

NUCLEATION AND EPITAXY OF CONDUCTIVE BUFFERS ON (001) Cu FOR  
COATED HIGH-TEMPERATURE SUPERCONDUCTING CONDUCTORS

By

KYUNGHOON KIM

A DISSERTATION PRESENTED TO THE GRADUATE SCHOOL  
OF THE UNIVERSITY OF FLORIDA IN PARTIAL FULFILLMENT  
OF THE REQUIREMENTS FOR THE DEGREE OF  
DOCTOR OF PHILOSOPHY

UNIVERSITY OF FLORIDA

2005

Copyright 2005

by

Kyunghoon Kim

To my family for their love and encouragement

## ACKNOWLEDGMENTS

Above all, I would like to express my sincere appreciation to my advisor, Professor David P. Norton, for his excellent guidance and invaluable help. I cannot forget his warm support and the five years that I worked for Dr. Norton was the precious time in my life.

My appreciation also goes to my committee members, Professor Cammy R. Abernathy, Professor Rajiv Singh, Professor Wolfgang Sigmund, and Professor Andrew Rinzler.

Since I started collaboration research in Oak Ridge National Laboratory, I received a lot of support from the staff members and post doctors. I would like to give my deep appreciation to Dr. David K. Christen, who is my supervisor and a group leader of the superconductivity group. Dr. Christen gave made me feel comfortable staying in ORNL as a graduate student. I wish to give my special thanks to the members of Condensed Matter Sciences Division, Metals and Ceramics Division, and Chemical Science Division: Dr. Claudia Cantoni, who helped me use the PLD system and shared a lot of time to discuss technical issues; Dr. Tolga Aytug, who helped me use the sputtering system and gave me great advice; Dr. Albert A. Gapud, who helped me use the transport measuring system; Professor James R. Thompson, who helped me use the SQUID system and gave me lots of technical information; Yifei Zhang, who helped me use the SQUID system; Dr. M. Paranthaman, who gave me valuable help and encouraged me; Dr. Amit Goyal, who supported metal substrates; Patrick M. Martin, who helped me use electrical measuring instruments and annealing system; Dr. Ho Nyung Lee, who helped me get a

lot of physical results and shared precious time to discuss technical issues; Dr. Sukill Kang, who helped me use various instruments and gave me warm support; and Dr. Daeho Kim and Dr. Mina Yoon who taught me lots of fundamental physics. I also want to thank all the members of Dr. Norton's group.

I would like to acknowledge the enormous help of my sister-in-law, Youri, and her family. They gave me a lot of joy and happiness. I also express my deep appreciation to my elder sister, Hyeonjoo, who always encouraged me and prayed for my family. I would like to give my special thanks to my parents-in-law for their great affection and concern. Especially, it is my great honor to dedicate this work to my father-in-law who passed away last February. I am also deeply grateful to my parents, with all my respect, for their endless love, patience and prayers for me and my family.

Finally, my great gratitude goes to my lovely wife, Youmi Kang, and my son, Youngwook Kim. I sincerely appreciate my wife's encouragement, support and love. Without her love and support, I could not do all of this.

## TABLE OF CONTENTS

	<u>page</u>
ACKNOWLEDGMENTS .....	iv
LIST OF TABLES .....	viii
LIST OF FIGURES .....	ix
ABSTRACT .....	xiv
CHAPTERS	
1 INTRODUCTION .....	1
2 LITERATURE REVIEW .....	4
2.1 High Temperature Superconductors .....	4
2.2 Superconducting Power Applications using HTS Wire .....	9
2.2.1 Biaxially Textured Metal Substrates .....	11
2.2.2 Buffer Layers .....	13
2.3 Review of Conducting Oxide Buffers for Cu based YBCO Coated Conductors .....	16
2.3.1 Introduction .....	16
2.3.2 Preventing Methods of Cu Oxidation .....	20
2.3.3 Thin Film Techniques for Oxides Growth .....	22
2.3.4 Overview of Conductive Oxides for HTS Coated Conductors .....	25
3 GROWING EPITAXIAL $\text{Cu}_2\text{Mg}$ AS AN OXIDATION BARRIER FOR HIGH TEMPERATURE SUPERCONDUCTING COATED CONDUCTORS .....	55
3.1 Introduction .....	55
3.2 Experiments .....	57
3.3 Results and Discussion .....	57
3.4 Conclusions .....	58
4 (La,Sr)TiO <sub>3</sub> AS A CONDUCTING BUFFER LAYER FOR HIGH TEMPERATURE SUPERCONDUCTING COATED CONDUCTORS .....	66
4.1 Introduction .....	66
4.2 Experiments .....	68
4.3 Results and Discussion .....	69

4.4 Conclusions.....	73
5 EPITAXIAL (La,Sr)TiO <sub>3</sub> AS A CONDUCTIVE BUFFER FOR Ni-W BASED HIGH TEMPERATURE SUPERCONDUCTING COATED CONDUCTORS .....	90
5.1 Introduction.....	90
5.2 Experiments .....	92
5.3 Results and Discussion .....	93
5.4 Conclusions.....	96
6 EPITAXIAL (La,Sr)TiO <sub>3</sub> AS A CONDUCTIVE BUFFER FOR Cu BASED HIGH TEMPERATURE SUPERCONDUCTING COATED CONDUCTORS .....	111
6.1 Introduction.....	111
6.2 Experiments .....	113
6.3 Results and Discussion .....	114
6.4 Conclusions.....	117
7 SUMMARY .....	131
LIST OF REFERENCES .....	134
BIOGRAPHICAL SKETCH .....	145

## LIST OF TABLES

<u>Table</u>	<u>page</u>
2-1. The critical temperature values in absolute temperature unit reported for $\text{YBa}_2(\text{Cu}_{1-x}\text{M}_x)_3\text{O}_{7-\delta}$ systems. ....	31
2-2. The list of buffer layer materials tested with RABiTS applications.....	32
2-3. The overall electrical and structural properties of perovskite oxide compounds mentioned in this section. ....	33



## LIST OF FIGURES

<u>Figure</u>	<u>page</u>
2-1. (a) Schematic drawing of energy gap in superconducting material, (b) the energy gap dependence on temperature with theoretical value versus experimental results for some elemental metals. ....	34
2-2. Schematic drawing of the critical space within which the superconductivity remains (T-H-I diagram). ....	35
2-3. Phase diagram of type II superconductor with temperature and magnetic field dependency. ....	35
2-4. Schematic drawing of $\text{La}_2\text{CuO}_4$ . ....	36
2-5. Schematic drawing of $\text{YBa}_2\text{Cu}_3\text{O}_{7-\delta}$ unit cell combined with oxygen deficient perovskite structure. ....	37
2-6. Schematic drawing of $\text{YBa}_2\text{Cu}_3\text{O}_6$ compound which has different CuO chains with $\text{YBa}_2\text{Cu}_3\text{O}_7$ . ....	38
2-7. Schematic drawing of (a) Bi-Sr-Cu-O, (b) Bi-Sr-Ca-Cu-O (double Cu-O sheets), and (c) Bi-Sr-Ca-Cu-O (triple Cu-O sheets). ....	39
2-8. Conceptual drawing of rolling assisted biaxially textured substrate (RABiTS) process based on Ni substrate. The pattern inside the circle designates the texture alignment of the substrate. ....	40
2-9. The X-ray diffraction $\omega$ -scan (rocking curve) of (002) Ni which indicates the substrate's out-of-plane alignment. The full-width-half-maximum (FWHM) of the curve is $5.4555^\circ$ . ....	41
2-10. The x-ray diffraction $\phi$ -scan of (111) Ni which indicates the substrate's in-plane alignment. The average full-width-half-maximum (FWHM) of the 4 peaks is $7.7762^\circ$ . ....	42
2-11. The log-scale (111) Ni pole figure of the Ni substrate formed by RABiTS process. The cube fraction of the substrate is 98.2694%. ....	43

2-12. The X-ray diffraction $\theta$ - $2\theta$ scan graphs of textured Cu tapes formed by RABiTS process (a) before annealing and (b) after annealing at 800°C in vacuum for 2 hours. ....	44
2-13. The log-scale pole figures of (111) Cu substrates (a) before annealing and (b) after annealing at 800°C in vacuum for two hours. ....	45
2-14. Schematic vertical structure drawing of conventional 2G wire based on YBCO HTS. ....	46
2-15. SEM cross-section of AMSC's 2G wire.....	46
2-16. Resistivity comparison of Cu tape and Ni-W (3 at.%) tape as a function of the temperature.....	47
2-17. Simulated graph of cap layer thickness as a function of current per tape width. ....	48
2-18. Simulated graph of engineering current density as a function of current per tape width.....	49
2-19. Thermodynamic stability curve of Cu in terms of temperature and oxygen partial pressure.....	50
2-20. Schematic drawing of magnetron sputtering system. ....	51
2-21. Schematic drawing of electron beam evaporation system.....	52
2-22. Schematic drawing of pulsed laser deposition system. ....	53
2-23. Schematic drawing of typical perovskite crystal structure. ....	54
2-24. Schematic diagram of Zaanen, Sawatzky and Allen (ZSA) framework. ....	54
3-1. The vertical structure which is used for this experiment.....	60
3-2. The X-ray diffraction $\theta$ - $2\theta$ scan along the surface normal for a multilayer structure annealed at 400°C.....	61
3-3. The X-ray diffraction rocking curve for the (004) $\text{Cu}_2\text{Mg}$ peak, indicating a full-width half-maximum (FWHM) of $\Delta\theta = 2.0^\circ$ . ....	62
3-4. The X-ray diffraction $\phi$ -scan through the $\text{Cu}_2\text{Mg}$ (222).....	63
3-5. The X-ray diffraction $\theta$ - $2\theta$ scan of the (Cu,Mg) multilayer after annealing at 400, 500, 600, 700°C.....	64
3-6. The SEM picture of (a) $\text{CeO}_2$ film on Ni / Cu / MgO (b) $\text{CeO}_2$ / Ni / (Cu,Mg) / Cu / MgO structure. ....	65

4-1. The X-ray diffraction $\theta$ - $2\theta$ scan of (La,Sr)TiO <sub>3</sub> film grown on SrTiO <sub>3</sub> single crystal substrate by pulsed laser deposition (PLD) method at 750°C, in vacuum. ....	74
4-2. The in situ reflection high-energy electron diffraction (RHEED) pattern of (La,Sr)TiO <sub>3</sub> film deposited on SrTiO <sub>3</sub> single crystal substrate by PLD method at 750°C, in vacuum. RHEED is used to monitor the epitaxial film growth. ....	75
4-3. The X-ray $\theta$ - $2\theta$ scans of (La,Sr)TiO <sub>3</sub> films deposited on SrTiO <sub>3</sub> single crystal substrates in different ambient conditions. ....	76
4-4. The X-ray diffraction $\theta$ - $2\theta$ scan of LaTiO <sub>3</sub> film grown on SrTiO <sub>3</sub> single crystal substrate by pulsed laser deposition (PLD) method at 750°C, in vacuum. ....	77
4-5. The two different X-ray $\theta$ - $2\theta$ scans of LaTiO <sub>3</sub> film grown on SrTiO <sub>3</sub> single crystal substrate in the oxygen pressure of $3.0 \times 10^{-5}$ Torr, aligned to (a) the substrate (001) plane and (b) the La <sub>2</sub> Ti <sub>2</sub> O <sub>7</sub> (-210) plane, respectively. ....	78
4-6. The two different X-ray $\theta$ - $2\theta$ scans of LaTiO <sub>3</sub> film grown on SrTiO <sub>3</sub> single crystal substrate in the oxygen pressure of $4.0 \times 10^{-4}$ Torr, aligned to (a) the substrate (001) plane and (b) the La <sub>2</sub> Ti <sub>2</sub> O <sub>7</sub> (-210) plane, respectively. ....	79
4-7. The X-ray $\phi$ -scan of (-420) peak for La <sub>2</sub> Ti <sub>2</sub> O <sub>7</sub> layer grown on SrTiO <sub>3</sub> single crystal substrate in the oxygen pressure of $3.0 \times 10^{-5}$ Torr. ....	80
4-8. The resistivities of (La,Sr)TiO <sub>3</sub> and LaTiO <sub>3</sub> films on single crystal SrTiO <sub>3</sub> , measured at (a) 300 K and (b) 77 K, as a function of the oxygen pressure. ....	81
4-9. The resistivity curves of (La,Sr)TiO <sub>3</sub> films on SrTiO <sub>3</sub> substrates grown in (a) vacuum, (b) $3.0 \times 10^{-5}$ Torr of oxygen, and (c) $4.0 \times 10^{-4}$ Torr of oxygen, as a function of temperature. ....	82
4-10. The resistivity curves of LaTiO <sub>3</sub> films on SrTiO <sub>3</sub> substrates grown in (a) vacuum, (b) $3.0 \times 10^{-5}$ Torr of oxygen, and (c) $4.0 \times 10^{-4}$ Torr of oxygen, as a function of temperature. ....	83
4-11. The X-ray $\theta$ - $2\theta$ scan of YBa <sub>2</sub> Cu <sub>3</sub> O <sub>7</sub> deposited on (La,Sr)TiO <sub>3</sub> buffer layer on SrTiO <sub>3</sub> single crystal substrate. ....	84
4-12. The X-ray $\omega$ -scan of (a) (002) peak for (La,Sr)TiO <sub>3</sub> buffer layer on SrTiO <sub>3</sub> single crystal substrate and (b) (006) peak for the YBa <sub>2</sub> Cu <sub>3</sub> O <sub>7</sub> film deposited on (La,Sr)TiO <sub>3</sub> buffer layer. ....	85
4-13. The X-ray $\phi$ -scan of (a) (112) peak for (La,Sr)TiO <sub>3</sub> buffer layer on SrTiO <sub>3</sub> single crystal substrate and (b) (012) peak for the YBa <sub>2</sub> Cu <sub>3</sub> O <sub>7</sub> film deposited on (La,Sr)TiO <sub>3</sub> buffer layer. ....	86

4-14. The resistivity versus temperature measurement for $\text{YBa}_2\text{Cu}_3\text{O}_7$ film deposited on $(\text{La,Sr})\text{TiO}_3$ buffer layer on single crystal $\text{SrTiO}_3$ substrate. ....	87
4-15. The critical current density ( $J_c$ ) as a function of magnetic field of $\text{YBa}_2\text{Cu}_3\text{O}_7$ film deposited on $(\text{La,Sr})\text{TiO}_3$ buffer layer on single crystal $\text{SrTiO}_3$ substrate. ....	88
4-16. The resistivity versus temp. graph of $(\text{La,Sr})\text{TiO}_3$ film grown on single crystal $\text{SrTiO}_3$ substrate after annealing with the $\text{YBa}_2\text{Cu}_3\text{O}_7$ deposition condition. ....	89
5-1. The X-ray diffraction $\theta$ - $2\theta$ scan of $(\text{La,Sr})\text{TiO}_3$ films deposited directly on Ni-W tape by PLD at the temperature of (a) $700^\circ\text{C}$ , (b) $750^\circ\text{C}$ , and (c) $800^\circ\text{C}$ . ....	97
5-2. The energy dispersive X-ray spectroscopy (EDS) results of TiN films grown on Cu layers on single crystal $\text{SrTiO}_3$ substrates with the thicknesses of (a) $500\text{\AA}$ , (b) $1000\text{\AA}$ , (c) $2000\text{\AA}$ , and (d) $5000\text{\AA}$ . These curves were taken after annealing the samples at $740^\circ\text{C}$ , in vacuum for 60 minutes. ....	98
5-3. The atomic percent of Cu observed on the surface of TiN layer with the thickness range of $500\sim 5000\text{\AA}$ . The square symbols designate the samples without annealing. The circles and triangles show the samples with annealing at $740^\circ\text{C}$ , in vacuum for 30 minutes and 60 minutes, respectively. ....	99
5-4. The X-ray diffraction $\theta$ - $2\theta$ scan of (a) TiN layer deposited on textured Ni-W alloy tape, and (b) $(\text{La,Sr})\text{TiO}_3$ film deposited on TiN seed layer. ....	100
5-5. The in situ reflection high-energy electron diffraction (RHEED) pattern of (a) TiN film deposited on textured Ni-W alloy tape, and (b) $(\text{La,Sr})\text{TiO}_3$ film deposited on TiN seed layer. ....	101
5-6. The X-ray diffraction $\omega$ -scan of (a) Ni-W (002), (b) TiN (002), and (c) $(\text{La,Sr})\text{TiO}_3$ (004) planes. ....	102
5-7. The X-ray diffraction $\phi$ -scan of (a) Ni-W (111), (b) TiN (111), and (c) $(\text{La,Sr})\text{TiO}_3$ (112) planes. ....	103
5-8. The X-ray diffraction $\theta$ - $2\theta$ scan of high temperature superconducting $\text{YBa}_2\text{Cu}_3\text{O}_7$ film grown on $(\text{La,Sr})\text{TiO}_3$ buffer layer / TiN seed layer / Ni-W tape. ....	104
5-9. The X-ray diffraction $\omega$ -scan of (005) $\text{YBa}_2\text{Cu}_3\text{O}_7$ which was grown on $(\text{La,Sr})\text{TiO}_3$ buffer layer / TiN seed layer / Ni-W tape. ....	105
5-10. The X-ray diffraction $\phi$ -scan of (103) $\text{YBa}_2\text{Cu}_3\text{O}_7$ which was grown on $(\text{La,Sr})\text{TiO}_3$ buffer layer / TiN seed layer / Ni-W tape. ....	106
5-11. The resistivity versus temperature graph for $\text{YBa}_2\text{Cu}_3\text{O}_7$ film grown on $(\text{La,Sr})\text{TiO}_3$ buffer layer / TiN seed layer / Ni-W tape. ....	107

5-12. The voltage versus current graph of $\text{YBa}_2\text{Cu}_3\text{O}_7$ film deposited on (La,Sr) $\text{TiO}_3$ buffer layer / TiN seed layer / Ni-W tape.....	108
5-13. The SEM picture of $\text{YBa}_2\text{Cu}_3\text{O}_7$ film surface deposited on (La,Sr) $\text{TiO}_3$ buffer layer / TiN seed layer / Ni-W tape. ....	109
5-14. The energy dispersive X-ray spectroscopy (EDS) results of $\text{YBa}_2\text{Cu}_3\text{O}_7$ film grown on (La,Sr) $\text{TiO}_3$ / TiN / Ni-W tape. ....	110
6-1. The surface SEM picture of the (La,Sr) $\text{TiO}_3$ film grown on Cu tape after annealing at 780°C in oxygen partial pressure of $1.0 \times 10^{-1}$ Torr for 7 minutes. ....	118
6-2. The energy dispersive X-ray spectroscopy (EDS) graph of (La,Sr) $\text{TiO}_3$ film grown on Cu tape after annealing at 780°C in oxygen $1.0 \times 10^{-1}$ Torr for 7 minutes. ....	119
6-3. The X-ray diffraction $\theta$ - $2\theta$ scan of (a) Ir layer deposited on textured Cu by PLD, and (b) (La,Sr) $\text{TiO}_3$ film deposited on Ir layer. ....	120
6-4. The in situ reflection high-energy electron diffraction (RHEED) pattern of Ir film deposited on textured Cu tape, and (b) (La,Sr) $\text{TiO}_3$ film deposited on Ir layer. ....	121
6-5. The X-ray diffraction $\omega$ -scan of (a) Cu (002), (b) Ir (002), and (c) (La,Sr) $\text{TiO}_3$ (004) planes.....	122
6-6. The X-ray diffraction $\phi$ -scan of (La,Sr) $\text{TiO}_3$ (112) which was grown on Ir film on Cu tape. ....	123
6-7. The X-ray pole figures of (a) Cu (111), (b) Ir (111), and (c) (La,Sr) $\text{TiO}_3$ (112). ....	124
6-8. The resistivity curves of Ir on $\text{SrTiO}_3$ single crystal, (La,Sr) $\text{TiO}_3$ film on $\text{SrTiO}_3$ substrate and (La,Sr) $\text{TiO}_3$ film on Ir on $\text{SrTiO}_3$ substrate.....	125
6-9. The resistivity curves of Ir on $\text{SrTiO}_3$ single crystal with and without annealing at 780°C in oxygen $1.0 \times 10^{-1}$ Torr for 7 minutes. ....	126
6-10. The X-ray diffraction $\theta$ - $2\theta$ scan of $\text{YBa}_2\text{Cu}_3\text{O}_7$ layer deposited on (La,Sr) $\text{TiO}_3$ / Ir multi buffer stack on textured Cu tape. ....	127
6-11. The surface SEM picture of the $\text{YBa}_2\text{Cu}_3\text{O}_7$ film grown on (La,Sr) $\text{TiO}_3$ / Ir buffer stack on Cu tape with the magnification of (a) $\times 1000$ and (b) $\times 5000$ .....	128
6-12. The energy dispersive X-ray spectroscopy (EDS) graph of (a) normal $\text{YBa}_2\text{Cu}_3\text{O}_7$ film surface, (b) defect region of $\text{YBa}_2\text{Cu}_3\text{O}_7$ film. ....	129
6-13. The resistivity versus temperature measurement for $\text{YBa}_2\text{Cu}_3\text{O}_7$ film deposited on (La,Sr) $\text{TiO}_3$ / Ir multi buffer stack on Cu tape. ....	130

Abstract of Dissertation Presented to the Graduate School  
of the University of Florida in Partial Fulfillment of the  
Requirements for the Degree of Doctor of Philosophy

NUCLEATION AND EPITAXY OF CONDUCTIVE BUFFERS ON (001) Cu FOR  
COATED HIGH-TEMPERATURE SUPERCONDUCTING CONDUCTORS

By

Kyunghoon Kim

August 2005

Chair: David P. Norton

Major Department: Materials Science and Engineering

In the 2<sup>nd</sup> generation wire technology of high temperature superconducting coated conductors, highly conductive and nonmagnetic Cu substrate can improve the wire properties along with the conductive buffer layers, offering fully conductive wire architecture. This scheme requires two components, namely oxidation resistance for the Cu tape and conductive buffer layers.

The growth of epitaxial Cu<sub>2</sub>Mg as an oxidation barrier was investigated. Epitaxy of (004) Cu<sub>2</sub>Mg intermetallic phase was achieved on (002) Cu film. An in-plane  $\phi$ -scan through the Cu<sub>2</sub>Mg (222) and the x-ray diffraction rocking curve for the (004) Cu<sub>2</sub>Mg peak indicates that the intermetallic phase is well oriented on (002) Cu surface.

The perovskite (La,Sr)TiO<sub>3</sub> was investigated as a possible conducting oxide buffer layer for high temperature superconducting coated conductors. YBa<sub>2</sub>Cu<sub>3</sub>O<sub>7</sub> was grown epitaxially on (La,Sr)TiO<sub>3</sub> buffer layer on SrTiO<sub>3</sub> substrate with excellent in-plane and out-of-plane alignment. The superconducting transition temperature ( $T_c$ ) of YBa<sub>2</sub>Cu<sub>3</sub>O<sub>7</sub> /

(La,Sr)TiO<sub>3</sub> / SrTiO<sub>3</sub> structure was 91 K and the critical current density ( $J_c$ ) of this structure was  $2.18 \times 10^6$  A/cm<sup>2</sup> at 0 magnetic field. The resistivity results of a post annealed sample at YBa<sub>2</sub>Cu<sub>3</sub>O<sub>7</sub> deposition condition indicates that the (La,Sr)TiO<sub>3</sub> layer can be a candidate for the conductive buffer layer in the coated conductor applications.

The epitaxial film growth of (La,Sr)TiO<sub>3</sub> was examined on Ni-W metal alloy tape. The transition metal nitride such as TiN was deposited epitaxially on Ni-W tape by PLD and played an excellent role as a seed layer for (La,Sr)TiO<sub>3</sub> film growth on Ni-W tape. The YBa<sub>2</sub>Cu<sub>3</sub>O<sub>7</sub> film was deposited epitaxially on the (La,Sr)TiO<sub>3</sub> buffer layer with the TiN seed layer on Ni-W tape. The YBa<sub>2</sub>Cu<sub>3</sub>O<sub>7</sub> film grown on (La,Sr)TiO<sub>3</sub> / TiN / Ni-W tape has  $T_c$  of 89 K and  $J_c$  of  $0.42 \times 10^6$  A/cm<sup>2</sup>.

The epitaxial film growth of (La,Sr)TiO<sub>3</sub> was examined on Cu tape as a possible conducting buffer layer for high temperature superconducting coated conductors. The noble metal, such as Ir, was deposited epitaxially on Cu tape by PLD for an oxygen diffusion barrier. The YBa<sub>2</sub>Cu<sub>3</sub>O<sub>7</sub> film was deposited epitaxially on the (La,Sr)TiO<sub>3</sub> and Ir buffer stack on Cu tape. The YBa<sub>2</sub>Cu<sub>3</sub>O<sub>7</sub> film grown on the (La,Sr)TiO<sub>3</sub> / Ir / Cu tape has a superconducting transition temperature of 90 K and a critical current density value of  $1.0 \times 10^6$  A/cm<sup>2</sup>. This shows that (La,Sr)TiO<sub>3</sub> is a possible candidate for the conductive buffer layer in the Cu based RABiTS applications.

## CHAPTER 1 INTRODUCTION

The coated high-temperature superconducting (HTS) conductors consist of metal substrate, buffer layers and thin film superconducting oxide. The rolling-assisted biaxially textured substrate (RABiTS) process made it possible to offer long length HTS wire. The advantages of Cu tape with nonmagnetic, lower material cost (~20% of Ni), easy formation of a sharp cube texture and higher electrical and thermal conductivity (for Cu,  $k : 398 \text{ W/m-K}$  and for Ni,  $k : 90 \text{ W/m-K}$ ) than Ni or Ni based alloy tapes can improve the  $\text{YBa}_2\text{Cu}_3\text{O}_7$  based 2G wire properties along with the conductive buffer layers, which offers fully conductive wire architecture.

Though the Cu based RABiTS process with the conductive buffer architecture has advantages, the Cu oxidation problem could be worse. In metallurgical applications, enhancement of Cu oxidation resistance has been investigated by several approaches. Among these, the use of Mg-doped Cu films as an oxygen diffusion barrier is being investigated with the intermetallic phase of  $\text{Cu}_2\text{Mg}$ .

There are key issues for a conductive buffer layer of HTS coated conductors. First, it must be reasonably well lattice matched to both the metal substrate and the superconducting film, thus enabling epitaxy. Second, the interaction between the buffer layer and the metal substrate must be such as to minimize formation of any native interfacial oxide that would serve as an insulating barrier to shunted current flow. An alternative candidate material system that may satisfy the criteria for conductive buffers mentioned above is  $(\text{La,Sr})\text{TiO}_3$ .  $\text{LaTiO}_{3+x}$  is an interesting defect perovskite system, with



transport properties varying from insulating to metallic based on oxygen stoichiometry. La and Ti have a relatively high affinity for oxygen. This suggests that the driving force for native oxide formation at the interface between  $\text{LaTiO}_3$  and either Ni or Cu should be reasonably low. With an extreme sensitivity to oxygen content,  $\text{LaTiO}_{3+x}$  is not particularly attractive as a conductive buffer layer. One possible approach to maintaining metallic conductivity in an oxidized state is through cation doping. This could maintain carrier density as well as reduce oxygen diffusivity. The most likely dopant candidate is Sr. Doping with a divalent element increases the  $\text{Ti}^{+3} / \text{Ti}^{4+}$  ratio and can make the compound less sensitive to ambient oxygen pressure during YBCO deposition.

One objective of this work is to investigate the epitaxial growth of intermetallic  $\text{Cu}_2\text{Mg}$  phase as an oxygen diffusion barrier for high temperature superconducting coated conductors. The other one is to grow epitaxial  $(\text{La,Sr})\text{TiO}_3$  film as a conductive buffer layer for Cu based RABiTS applications.

Chapter 2 reviews the fundamental background of the high temperature superconductors and the rolling-assisted biaxially textured substrate (RABiTS) process including textured metal substrates and buffer layers. In this chapter, preventing method of Cu oxidation, thin film techniques for oxides growth and overview of various conductive oxides for HTS coated conductors will be mentioned. Chapter 3 gives the results of epitaxial  $\text{Cu}_2\text{Mg}$  growth as an oxygen diffusion barrier for Cu RABiTS. Chapter 4 describes the fundamental characteristics of the  $(\text{La,Sr})\text{TiO}_3$  film as a conductive buffer layer for coated conductors. The oxygen sensitivity of  $(\text{La,Sr})\text{TiO}_3$  film will be investigated with the comparison of  $\text{LaTiO}_3$  film. The electrical transport property such as resistivity as a function of temperature will be covered with various oxygen

pressure conditions. Chapter 5 is for the application of (La,Sr)TiO<sub>3</sub> film as a conductive buffer layer in Ni-W based RABiTS process. In this chapter, epitaxial TiN layer deposited by PLD method on Ni-W tape will be mentioned as a seed layer for (La,Sr)TiO<sub>3</sub> film. Chapter 6 is for the application of (La,Sr)TiO<sub>3</sub> film as a conductive buffer layer in Cu based RABiTS architecture. Epitaxial Ir layer grown by PLD method on Cu tape will be described as an oxygen diffusion barrier. From the result of chapter 6, the feasibility of (La,Sr)TiO<sub>3</sub> film as a conductive buffer layer for Cu based coated conductor will be confirmed. Finally, chapter 7 is the summary for my dissertation.

## CHAPTER 2 LITERATURE REVIEW

### 2.1 High Temperature Superconductors

Superconductivity is an electronic phase transition in which a metal displays a dc resistivity of identically zero and behaves as a perfect diamagnetic material in excluding magnetic field. Most metals do not exhibit a superconducting phase. The low temperature superconductors (LTS) show zero electrical resistance usually well below 20 K. Single elements such as Hg (superconducting transition temperature  $T_c$  : 4.1 K), Pb ( $T_c$  : 7.2 K), Nb ( $T_c$  : 9.2 K) and various compounds show superconducting behavior at low temperatures. Nb<sub>3</sub>Sn ( $T_c$  : 18.1 K) known as A15 superconductors [1], Li<sub>1+x</sub>Ti<sub>2-x</sub>O<sub>4</sub> ( $T_c$  : 13.7 K) [2] and BaPb<sub>1-x</sub>Bi<sub>x</sub>O<sub>3</sub> ( $T_c$  : 11.7 K) [3] are the examples of compound LTS.

The BCS theory (proposed by John Bardeen, Leon Cooper and Robert Shrieffer in 1957) gives an explanation of superconductivity behavior [4]. According to this model, pairs of electrons (Cooper pair) interact with crystal lattice vibrations in such a way so that an attractive potential results from this interaction. The electron pairs have a slightly lower energy than unpaired electrons and produce an energy gap which decreases from about  $3.5k_B T_c$  at  $T=0$  K (where  $k_B$  is Boltzmann constant =  $8.616 \times 10^{-5}$  eV/ K) to zero at  $T_c$ . This reduced energy gap as a function of temperature was experimentally supported by Townsend *et al.* [5]. Figure 2-1 is schematic drawing of the energy gap of superconductor material and the energy gap dependence on temperature with theoretical value vs experimental results for some elemental metals [6]. There are two important characteristic lengths associated with superconductivity. One is the London penetration

depth, which describes the magnetic field decay inside the superconductor [7]. The penetration depth,  $\lambda_L$ , is defined by  $B_z = B_z(0) \exp(-x/\lambda_L)$ , where  $B_z$  is the magnetic field inside the superconducting material,  $B_z(0)$  is the magnetic field at the interface and  $x$  is the distance from the interface. The exclusion of magnetic field by superconductors, known as the Meissner effect, can be explained by this London theory. The other characteristic length is the coherence length,  $\xi$ , which is related to the transition layer thickness from superconducting state to a normal state. The coherence length is the decay distance of the superconducting wavefunction [8].

In addition to  $T_c$ , there are two more critical parameters that characterize superconducting behavior. The critical magnetic field,  $H_c$ , is the magnetic field strength above which the superconductivity disappears. It depends on the temperature as described by  $H_c(T) = H_c(0) [1 - (T / T_c)^2]$ . Superconductivity also vanishes if too much current is flowing through the material. The limiting current is called the critical current  $I_c$ . Superconductivity remains only when the temperature, magnetic field and current are below these three limiting factors ( $T_c$ ,  $H_c$ ,  $I_c$ ). Figure 2-2 shows the phase space within which the superconductivity remains (T-H-I diagram). A sharp transition from the superconducting state to a normal state with applied magnetic field is observed in type I superconductors. Practical limitation exists in Type I superconductor because of the low  $H_c$  value. Type II superconductors has somewhat different transition behavior. The transition from the superconducting state to a normal state is gradual, and there exists an upper critical magnetic field  $H_{c2}$  which is higher than  $H_{c1}$ . The type I and II superconductors can be distinguished by using the Ginzburg-Landau parameter,  $\kappa$ , which is the ratio of penetration depth  $\lambda_L$  to coherence length  $\xi$  ( $\kappa \equiv \lambda_L / \xi$ ). A Type I

superconductor shows the  $\kappa$  value far below 1 ( $\xi \gg \lambda_L$ ). Pure, elemental superconductors are in this category. When  $\lambda_L$  is larger than  $\xi$  ( $\kappa \gg 1$ ), such superconductors are in the type II category.

The magnetic field begins to penetrate through the type II superconductors when the field strength reaches a lower critical magnetic field ( $H_{c1}$ ). This phenomenon is described as a vortex state. Type II superconductors have cylindrically symmetric domains called vortices which are in the normal state and surrounded by the superconducting matrix. An external magnetic field can penetrate through these vortices which the material remains in the superconducting state. A superconducting current can be maintained in the superconducting matrix if the vortices are pinned to their positions (fluxoid pinning). As the temperature or the magnetic field is increased, the vortex density increases, with vortices getting close to each other. Finally the superconductivity disappears at the upper critical magnetic field ( $H_{c2}$ ). Figure 2-3 shows the vortex state or mixed state which exists in the type II superconductors. Superconducting alloys and compounds show type II superconductivity with relatively high transition temperatures, flowing large currents and often operating in large magnetic fields [9]. Type II superconductors are sometimes referred to as hard superconductors because of these properties mentioned.

A high temperature superconductor (HTS) typically describes a material in which the superconducting transition temperature is greater than 30 K. In 1986, Bednorz and Müller discovered Ba-La-Cu-O system which showed superconductivity in the 30 K range [10]. Various oxide compounds have been explored since this first HTS discovery. Y-Ba-Cu-O compounds showing superconductivity transition between 80 and 93 K were

reported by Wu *et al.* in 1987 [11]. Maeda *et al.* discovered the Bi-Sr-Ca-Cu-O system with the  $T_c$  of about 105 K in 1988 [12]. The Tl-Ba-Ca-Cu-O superconductor, which showed 120 K transition temperature, was discovered by Sheng *et al.* in 1988 [13]. The highest  $T_c$  (above 120 K) was reported in the Hg-Ba-Ca-Cu-O system by Putlin *et al.* in 1993 [14].

The generic structure of all HTS compounds consists of layered  $\text{CuO}_2$  planes and charge reservoir blocks in a unit lattice cell [15]. The  $\text{CuO}_2$  planes are separated by divalent or trivalent atoms. The superconductivity, as well as charge transport, are mostly confined to the  $\text{CuO}_2$  planes. Figure 2-4 is the schematic drawing of  $\text{La}_2\text{CuO}_4$ . Carrier doping by substitution of alkaline earth atoms with trivalent rare earth atoms such as  $(\text{La,Sr})_2\text{CuO}_4$  makes it superconducting at 40 K.  $\text{YBa}_2\text{Cu}_3\text{O}_7$  has been extensively explored for superconducting devices and wires.  $\text{YBa}_2\text{Cu}_3\text{O}_{7-\delta}$  is a hole-doped superconductor possessing a  $\text{Cu}^{3+} / \text{Cu}^{2+}$  valence state mixture. Its crystal structure is orthorhombic with  $a = 3.82\text{\AA}$ ,  $b = 3.88\text{\AA}$ , and  $c = 11.68\text{\AA}$  [16]. Figure 2-5 is the schematic drawing of the  $\text{YBa}_2\text{Cu}_3\text{O}_{7-\delta}$  unit cell which can be thought of as an oxygen deficient perovskite structure. One unit cell of  $\text{YBa}_2\text{Cu}_3\text{O}_{7-\delta}$  contains one Y atom, two Ba atoms, three Cu atoms and seven O atoms. The  $\text{YBa}_2\text{Cu}_3\text{O}_{7-\delta}$  unit cell consists of two  $\text{CuO}_2$  planes separated by a Y atom. CuO chains are between the Ba-O layers. Growth temperature and oxygen stoichiometry affects the oxygen site occupancy and transition temperature of the  $\text{YBa}_2\text{Cu}_3\text{O}_{7-\delta}$  compound. For films, the lattice parameters can depend on growth temperature. The  $T_c$  can be reduced below 40 K with  $\delta = 0.7$  [17, 18]. In the case of  $\delta = 1$ ,  $\text{YBa}_2\text{Cu}_3\text{O}_6$  compound is not superconductor and shows a tetragonal structure with  $a = 3.857\text{\AA}$  and  $c = 11.819\text{\AA}$  [19]. Figure 2-6 is the schematic drawing of

YBa<sub>2</sub>Cu<sub>3</sub>O<sub>6</sub> compound. The structural difference between  $\delta = 0$  (Figure 2.5) and  $\delta = 1$  (Figure 2-6) is in the CuO chains which play a crucial role in superconductivity. The highest  $J_c$  can be obtained for current flow parallel to the *a-b* planes, reflecting the anisotropic crystal structure characteristics. The c-axis oriented epitaxial YBa<sub>2</sub>Cu<sub>3</sub>O<sub>7</sub> films can be deposited by various techniques. Coevaporation is one of the earliest proposed methods for YBa<sub>2</sub>Cu<sub>3</sub>O<sub>7</sub> film growth [20–22]. Y, Cu, and BaF<sub>2</sub> from separate sources are coevaporated and an *ex situ* annealing in oxygen ambient is performed. The RF magnetron sputtering method [23] and pulsed laser deposition method [24] for YBa<sub>2</sub>Cu<sub>3</sub>O<sub>7</sub> film growth were also reported. The detailed thin film growth technique will be explained in Chapter 2.3.

The maximum superconducting transition temperature of the Bi-Sr-Ca-Cu-O system was found at 105 K which is greater than that of YBa<sub>2</sub>Cu<sub>3</sub>O<sub>7</sub>. The Bi-Sr-Cu-O system without Ca has a maximum  $T_c$  value of 22 K [25,26]. The crystal structure of Bi-Sr-Ca-Cu-O system is an incommensurate superstructure based on an orthorhombic subcell with  $a = 5.414\text{\AA}$ ,  $b = 5.44\text{\AA}$ ,  $c = 30.78\text{\AA}$  [27]. Figure 2-7 is the schematic drawings of Bi-Sr-Cu-O and Bi-Sr-Ca-Cu-O compounds. If there is no calcium [Figure 2-7(a)], the compound shows low temperature superconductivity. The important difference between Figure. 2-7 (b) and (c) is the number of Cu-O sheets. The compounds of double Cu-O sheets have orthorhombic c-axis of about  $30\text{\AA}$ , and the compounds that have triple Cu-O sheets show c-axis of about  $37\text{\AA}$  [28, 29]. This structural difference generated from the number of Cu-O sheets leads to the transition temperature alteration. The compound with the double Cu-O sheets shows a lower  $T_c$  phase of around 80 K, but the compound with triple Cu-O sheets shows a higher  $T_c$  phase as shown in Maeda's R-T curve [12].

The three basic high temperature superconductors such as La-A-Cu-O (A : Ba, Sr, Ca), R-Ba-Cu-O (R : rare earth element), and Bi-Sr-Ca-Cu-O compound have Cu-O sheets where Cu is in essentially square-planar coordination with  $\text{Cu}^{2+}$ . Subramanian suggested that the superconducting mechanism of the Bi-Sr-Ca-Cu-O compound is related to the orthorhombic distortion of pseudo-tetragonal sheets. Lowering the symmetry of the copper-oxygen sheets and the Bi-O sheets may play a role in this distortion [30]. The bulk Bi-Sr-Ca-Cu-O compounds can be synthesized by the procedure of calcining, grinding, pressing and sintering in air or oxygen ambient. Bismuth oxide ( $\text{Bi}_2\text{O}_3$ ), strontium carbonate ( $\text{SrCO}_3$ ), calcium carbonate ( $\text{CaCO}_3$ ) and copper oxide ( $\text{CuO}$ ) mixture can be used as the synthesizing agents. In order to produce Bi-Sr-Ca-Cu-O thin films for various device applications, laser sputtering [29], laser ablation [31], successive laser ablation with  $\text{N}_2\text{O}$  gas [28] and laser molecular beam epitaxy [32] methods have been used. Lead (Pb) can be added to this compound to reduce the processing temperature and increase the transition temperature. In the study of the new cuprate superconductors, Kawai *et al.* observed that the basic structure units in  $\text{Bi}_2\text{Sr}_2\text{Ca}_n\text{-}_1\text{Cu}_n\text{O}_{2n+4}$  and  $\text{Ti}_2\text{Ba}_2\text{Ca}_{n-1}\text{Cu}_n\text{O}_{2n+4}$  consist of layers of  $\text{Ca}(\text{Sr})\text{CuO}_2$  and  $n=1$  compound [32]. For example, the mixture of  $\text{CaCuO}_2$  with  $\text{Bi}_2\text{Sr}_2\text{CuO}_6$  ( $n=1$ ) gives the compound of  $\text{Bi}_2\text{Sr}_2\text{CaCu}_2\text{O}_8$  ( $n=2$ , so-called Bi-2212), and the mixture of  $2(\text{CaCuO}_2)$  with  $\text{Bi}_2\text{Sr}_2\text{CuO}_6$  ( $n=1$ ) gives  $\text{Bi}_2\text{Sr}_2\text{Ca}_2\text{Cu}_3\text{O}_{10}$  ( $n=3$ , so-called Bi-2223). For this reason,  $\text{CaCuO}_2$  is considered the parent structure of high temperature superconductors.

## 2.2 Superconducting Power Applications using HTS Wire

High-current power transmission cables are among the most exciting opportunities in the high temperature superconductor applications. The operating temperature of HTS materials such as Y-Ba-Cu-O and Bi-Pb-Sr-Ca-Cu-O compounds at liquid nitrogen of 77



K certainly has the attractive advantages. The cost savings of the liquid nitrogen is at least 50 times compared to liquid helium which is used to cool the LTS materials, such as Nb<sub>3</sub>Sn and NbTi, to 4.2 K. In addition, the cryogenic cooling and vacuum insulation systems will be simple by using liquid nitrogen. Other application examples of the superconductors include the field magnet for the motor, the rotor coil for a generator, transformer for power grids, a fault-current limiter which protects a power transmission and distribution system from surges, a current lead for reducing the heat loss in cryogenic machine, magnetic bearings which would be used with large flywheels, magnetically levitated trains for transportation, magnetic resonance imaging (MRI) for medical diagnostic instrument, and superconducting quantum interference devices (SQUID) for magnetic field sensors [33].

First-generation (1G) HTS wire using Bi-Pb-Sr-Ca-Cu-O compounds has the disadvantage of high cost because it is manufactured with superconductive filaments in a silver matrix using the powder-in-tube (PIT) procedure. The detail process of PIT will be mentioned in Chapter 2.3. In order to produce cost-effective long length wire, the process using superconducting Y-Ba-Cu-O material grown on metal tape has been proposed which is known as the second-generation (2G) wire.

An important factor that can influence the current density,  $J_c$ , in superconducting wire applications is the crystallinity of the HTS material. The high-angle grain boundaries generated in polycrystalline HTS reduce the critical current. The grain boundary can act as a weak superconducting interface. These are known as weak links. The grain boundary effect was demonstrated by Chaudhari *et al.* [34]. For this reason, the method of epitaxial YBa<sub>2</sub>Cu<sub>3</sub>O<sub>7</sub> film deposition on biaxially textured metal tapes was

introduced [35]. The  $\text{YBa}_2\text{Cu}_3\text{O}_7$  film grown on textured metal templates can drastically reduce the misorientation of the individual grains allowing improvement of the links in the current path. The metal tapes produced by the thermomechanical texturing are known as rolling assisted biaxially textured substrate (RABiTS). The RABiTS process includes depositing buffer layers and HTS materials on the biaxially textured flexible metal substrates.

### 2.2.1 Biaxially Textured Metal Substrates

The basic procedure for RABiTS consists of cold rolling a metal bar in long lengths and subsequent annealing in reducing condition. The primary metals of interest are Ni, Cu and the alloys. The  $\{100\}\langle 100 \rangle$  cube texture of the metal tape has cube plane parallel to the plane of the sheet and a cube edge parallel to the rolling direction. By continuous rolling, a smooth surface of the metal substrate can be obtained with root mean square (rms) roughness of  $\sim 50$  nm [36]. Subsequent annealing of the as-rolled metal tape enables the sharp  $\{100\}\langle 100 \rangle$  cube texture. The annealing is performed at  $800\sim 1000^\circ\text{C}$  in vacuum or ambient of  $\text{Ar}/\text{H}_2$  mixture gas for a few hours. Figure 2-8 shows the conceptual drawing of the RABiTS process including the buffer layer deposition [36].

The degree of texturing in metal substrates can be measured by x-ray diffraction. Figure 2-9 shows the x-ray  $\omega$ -scan of the (002) Ni which indicates the Ni substrate formed by RABiTS process has out-of-plane alignment. This measurement is done by fixing the sample in the  $2\theta$  position of (002) Ni and scanning the  $\theta$  angle. Figure 2-10 shows the x-ray  $\phi$ -scan of the (111) Ni which indicates the substrate has in-plane alignment. This measurement is done by fixing the sample in the  $2\theta$  and  $\psi$  position of (111) Ni, and scanning the  $\phi$  angle. Scanning the  $\phi$  angle is necessary to observe the in-

plane-alignment. The  $2\theta$  angle of (002) Ni is  $51.844^\circ$  [37]. The  $\psi$  angle of (111) Ni is  $35^\circ$  because the Ni has face-centered-cubic (fcc) crystal structure. The full-width-half-maximum (FWHM) of  $\omega$ - and  $\phi$ -scan graph is calculated by fitting Gaussian distribution to the measured data points. For the sample shown, the FWHM values of  $\omega$ - and  $\phi$ -scan are  $5.4555^\circ$  and  $7.7762^\circ$ , respectively. These are well matched with the typical data of Ni based RABiTS [38]. Figure 2-11 is the log-scale (111) Ni pole figure of the Ni tape. The pole figure is obtained by fixing the  $2\theta$  angle of (111) Ni and rotating the sample by  $360^\circ$  at an individual  $\psi$  angle from  $0^\circ$  to  $90^\circ$ . The cube fraction of textured substrate can be calculated by summing the intensities at the cube orientation locations and dividing by the total integrated intensity in the log-scale pole figure. The cube fraction for the sample in figure 2.11 is 98.2694%. The four dark circles indicate a well-developed, single component cube texture. The influence of the annealing on the cube texture can also be observed by the x-ray diffraction method. Figure 2-12 shows the x-ray diffraction  $\theta$ - $2\theta$  scan graphs of textured Cu substrates before and after annealing. The annealing condition is  $800^\circ\text{C}$  in vacuum for 2 hours. The  $\theta$ - $2\theta$  scan can not tell any differences between the before and after annealing samples because it only finds every  $2\theta$  angles that satisfies the Bragg's condition ( $n\lambda = 2d\sin\theta$ , here  $\lambda$  is the wave length of incident x-ray,  $d$  is the inter-plane distance and  $\theta$  is the scattering angle). The  $2\theta$  angle of (002) Cu is  $50.4309^\circ$  [37]. On the other hand, the pole figure graphs designate clear differences of cube texture between the two treatments. Figure 2-13 is the log-scale pole figure of (111) Cu formed by RABiTS process before and after annealing. Without annealing, there are many satellite intensities between each 4 peaks which indicates that the texture is not clearly aligned. After annealing at  $800^\circ\text{C}$  in vacuum for 2 hours, the satellite peaks disappear and

the cube fraction was 97.2784% which is higher than the sample without annealing of 84.6100%.

Pure Ni is ferromagnetic. This contributes to ac losses. Alloying Ni with W and Fe [39], W only [40] or Cr [41] were suggested to overcome this ferromagnetic problem. Addition of alloying element also increases the yield strength of the metal tape which can be acceptable for a large number of applications. Addition of 3 at. % W can enhance the yield strength of pure Ni from 34 MPa to 150 MPa and reduce the Curie temperature from 627 K to around 400 K [42].

### **2.2.2 Buffer Layers**

The first generation of high temperature superconducting wire technology was led by powder in tube (PIT) process with Bi-Pb-Sr-Ca-Cu-O superconductor material. On the other hand, the second generation (2G) wire is being developed by the RABiTS process with Y-Ba-Cu-O material. The RABiTS process consists of a biaxially textured metal substrate such as Ni, Cu or their alloys, buffer layers and  $\text{YBa}_2\text{Cu}_3\text{O}_7$ . The growth of HTS directly on the metal substrate has several obstacles. Due to the oxygen ambient ( $\sim 10^{-1}$  Torr) at elevated temperature ( $\sim 800^\circ\text{C}$ ) during the HTS film formation, the metal substrate can be oxidized resulting in metal oxide on the metal surface. Another problem is the cation substitution in the HTS material. For these reasons, buffer layers between the metal substrate and HTS material have an important role. The buffer layers should prevent oxidation of metal substrate and metal diffusion through the HTS material during the high oxygen pressure and high temperature process. In the case of forming metal oxide on metal substrate, epitaxial layer growth can be impeded which affects the epitaxial layer formation of HTS film. As mentioned in the previous section, the realization of an in plane and out-of-plane aligned HTS film is crucial for achieving high

critical current density  $J_c$ . The metal oxide also affects the mechanical strength of final coated conductors. When selecting proper buffer layers in the RABiTS process, one should consider the oxidation of metal substrate during buffer layer deposition itself. This is because the process condition of buffer layers can be at high temperature and in an oxidizing ambient. The solution to this problem is to find stable buffer layer materials relative to NiO, CuO or Cu<sub>2</sub>O in the growth condition. Jackson *et al.* reported the thermodynamic stability curves of NiO, CuO and Cu<sub>2</sub>O compared to several oxides by calculating Gibbs free energies of the reactants and products [43]. According to this report, MgO, CeO<sub>2</sub>, Y<sub>2</sub>O<sub>3</sub> are good possible candidates for buffer layers. Another important role of buffer layers is chemical separation of HTS from the cation contamination. YBa<sub>2</sub>Cu<sub>3</sub>O<sub>7</sub> has proved to accommodate various cationic and anionic substitutions [44]. Among these, substitution of Cu with metallic elements dramatically affects the nature of the high- $T_c$  superconductivity. In the YBa<sub>2</sub>(Cu<sub>1-x</sub>M<sub>x</sub>)<sub>3</sub>O<sub>7-δ</sub> system where M = Ti, Cr, Mn, Fe, Co, Ni, Ga and Zn, 3 ~ 10% of metal contamination can reduce the  $T_c$  value below the boiling temperature of liquid nitrogen [45–49]. Table 2-1 shows the  $T_c$  values reported for YBa<sub>2</sub>(Cu<sub>1-x</sub>M<sub>x</sub>)<sub>3</sub>O<sub>7-δ</sub> systems. The third important aspect of buffer layers is the mechanical stability and proper adhesion to the metal substrate. For this reason, the lattice constant of the buffer layer should provide a reasonable match with both the metal substrate and HTS materials. The thermal expansion coefficient of the buffer layer also needs to be considered.

Buffer layer materials has also been studied for the microelectronic applications of superconducting devices such as superconductor-normal metal-superconductor (S-N-S) junctions or superconductor-insulator-superconductor (S-I-S) tunnel junctions. In these

applications, the starting substrates were single crystal materials such as Si, sapphire ( $\text{Al}_2\text{O}_3$ ), GaAs, MgO or  $\text{SrTiO}_3$ . It is difficult to grow high temperature superconducting thin films directly on these substrates because of interdiffusion and the lattice mismatch between them. Several buffer layers were explored for the superconducting microelectronic devices such as MgO [50~52],  $\text{SrTiO}_3$  [53~55],  $\text{Y}_2\text{O}_3$  [56,57], Yttria-stabilized zirconia (YSZ) [58~60],  $\text{CeO}_2$  [61],  $\text{ZrO}_2$  [62~64]. In the RABiTS application for 2G wire technique, YSZ /  $\text{CeO}_2$  multilayer buffer scheme on Ni tape was proposed by Norton *et al.* in 1996 [65]. In this architecture, the  $\text{CeO}_2$  layer is the epitaxial template, and YSZ has a role of alleviating oxide cracks. All of the multilayer buffer films were grown by pulsed laser deposition (PLD) method using a KrF excimer laser. After  $\text{YBa}_2\text{Cu}_3\text{O}_7$  formed on this buffer scheme, the superconducting transition temperature ( $T_c$ ) was observed at 88 K and the critical current density ( $J_c$ ) for these initial RABiTS structures was  $7 \times 10^5 \text{ A/cm}^2$  at 77 K, 0 T. These results were comparable to those obtained for the epitaxial films on single crystal substrates. In order to retard metal oxidation effectively and overcome the slow deposition rate of PLD method, Pd deposition directly on Ni surface and electron beam evaporation deposition method for the multilayer buffer scheme were proposed. Goyal *et al.* obtained  $J_c$  value of  $3 \times 10^5 \text{ A/cm}^2$  at 77 K, 0 T by using PLD deposited YBCO / YSZ /  $\text{CeO}_2$  buffer scheme on e-beam evaporated Pd on Ni tape [35]. Paranthaman *et al.* proposed e-beam evaporated YSZ /  $\text{CeO}_2$  buffer layers on Ni tape with crack free  $\text{CeO}_2$  thin film of 3~10 nm thickness [66]. Furthermore, He *et al.* studied YSZ /  $\text{CeO}_2$  buffer layers on Ni tape by using RF or DC magnetron sputtering method [67]. Mathis *et al.* could get superconducting properties of  $T_c$  around 88 K,  $J_c$  exceeding  $3 \times 10^6 \text{ A/cm}^2$  at 77 K, 0 T by adapting RF sputtered YSZ

and e-beam evaporated  $\text{CeO}_2$  multilayer scheme [68]. Another buffer scheme using transition metal nitride film was reported by Kim *et al.* in 2002 [69]. In this report, TiN was chosen because of low electrical resistivity ( $20\sim 30\ \mu\Omega\cdot\text{cm}$ ) and good mechanical strength (Young's modulus : 600 GPa, micro-hardness :  $2000\ \text{Kg/mm}^2$ ). Due to the oxidation of TiN layer during YBCO deposition,  $\text{CeO}_2$  layer also applied between YBCO and TiN films. The TiN layer was formed by DC reactive sputtering with  $\text{Ar/N}_2$  mixture gas and the  $\text{CeO}_2$ , YBCO layers were grown by PLD method. A superconducting transition temperature for this architecture was 89 K and the critical current density was  $6\times 10^5\ \text{A/cm}^2$  at 77 K. Because TiN is also known as Cu diffusion barrier [70], Cantoni *et al.* studied multi buffer scheme using TiN for Cu based RABiTS process [71]. In this report,  $\text{LaMnO}_3$  /  $\text{MgO}$  / TiN buffer architecture was proposed.  $\text{MgO}$  layer was chosen for oxygen diffusion barrier, and  $\text{LaMnO}_3$  layer proved to be a planarizing material for smooth growing of YBCO. Table 2-2 shows the list of buffer layer materials tested with RABiTS applications referred from [42].

## **2.3 Review of Conducting Oxide Buffers for Cu based YBCO Coated Conductors**

### **2.3.1 Introduction**

Since the high temperature superconductors (HTS) were discovered in the late 1980s, worldwide efforts have been made to achieve high-efficiency electric wires. The first generation (1G) multifilamentary HTS wires are composites which can be produced with  $\text{Bi}_{2-x}\text{Pb}_x\text{Sr}_2\text{Ca}_2\text{Cu}_3\text{O}_{10}$  (known as BSCCO-2223) and silver or silver alloy. BSCCO based HTS wire has shown a critical current density above  $100,000\ \text{A/cm}^2$  at 77 K [72]. Critical current density ( $J_c$ ) is one of the limiting parameters of superconductivity, above which superconductivity disappears. Bi-Sr-Ca-Cu-O system has a high critical

temperature ( $T_c$ ) value as high as 110 K with no rare earth elements [73]. The fabrication method of superconducting tapes with BSCCO and silver is known as powder-in-tube (PIT) process. The high-purity mixture of  $\text{Bi}_2\text{O}_3$ ,  $\text{PbO}$ ,  $\text{SrCO}_3$ ,  $\text{CaO}$  and  $\text{CuO}$  powder is filled into a silver tube and continuously drawn into a narrow cylinder of about 1mm diameter. Such filaments are rolled together and deformed into a tape. Then a final annealing procedure is performed to react and obtain the tapes with good superconducting properties [74].

In order to overcome the high production cost - \$300/kA-m - of 1G wires,  $\text{YBa}_2\text{Cu}_3\text{O}_{7-8}$  (YBCO) based second generation (2G) wires or tapes are widely being developed in both laboratories and industries [75]. 2G wires have the advantages of lower cost and better electrical performance under applied magnetic fields. The 2G wire with YBCO HTS on RABiTS architecture used by American Superconductor Corporation Inc. (AMSC) is made up of 3 buffer layers scheme on textured Ni-W (5 at.%) tape [76].  $\text{Y}_2\text{O}_3$  which can be formed by electron beam evaporation technique serves as a seed layer on 75 $\mu\text{m}$  thick Ni-W metal substrate. Yttrium-stabilized zirconia (YSZ) is deposited as a barrier layer. Due to the low level of lattice mismatch with YBCO ( $\sim 0.12\%$ ),  $\text{CeO}_2$  plays a role as a cap layer. Both YSZ and  $\text{CeO}_2$  layers are deposited by an rf-sputtering method. Each buffer layer has a thickness of 75nm. The YBCO film, with the thickness of about 1 $\mu\text{m}$ , is deposited on this buffer stack by metal organic decomposition (MOD) method using trifluoroacetate (TFA) based precursors. Silver is deposited on YBCO film with 3 $\mu\text{m}$  thickness for capping the superconductor layer. Finally, a 75 $\mu\text{m}$  thick Cu film is bonded for mechanical and electrical stability. The Ag cap layer and Cu stabilizer can also serve as a current shunting path in the event of local defects existing in the YBCO



film. This shunting current cannot flow through the buffer layers because they are all insulators. Figure 2-14 is the schematic drawing of this YBCO based 2G wire architecture, and Figure 2-15 is the SEM cross-section of AMSC's 2G wire.

Nickel, which is the starting template of 2G wires, is ferromagnetic (FM) with a Curie temperature of 631 K and a saturation magnetization of  $0.51 \times 10^6$  A/m at 0 K [77]. The magnetic metal substrate, such as Ni, can cause significant hysteretic losses during application of alternating current (ac). The ac loss can be decreased by adding W to Ni [78]. The Ni-W (5 at.%) alloy shows the Curie temperature of 339 K [79] and also increases the yield strength of the substrate to 165 MPa compared to pure Ni substrate of 34 MPa [78]. However, the Ni-W (5 at.%) alloy tape is not nonmagnetic at 77 K. In this aspect, Cu substrate is an attractive candidate for the starting template of 2G wires. Cu is a diamagnetic material that shows no ac loss phenomenon. Cu also surpasses Ni alloy in the electrical conductivity characteristics. At 300 K, the resistivity of Cu tape is  $1.5 \times 10^{-6}$   $\Omega \cdot \text{cm}$ , which is lower than Ni-W (3 at.%) alloy tape of  $2.5 \times 10^{-5}$   $\Omega \cdot \text{cm}$ . At the temperature of liquid nitrogen 77 K, Cu tape and Ni-W (3 at.%) tape show the resistivity value of  $2.0 \times 10^{-7}$   $\Omega \cdot \text{cm}$  and  $1.7 \times 10^{-5}$   $\Omega \cdot \text{cm}$  respectively. Figure 2-16 is the resistivity curves of Cu tape and Ni-W (3 at.%) alloy tape as a function of temperature. Cu tape has {100}<100> cube texture and obtained from randomly oriented metal bars by cold-rolling, followed by an anneal in vacuum at 800°C for 1 h.

In this 2G wire architecture, the YBCO layer is located in the neutral axis between the 77~78 $\mu\text{m}$  thick Ni alloy substrate with 3 buffer layers, and the 77~78 $\mu\text{m}$  thick Ag cap layer with Cu stabilizer. The total thickness of the wire is slightly more than 150 $\mu\text{m}$ . For determining the critical current density ( $J_c$ ), we divide the electrical current value by the

cross-sectional area of YBCO which carries the super current in its superconducting state. The overall engineering critical current density ( $J_E$ ) deals with the current value through the whole cross-sectional area of the wire including not only YBCO but also the substrate, buffer layers, cap layer and stabilizer. One way of increasing the  $J_E$  value is to reduce the total wire thickness. This can be done by reducing the thicknesses of both the silver cap layer and copper stabilizer, which accounts for half of the total thickness [80]. In this case, the remaining problem is that we have to supply a shunting current path through the starting metal substrate. The current 2G wire structure consists of insulating buffer layers, which means that there is no shunting current path if there is no metallic capping layer on the YBCO film. In order to make the current flow through the metal substrate without capping layer, there must be a conductive buffer layers between the HTS layer and the metal substrate.

Compared to Ni or Ni based alloy tapes for 2G wire technology, several profitable aspects can be found in Cu substrates. Cantoni *et al.* have reported that the thermal stability of coated conductor has the relations with the capping layer thickness and the engineering current density [80]. Figure 2-17 and 2-18 are the simulated graphs of capping layer thickness and engineering current density as a function of the current-width values. The expressions for the capping layer thickness ( $d_c$ ) and engineering current density ( $J_E$ ) are:

$$d_c = \rho_c[(K^2/w) - (d_s/\rho_s + d_m/\rho_m)],$$

$$J_E = K/\{d_s + d_m + \rho_c[(K^2/w) - (d_s/\rho_s + d_m/\rho_m)]\},$$

where  $\rho_c$ ,  $\rho_s$ , and  $\rho_m$  are the resistivities of capping layer ( $\rho_c : 2.0 \times 10^{-7} \Omega\text{-cm}$  for Cu or Ag), superconducting film ( $\rho_s : 5.0 \times 10^{-5} \Omega\text{-cm}$ ), and metal substrate ( $\rho_m : 2.0 \times 10^{-7} \Omega\text{-cm}$ )

for Cu and  $4.5 \times 10^{-7} \Omega\text{-cm}$  for Ni).  $K$  is the current flow per tape width and  $w$  is the critical heat flux of the liquid nitrogen at 77 K ( $w$  : 10-20 W/cm<sup>2</sup>) [81]. The thicknesses of superconducting film and metal substrate are designated by  $d_s$  ( $d_s = K/J_s$ ,  $J_s$  : current density flown through the superconductor) and  $d_m$  ( $d_m$  : 50 $\mu\text{m}$ ). According to these graphs, no capping layer is needed up to  $K \sim 500 \text{ A/cm}$  in the case of Cu tape and the maximum  $J_E$  can be obtained up to  $\sim 90 \text{ kA/cm}^2$  for Cu tape which is higher than the value for Ni tape ( $\sim 60 \text{ kA/cm}^2$ ). The advantages of Cu tape (nonmagnetic, lower material cost ( $\sim 20\%$  of Ni), easy formation of a sharp cube texture [82] and higher electrical and thermal conductivity (for Cu,  $k$  : 398 W/m-K and for Ni,  $k$  : 90 W/m-K)) as compared to Ni or Ni based alloy tapes can improve the 2G wire properties along with the conductive buffer layers which offers fully conductive wire architecture. In this review, the possible problems of Cu based RABiTS process and overview of conductive buffer oxides will be addressed.

### 2.3.2 Preventing Methods of Cu Oxidation

In recent research, Aytug *et al.* demonstrated SrRuO<sub>3</sub> (SRO) / LaNiO<sub>3</sub> (LNO) as a conductive buffer structure for Ni based coated conductors [83]. Both SRO and LNO are perovskite type conductive oxides that show metallic behavior. The room temperature resistivity of SRO film is  $\sim 1.8 \times 10^{-4} \Omega\text{-cm}$  and  $\sim 3.0 \times 10^{-5} \Omega\text{-cm}$  at 4 K [84]. LNO has a resistivity of  $1.8 \times 10^{-3} \Omega\text{-cm}$  at 290 K and  $5 \times 10^{-4} \Omega\text{-cm}$  at 4.2 K [85]. Pulsed laser deposition (PLD) method of YBCO on these conductive buffers is done at high temperatures ( $\sim 780^\circ\text{C}$ ) and high oxygen partial pressures ( $\sim 2 \times 10^{-1}$  Torr). These growth condition offer an oxidation environment to the metal substrate. From the work of Aytug *et al.*, Ni substrate oxidation could be observed from XRD and cross-sectional SEM

analysis. Though the Cu based RABiTS process with the conductive buffer architecture has advantages, the oxidation problem could be worse. Figure 2-19 shows the thermodynamic stability curve which indicates that even  $\sim 1 \times 10^{-6}$  Torr of oxygen in the system at YBCO growing temperature can cause copper oxidation. Aytug *et al.* reported that  $\text{La}_{0.7}\text{Sr}_{0.3}\text{MnO}_3$  (LSMO) could be used as a conductive buffer layer on Cu based RABiTS applications [86]. In this work, they chose a Ni layer on metal substrate to prevent Cu oxidation. However, there are still remaining problems such as ferromagnetism of the Ni layer and NiO formation at the interface between substrate and buffer layer.

In metallurgical applications, enhancement of Cu oxidation resistance has been investigated by several approaches, including alloying or implanting elements such as Mg, Cr and Al that are known to be oxygen getters [87~92]. Among these, the Mg-Cu and Al-Cu systems are perhaps the most attractive due to the limited solubility of Cr in Cu [93]. The use of Mg-doped Cu films as an oxygen diffusion barrier is being investigated for Cu metallization in Si integrated circuit technologies [94]. Unfortunately, the resistivity of Cu increases rapidly with dopant concentration, deterring the use of an alloy as the RABiTS's substrate material if shunting functionality is desired. However, Mg-Cu or Al-Cu alloy thin film on the Cu substrate may prove to be suitable since the effective electrical transport path length would be limited to a thin surface layer.

Another method of preventing Cu oxidation is applying a noble metal as an oxygen barrier between metal substrate and conductive oxide buffer layers. One of the candidate material is iridium (Ir) which has face centered cubic (fcc) crystal structure and lattice parameter of  $3.840\text{\AA}$ . In the crystallographic aspect, iridium can be well matched with

Cu substrate. Because iridium is a well known platinum group metal with excellent oxidation resistance, oxidation behavior is only considered above 1400°C [95~97].

Although the iridium oxides ( $\text{IrO}_2$ ) are formed after the YBCO deposition, it has good metallic property with resistivity below  $3 \times 10^{-4} \Omega \cdot \text{cm}$  at room temperature [98].

Paranthaman *et al.* first tried Ir as an oxygen barrier on Ni-W alloy based RABiTS application [99]. In their research,  $\text{La}_{0.7}\text{Sr}_{0.3}\text{MnO}_3$  conductive buffer layer was used to form fully conductive buffer architecture. On the other hand, careful consideration is also needed, because oxygen diffusivity through Ir is  $5 \times 10^{-12} \text{ cm}^2/\text{s}$  at 800°C [78]. There is also a possibility of Cu diffusion through the Ir layer. Cu and Ir are known to be soluble in extremely small amounts [100]. However, 50  $\mu\text{m}$  thick Cu substrate can continuously supply copper element to the thin Ir layer during buffer oxides and YBCO processes. These mean that Cu oxidation can be observed either on top of the YBCO film or on the Cu substrate, and proper thickness of Ir layer should be deposited. Another candidate material for preventing Cu oxidation is Pd (palladium). Pd could be a good layer, but there is also an issue with miscibility in the Cu-Pd system.

### 2.3.3 Thin Film Techniques for Oxides Growth

In order to fabricate HTS coated conductors, not only the buffer oxides but also superconducting oxides can be grown by various deposition techniques. These techniques include sputtering, electron beam evaporation, pulsed laser deposition (PLD), and non-vacuum deposition method known as chemical solution deposition (CSD).

Sputter deposition is a physical vapor deposition (PVD) technique that has been used widely for thin film growth, especially in the semiconductor industries. Metal films, such as Al, Ti, and W, are sputter deposited for interconnection or metallization

applications. Usually Ar gas is introduced into the vacuum chamber (from few milli Torr to tens of milli Torr of pressure). The positively charged  $\text{Ar}^+$  ions generated by the potential difference between the cathode and anode electrodes bombard the negatively charged target materials. The ejected target elements from these collisions are deposited on the surface of the heated substrate materials. Radio frequency (RF) sputtering is the common way of depositing ceramic materials. Due to the phenomenon of impedance drop of dielectric materials in the high-frequency plasma, the current can flow through the dielectrics. A negatively self-biased target that results from a mobility difference between oscillating electrons and ions enables the insulating ceramic materials to be sputtered [101]. According to the Lorentz force, the path of each charged particle flowing one direction is bent by applying magnetic field. Electrons affected by magnetic field in the plasma move with spiral motion which is called as helix movement. This increases the ion density due to enhanced possibility of collision with gas elements. In other words, deposition pressure can be lowered maintaining the efficiency of sputtering yield. The deposition rate also can be improved with the same applied voltage. These are the advantages of magnetron sputtering. Figure 2-20 shows the schematic drawings of a planar type magnetron sputtering system. In the HTS coated conductor applications various buffer oxides such as YSZ [102],  $\text{CeO}_2$  [103],  $\text{LaMnO}_3$  [104],  $\text{SrRuO}_3$ ,  $\text{LaNiO}_3$  [83],  $\text{La}_{0.7}\text{Sr}_{0.3}\text{MnO}_3$  [99] are epitaxially grown by the DC or RF sputtering methods. High deposition rate of sputtering system makes it useful for manufacturing long length wires.

Electron beam (e-beam) evaporation is one approach to evaporation deposition. In thermal evaporation, materials that needs to be deposited are placed in a crucible and

heated by a resistive heater. The vapor atoms are transferred to the substrates in the vacuum chamber at pressures typically less than  $1.0 \times 10^{-3}$  Torr [105]. Due to the contamination problem of the crucible material at high temperatures, there is a limitation of using resistively heated evaporation sources. In the case of electron beam evaporation, contamination from the crucible and heating element can be drastically reduced by using shielded heating filaments [101]. The electrons thermionically emitted from this shielded heating filaments are deflected by a transverse magnetic field and reach the surface of the charged material. The evaporation starts by this electron beam heating of the source material. Figure 2-21 is a conceptual drawing of an electron beam evaporation system. Evaporation of MgO [106, 107],  $Y_2O_3$  [108],  $CeO_2$  [109] are performed by the electron beam evaporation method for HTS buffer layers.

Pulsed laser deposition (PLD) is one of the commonly used methods for growing oxides. A KrF excimer is the most popular laser source [110]. A KrF excimer laser produces ultra violet (UV) light of 248nm wave length. The laser energy is absorbed by the target material and ablates the target atoms. The ejected atoms generate a plume and travel to the heated substrate material. The distance from the target to the substrate must be considered with respect to the background pressure and ambient gas pressure. Multi-layered buffer oxides with various thickness range can be grown by shifting each target material without vacuum break and by changing the repetition rate. Figure 2-22 shows the schematic drawing of a simple PLD system. Due to its simplicity and ablating performance, most of the buffer oxides for HTS application can be deposited by PLD method.  $CeO_2$  [111], YSZ [112], MgO [113],  $LaMnO_3$  [113], TiN [113] buffer layers deposited by PLD for HTS application have been reported. The limited laser plume size

and the pulsed deposition mechanism can be a drawback of large scale fabrication of HTS coated conductors. However, high-rate pulsed laser deposition (HR-PLD) method has been proposed by Usoskin *et al.* [114].

Chemical solution deposition (CSD) under non-vacuum condition has great advantages because of low cost and high deposition rate. The general procedures of CSD are synthesis of precursor solution, deposition by spin coating, formation of amorphous film by pyrolysis of organics and crystallization of the coating by high temperature heat treatment [115]. Sol-gel process using 2-methoxyethanol ( $\text{CH}_3\text{OCH}_2\text{CH}_2\text{OH}$ ) as a reagent of metal-oxygen-metal bond formation, and metal organic decomposition (MOD) process using carboxylate compounds as a metal cation source are the common CSD approaches. In the semiconductor industries, sol-gel process is widely used for deposition of TEOS (tetraethyl orthosilicate) oxide as an inter-metallic dielectrics (IMD).  $\text{BaZrO}_3$  [116],  $\text{La}_2\text{Zr}_2\text{O}_7$  [117], and  $\text{CeO}_2$  [118] buffer layers have been investigated by CSD method.

Finally, ion beam assisted deposition (IBAD) can be used in the case of polycrystalline metal substrates in order to form the textured template for the buffer oxides. IBAD YSZ and IBAD MgO are the most common templates for producing 2G tapes [119].

### 2.3.4 Overview of Conductive Oxides for HTS Coated Conductors

An important aspect when considering epitaxial buffer oxides for HTS coated conductors is lattice match with the c-axis aligned YBCO layer. Many of the conducting oxides are in the category of perovskite crystal structure possessing a pseudo-cubic lattice parameter which matches well with the a, b axes of YBCO ( $a=0.382\text{nm}$ ,  $b=0.389\text{nm}$ ).

The Perovskite structure consists of two metallic cations and three oxygen atoms ( $\text{ABO}_3$ ). The large A atoms occupy each corner of the lattice and oxygen atoms sit on



each face center with small B atoms in the lattice center, completing mostly orthorhombic crystal structure. From another frame of view, the small B atoms are surrounded by 6 oxygen atoms forming  $\text{BO}_3$  (charge sharing notification) octahedron. This octahedron connects to other octahedra placing large A atom in the middle of their connection. This forms a pseudo-cubic structure. The A and B atoms are selected to make the charge balance. Figure 2-23 is the drawing of a typical perovskite lattice structure. The A site atoms can be cerium (Ce), calcium (Ca), sodium (Na), strontium (Sr), lead (Pb) and rare earth metals. The B site atoms can be titanium (Ti), niobium (Nb), iron (Fe), nickel (Ni), ruthenium (Ru), manganese (Mn), cobalt (Co), chromium (Cr) or copper (Cu) which are normally in the transition metal category.

The metallic, insulating and metal-insulator transition properties of a large number of perovskite oxide compounds have been explained by the framework model which includes correlation effects [120, 121]. The band widths  $W$  of occupied oxygen 2p states and metal's d orbitals, the energy difference between oxygen 2p and the lowest unoccupied metal orbital which is designated as  $\Delta$ , and the energy difference between the lowest unoccupied metal orbital and the highest occupied metal orbital which is designated as  $U'$  are the three terms that can be used in this model. Figure 2-24 is the schematic diagram of the Zaanen, Sawatzky and Allen (ZSA) framework. If the band width  $W$  is larger than  $\Delta$  or  $U'$  as shown in the left and right end side of figure 2-24, the oxides are conductive. The left end side of figure 2-24 designates the overlap of the occupied 2p oxygen valence band with unoccupied metal conduction band, and the right end side designates the overlap of the occupied and unoccupied metal orbitals. In each case partially filled metal orbitals contribute to charge transfer. If  $U'$  is greater than  $\Delta$ , the

oxide is called a charge-transfer insulator. If  $\Delta$  is greater than  $U'$ , the oxide is a Mott-Hubbard insulator.

Lanthanum nickelate ( $\text{LaNiO}_3$ ) is a conductive perovskite oxide with pseudo-cubic lattice parameter of 0.383 nm.  $\text{LaNiO}_3$  is metallic due to the charge transfer gap  $\Delta$  closing, which means that the occupied oxygen 2p orbitals and unoccupied 3d Ni orbitals are overlapped. A metal to insulator transition can be occurred in the oxygen deficient phase ( $\text{LaNiO}_{3-x}$ ) [122], and controlling of oxygen stoichiometry is important. Sputter deposited  $\text{LaNiO}_3$  buffered structure (YBCO /  $\text{LaNiO}_3$  / Ni tape) and multilayer buffer scheme (YBCO /  $\text{SrRuO}_3$  /  $\text{LaNiO}_3$  / Ni tape) are reported as conductive buffer oxides for Ni-based RABiTS [123, 83]. The  $\text{SrRuO}_3$  layer is used to prevent Ni diffusion through YBCO which can affect degradation of the  $T_c$  value.

The perovskite  $\text{SrRuO}_3$  has lattice constants of  $a = 0.555$  nm,  $b = 0.556$  nm,  $c = 0.786$  nm, and  $a$ ,  $b$  lattice constants are close to  $\sqrt{2} a_{\text{YBCO}}$  or  $\sqrt{2} b_{\text{YBCO}}$  with pseudo-cubic lattice parameter of 0.393 nm. The conductive property of  $\text{SrRuO}_3$  comes from the overlap between oxygen anion p orbitals and cation  $t_{2g}$  [124]. Metallic  $\text{SrRuO}_3$  is also ferromagnetic with a Curie temperature of  $\sim 160^\circ\text{K}$  [125]. There have been several reports of  $\text{SrRuO}_3$  buffer layers as diffusion barriers on Pt [126] and Ni [127~129] for HTS coated conductor applications.

$(\text{La}_{1-x}\text{A}_x)\text{MnO}_3$  is the interesting compound system which has both metallic and ferromagnetic properties. A represents a divalent alkali elements such as Sr, Ca or Ba. In the extreme composition of  $\text{LaMnO}_3$ , La and Mn must have 3+ charges in accordance with the 6- charge of three oxygen atoms.  $\text{LaMnO}_3$  is an insulating antiferromagnet where electrons are localized on the atomic orbitals [130]. When the La atoms are

replaced by divalent elements in the concentration range of  $0.2 < x < 0.4$ , it becomes ferromagnetic with metallic behavior. Zener explained this phenomenon by using a method called double exchange [131]. By hole doping (for example, replacing trivalent La by divalent Sr), this compound contains a considerable amount of  $\text{Mn}^{4+}$  ions. Charge transfer occurs by exchanging electrons between  $\text{Mn}^{3+}$  and  $\text{Mn}^{4+}$  ions via neighboring oxygen ion simultaneously. Sr doped  $\text{La}_{0.7}\text{Sr}_{0.3}\text{MnO}_3$  is a conducting perovskite oxide which has pseudo-cubic lattice parameter of 0.387 nm [132]. Aytug *et al.* reported a single conductive oxide buffer architecture using sputter deposited  $\text{La}_{0.7}\text{Sr}_{0.3}\text{MnO}_3$  films on Ni tape (YBCO / LSMO / Ni tape) [133] and on Cu tape (YBCO / LSMO / Ni / Cu tape) [86].

$\text{LaTiO}_3$  is an antiferromagnetic insulator ( $T_N \approx 150^\circ\text{K}$ ) when it has the fairly stoichiometric composition with trivalent  $\text{Ti}^{3+}$  ion. There exists a Mott-Hubbard energy gap  $E_g \approx U - W$  (see figure 2-24) which makes it an insulator. By changing the oxygen stoichiometry ( $\text{LaTiO}_{3+x}$ ), a mixed valent state of  $\text{Ti}^{3+}/\text{Ti}^{4+}$  can generate metallic transport properties [134, 135]. In the case of fully oxidized phase ( $\text{LaTiO}_{3.5}$  or  $\text{La}_2\text{Ti}_2\text{O}_7$ ), it becomes a ferroelectric band insulator.  $\text{LaTiO}_3$  has an orthorhombic perovskite structure with  $a = 5.604\text{\AA}$ ,  $b = 5.595\text{\AA}$  and  $c = 7.916\text{\AA}$  [136]. In contrast with  $\text{LaTiO}_3$ ,  $\text{La}_2\text{Ti}_2\text{O}_7$  shows monoclinic layered structure. According to the phase diagram study,  $\text{LaTiO}_{3+x}$  changes its electric and magnetic properties with oxygen content [137, 138].  $\text{LaTiO}_{3+x}$  is an attractive material for coated conductor application because it has good metallic property at all temperature ranges in the oxygen stoichiometric of  $0.1 < x < 0.25$  [137], and its pseudo-cubic lattice parameter is well matched with YBCO. However, the composition also can be changed during YBCO

growth in the high oxygen ambient ( $\sim 1 \times 10^{-1}$  Torr) at high temperature ( $\sim 780^\circ\text{C}$ ). The previous research on the relation of resistivity of  $\text{LaTiO}_{3+x}$  with oxygen pressure during deposition by PLD indicated that oxygen played a crucial role in conducting property [139]. Cation doping in the compound can overcome this oxygen sensitivity of  $\text{LaTiO}_{3+x}$ . Doping with divalent elements increases the  $\text{Ti}^{+3} / \text{Ti}^{+4}$  ratio and can make the compound less sensitive to ambient oxygen pressure during YBCO deposition. Electrical conductivity is a function of doping constant  $x$  in the  $\text{La}_{1-x}\text{Sr}_x\text{TiO}_3$  compound, and the resistivity continuously decreases with higher cation doping [140]. Previous studies on oxygen dependency showed that the room temperature resistivity of  $\text{La}_{0.5}\text{Sr}_{0.5}\text{TiO}_3$  remained below  $1.0 \times 10^{-3} \Omega\cdot\text{cm}$  in  $10^{-4} \sim 10^{-2}$  Torr of oxygen pressure range [141]. Recently, conductive buffer architecture with PLD deposited  $(\text{La},\text{Sr})\text{TiO}_3$  film on Cu based RABiTS application (YBCO / LSTO / Ir / Cu tape) was reported [142].

$\text{La}_{1-x}\text{Sr}_x\text{CoO}_3$  is the compound that has mixed valency due to the cation doping. The parent compound  $\text{LaCoO}_3$  is an insulator which has a charge transfer gap  $\Delta$  (see figure 2.24) formed between an occupied oxygen 2p band and an empty cobalt 3d  $e_g$  band [132]. By cation doping to  $\text{LaCoO}_3$ , the ratio of  $\text{Co}^{3+} / \text{Co}^{4+}$  increases introducing metallic behavior. The transport and magnetic properties depend on the doping concentration. The room temperature resistivity of  $\text{La}_{0.5}\text{Sr}_{0.5}\text{CoO}_3$  is known to be  $\sim 9 \times 10^{-5} \Omega\cdot\text{cm}$ . The pseudo-cubic lattice parameter of  $\text{La}_{0.5}\text{Sr}_{0.5}\text{CoO}_3$  is  $3.835\text{\AA}$ . The oxygen stoichiometry is an important parameter for resistivity control because oxygen deficiency can change the  $\text{Co}^{3+} / \text{Co}^{4+}$  ratio and the structural disorder in the Co-O-Co conduction channel [143].

$\text{LaCuO}_3$  is a compound which has  $\text{Cu}^{3+}$  ions. In a recent study, hybridization of unoccupied oxygen p states with Cu 3d and La 5d states was suggested as an electronic

structure of  $\text{LaCuO}_3$  [144]. The stoichiometric form of  $\text{La}_2\text{CuO}_4$  is an insulator. However, the conduction behavior of  $\text{LaCuO}_{3-\delta}$  alters from an insulator to metallic conductor with  $\delta$  ranging from 0 to 0.5. Although the nonstoichiometric  $\text{LaCuO}_{3-\delta}$  has high conductivity with available oxygen vacancies, it is not a desirable material due to difficulties of synthesis under high oxygen partial pressure. Yu *et al.* reported that Sr doping in the  $\text{LaCuO}_{3-\delta}$  compound stabilized the perovskite structure. Enhancement of conductivity was observed in  $\text{La}_{1-x}\text{Sr}_x\text{CuO}_{2-\delta}$  [145].

The overall electrical and structural properties of perovskite oxide compounds mentioned in this section is briefly shown in table 2-3. The major factor of selecting conductive buffer oxides for HTS coated conductor application should include not only the structural, chemical compatibility with metal substrate and YBCO film but also transport properties that need to be sustained even after the severe oxidizing process during YBCO formation.

Table 2-1. The critical temperature values in absolute temperature unit reported for  $\text{YBa}_2(\text{Cu}_{1-x}\text{M}_x)_3\text{O}_{7-\delta}$  systems.

x	Ti	Cr	Mn	Fe	Co	Ni	Zn	Ga	Ref.
0.1	75	84.5	78.9	38	21.2	66.3	< 3		45
0.033				61	55	80	70	51	46
0.1		86	92	50	50	73	40		47
0.033				76	73	55	55		48
0.033				88	88	80	58		49

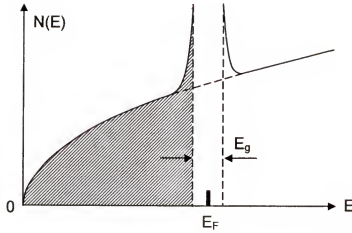
Table 2-2. The list of buffer layer materials tested with RABiTS applications.

Buffer Material	Cubic Lattice Parameter (Å)	% Lattice Mismatch versus YBCO	% Lattice Mismatch versus Ni	Oxygen Diffusivity (cm <sup>2</sup> /s) at 800°C	Electrical Resistivity (μΩ·cm)
MgO	4.210	9.67	17.74	$8 \times 10^{-22}$	
SrTiO <sub>3</sub>	3.905	2.16	10.26	$6 \times 10^{-11}$	
CeO <sub>2</sub>	5.411	0.12	8.22	$6 \times 10^{-9}$	
Y <sub>2</sub> O <sub>3</sub>	10.604	-1.89	6.22	$6 \times 10^{-10}$	
YSZ	5.139	-5.03	3.07	$2 \times 10^{-8}$	
TiN	4.242	10.43	18.49		20~30
LaMnO <sub>3</sub>	3.880	1.60	9.70	$8 \times 10^{-15}$	
Ni	3.524				5~6
Cu	3.615				1.5~2

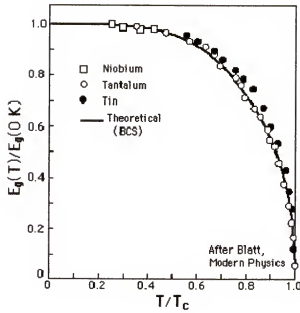
Table 2-3. The overall electrical and structural properties of perovskite oxide compounds mentioned in this section.

Material	Structure	Lattice Constant	Resistivity	Applications for Conductive Buffer Layer	Growth Method
$\text{LaNiO}_3$	rhombohedral [146] pseudo-cubic [147]	$a = 5.461 \text{ \AA}$ , $\alpha = 60.41^\circ$ $a = 3.83 \text{ \AA}$	$\sim 3 \times 10^{-4} \Omega \cdot \text{cm}$ @300 K $\sim 7 \times 10^{-5} \Omega \cdot \text{cm}$ @77 K	YBCO/LNO/Ni tape [123] YBCO/SRO/LNO/Ni tape [83] $T_c$ : 91 K $J_c$ : $1.3 \times 10^6 \text{ A/cm}^2$ @ 0T	rf magnetron sputtering
$\text{SrRuO}_3$	distorted orthorhombic [129] pseudo-cubic	$a = 5.573 \text{ \AA}$ , $b = 5.538 \text{ \AA}$ , $c = 7.586 \text{ \AA}$ $a = 3.93 \text{ \AA}$	$\sim 2 \times 10^{-4} \Omega \cdot \text{cm}$ @300 K [125] $\sim 5 \times 10^{-5} \Omega \cdot \text{cm}$ @77 K	YBCO/SRO/LAO [127] $T_c$ : 91 K $J_c$ : $3.0 \times 10^6 \text{ A/cm}^2$ @ 0T	PLD
$\text{La}_{0.5}\text{Sr}_{0.5}\text{MnO}_3$	rhombohedral or cubic [148]	$a = 3.88 \text{ \AA}$ [78]	$\sim 1 \times 10^{-3} \Omega \cdot \text{cm}$ @300 K [149] $\sim 2 \times 10^{-4} \Omega \cdot \text{cm}$ @77 K	YBCO/LSMO/Ni tape [133] YBCO/LSMO/Ni/Cu tape [86] $T_c$ : 91 K $J_c$ : $2.3 \times 10^6 \text{ A/cm}^2$ @ 0T	rf magnetron sputtering
$\text{La}_{0.5}\text{Sr}_x\text{TiO}_3$	orthorhombic ( $x < 0.3$ ) [140] cubic ( $x > 0.7$ )		if $x = 0.5$ $\sim 1 \times 10^{-4} \Omega \cdot \text{cm}$ @300 K [2,4,70]	YBCO/LSTO/Hr/Cu tape $T_c$ : 86 K $J_c$ : $1.0 \times 10^6 \text{ A/cm}^2$ @ 0T	PLD
$\text{La}_{0.5}\text{Sr}_{0.5}\text{CoO}_3$	distorted orthorhombic [132] pseudo-cubic	$a = 3.835 \text{ \AA}$	$\sim 5 \times 10^{-4} \Omega \cdot \text{cm}$ @300 K [143] $\sim 2.5 \times 10^{-5} \Omega \cdot \text{cm}$ @77 K		
$\text{LaCuO}_3$	distorted rhombohedral [150]	$a = 5.431 \text{ \AA}$ , $\alpha = 60.51^\circ$			
$\text{La}_{0.5}\text{Sr}_x\text{CuO}_{3.5}$	tetragonal ( $x = 0.2$ ) [145]	$a = 10.867 \text{ \AA}$ , $c = 3.857 \text{ \AA}$	$\sim 1 \times 10^{-4} \Omega \cdot \text{cm}$ @300 K [145]		





(a)



(b)

Figure 2-1. (a) Schematic drawing of energy gap in superconducting material, (b) the energy gap dependence on temperature with theoretical value versus experimental results for some elemental metals.

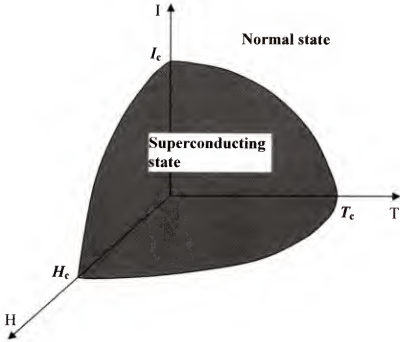


Figure 2-2. Schematic drawing of the critical space within which the superconductivity remains (T-H-I diagram).

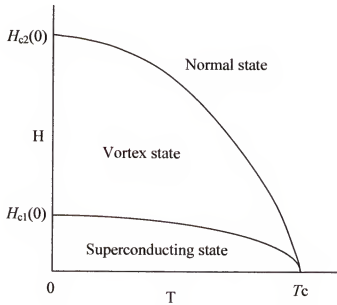


Figure 2-3. Phase diagram of type II superconductor with temperature and magnetic field dependency.

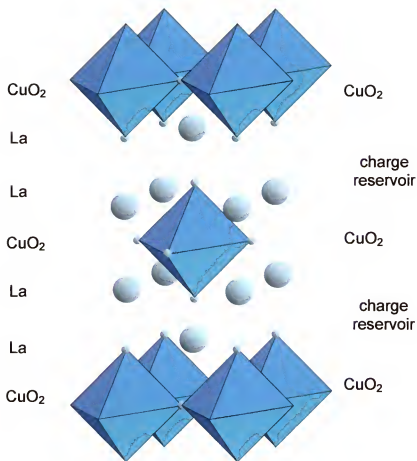


Figure 2-4. Schematic drawing of  $\text{La}_2\text{CuO}_4$ .

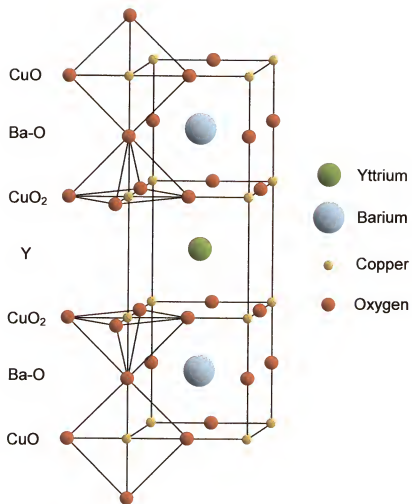


Figure 2-5. Schematic drawing of  $\text{YBa}_2\text{Cu}_3\text{O}_{7-\delta}$  unit cell combined with oxygen deficient perovskite structure.

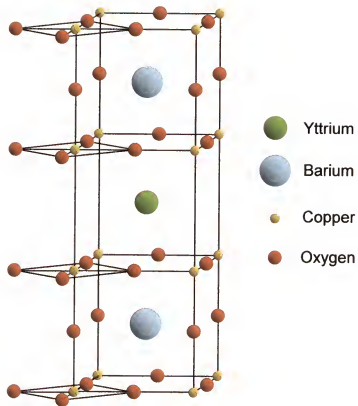


Figure 2-6. Schematic drawing of  $\text{YBa}_2\text{Cu}_3\text{O}_6$  compound which has different  $\text{CuO}$  chains with  $\text{YBa}_2\text{Cu}_3\text{O}_7$ .

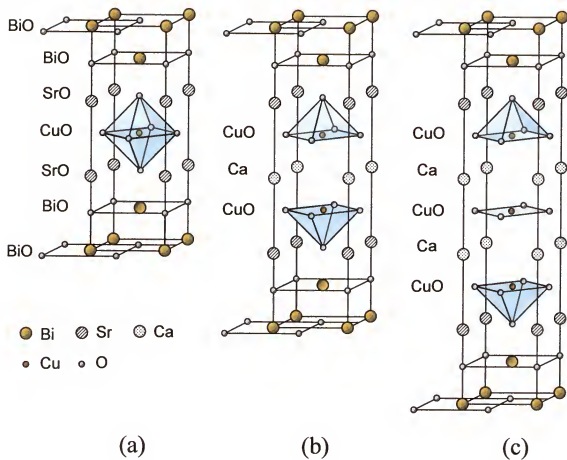


Figure 2-7. Schematic drawing of (a) Bi-Sr-Cu-O, (b) Bi-Sr-Ca-Cu-O (double Cu-O sheets), and (c) Bi-Sr-Ca-Cu-O (triple Cu-O sheets).

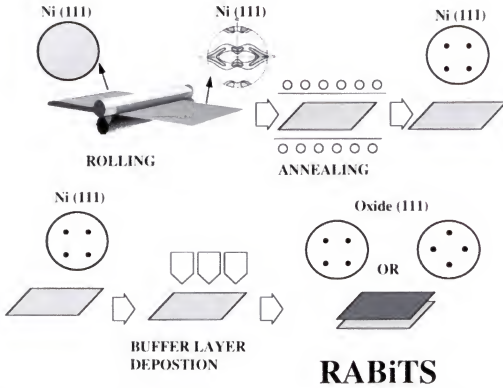


Figure 2-8. Conceptual drawing of rolling assisted biaxially textured substrate (RABiTS) process based on Ni substrate. The pattern inside the circle designates the texture alignment of the substrate.

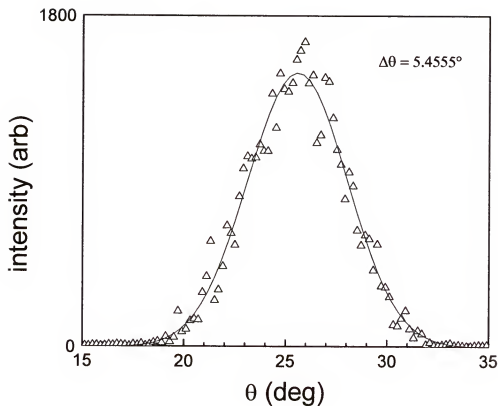


Figure 2-9. The X-ray diffraction  $\omega$ -scan (rocking curve) of (002) Ni which indicates the substrate's out-of-plane alignment. The full-width-half-maximum (FWHM) of the curve is  $5.4555^\circ$ .



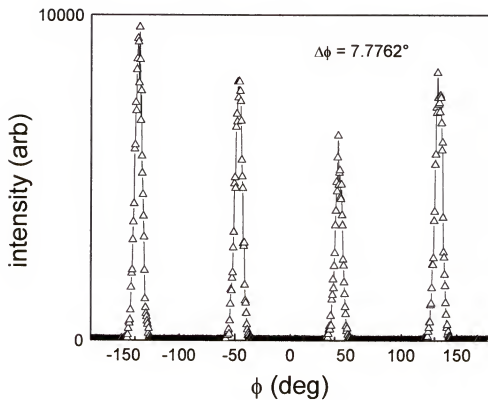


Figure 2-10. The x-ray diffraction  $\phi$ -scan of (111) Ni which indicates the substrate's in-plane alignment. The average full-width-half-maximum (FWHM) of the 4 peaks is  $7.7762^\circ$ .

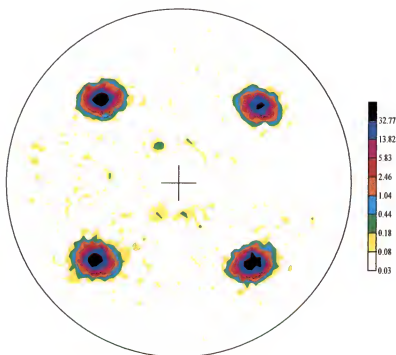
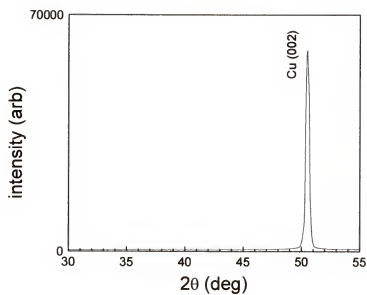
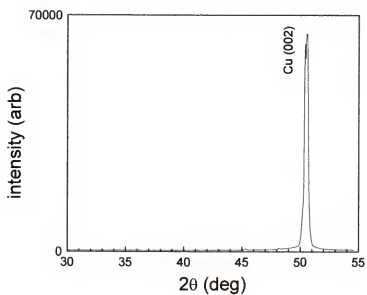


Figure 2-11. The log-scale (111) Ni pole figure of the Ni substrate formed by RABiTS process. The cube fraction of the substrate is 98.2694%.

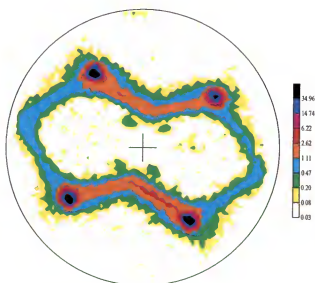


(a)

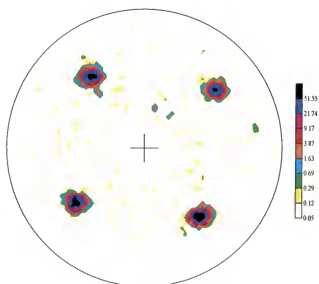


(b)

Figure 2-12. The X-ray diffraction  $\theta$ - $2\theta$  scan graphs of textured Cu tapes formed by RABiTS process (a) before annealing and (b) after annealing at  $800^\circ\text{C}$  in vacuum for 2 hours.



(a)



(b)

Figure 2-13. The log-scale pole figures of (111) Cu substrates (a) before annealing and (b) after annealing at 800°C in vacuum for two hours.

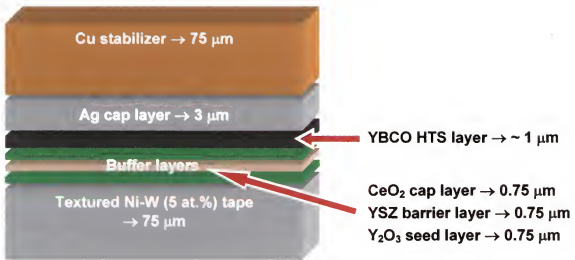


Figure 2-14. Schematic vertical structure drawing of conventional 2G wire based on YBCO HTS.

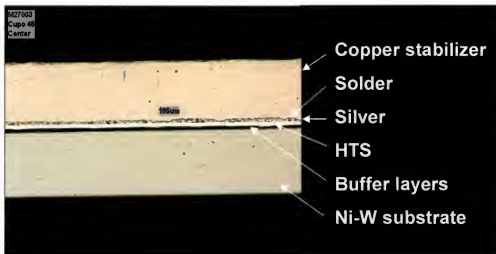


Figure 2-15. SEM cross-section of AMSC's 2G wire.

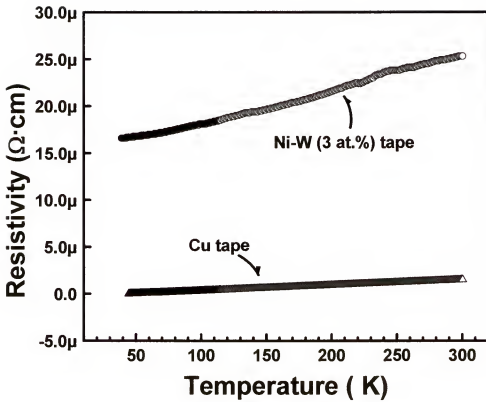


Figure 2-16. Resistivity comparison of Cu tape and Ni-W (3 at.%) tape as a function of the temperature.

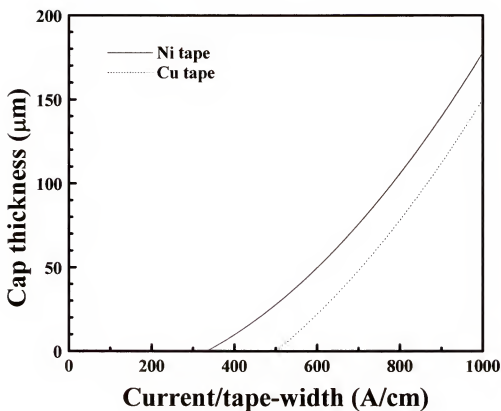


Figure 2-17. Simulated graph of cap layer thickness as a function of current per tape width.

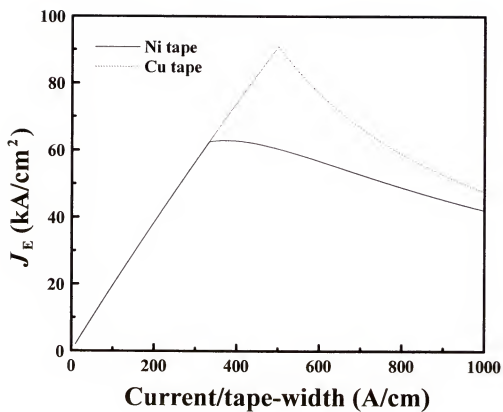


Figure 2-18. Simulated graph of engineering current density as a function of current per tape width.



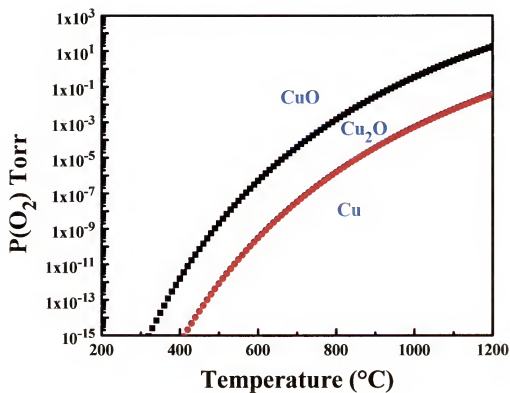


Figure 2-19. Thermodynamic stability curve of Cu in terms of temperature and oxygen partial pressure.

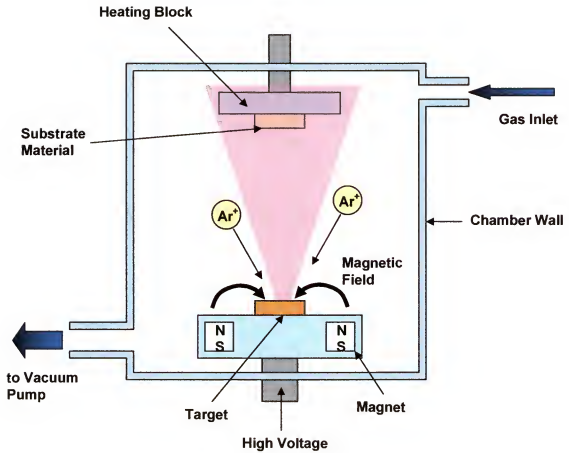


Figure 2-20. Schematic drawing of magnetron sputtering system.

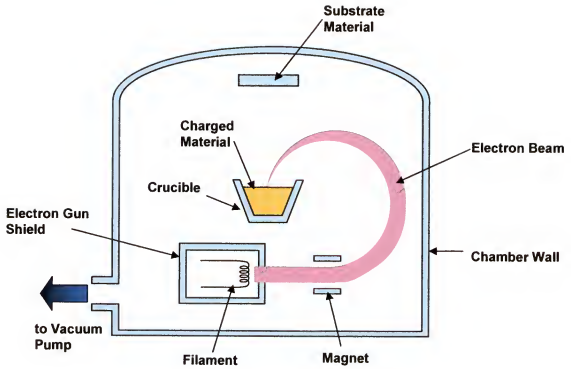


Figure 2-21. Schematic drawing of electron beam evaporation system.

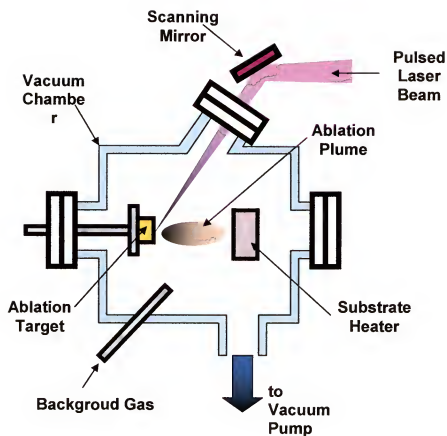


Figure 2-22. Schematic drawing of pulsed laser deposition system.

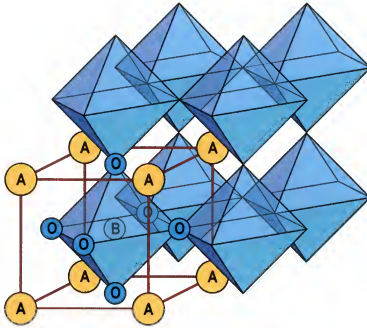


Figure 2-23. Schematic drawing of typical perovskite crystal structure.

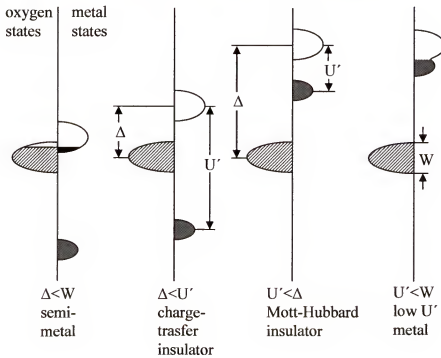


Figure 2-24. Schematic diagram of Zaanen, Sawatzky and Allen (ZSA) framework.

## CHAPTER 3

### GROWING EPITAXIAL $\text{Cu}_2\text{Mg}$ AS AN OXIDATION BARRIER FOR HIGH TEMPERATURE SUPERCONDUCTING COATED CONDUCTORS

#### 3.1 Introduction

High-temperature Superconducting (HTS) biaxially-textured coated conductors hold significant promise for the development of a superconducting wire technology functional at the liquid nitrogen temperatures (64-77 K). To date, this technology utilizes epitaxial  $\text{YBa}_2\text{Cu}_3\text{O}_7$  (YBCO) coatings deposited on biaxially-textured Ni or Ni-based alloy substrates [35][39][41][151]. These tape substrates are fabricated by thermo-mechanical deformation of the metals. While HTS wires based on the biaxially textured Ni substrates offer the promise of substantial energy savings for applications in the power sector, the actual impact of HTS wire will be determined by several factors, including the reliability of these conductors against catastrophic failure, as well as the potential limitations introduced via the use of ferromagnetic substrates. One approach that addresses both substrate ferromagnetism and supercurrent shunting is to use high conductivity Cu tapes as the base metal substrate. For use as a substrate for HTS coated conductors, the oxidation of the Cu substrate must be addressed. A significant issue with Cu is the oxidation of the metal substrate due to the following buffer oxide and YBCO depositions at the elevated temperature with high pressure of oxygen gas. The copper oxide ( $\text{Cu}_2\text{O}$ ,  $\text{CuO}$ ) growth occurs at the oxide-gas interface and the rate-determining step of oxidation is the diffusion of cation vacancies [152]. In general, the oxidation of Cu proceeds rapidly and at minimal oxygen partial pressure. At a temperature of 700°C,

Cu<sub>2</sub>O formation is favored for pure Cu exposed to oxygen pressures as low as  $10^{-8}$  Torr. A typical RABiTS is composed of several buffer layers such as CeO<sub>2</sub>, Y<sub>2</sub>O<sub>3</sub> and yttria-stabilized zirconia (YSZ). At the temperatures of YBCO deposition, these oxides cannot block oxygen diffusion causing the oxidation of Cu substrate. Copper oxide is not an effective passivation layer to further oxidation or scaling.

In metallurgical applications, enhancement of Cu oxidation resistance has been investigated by several approaches, including alloying or implanting elements such as Mg, Cr and Al that are known to be oxygen getters [87]-[92]. Among these, the Mg-Cu and Al-Cu systems are perhaps the most attractive due to the limited solubility of Cr in Cu [93]. The use of Mg-doped Cu films as an oxygen diffusion barrier is being investigated for Cu metallization in Si integrated circuit technologies [94]. Unfortunately, the resistivity of Cu increases rapidly with dopant concentration, deterring the use of an alloy as the substrate material if shunting functionality is desired. However, Mg-Cu or Al-Cu alloy thin film on the Cu substrate may prove suitable since the effective electrical transport path length would be limited to a thin surface layer. The phase diagram for the Cu-Mg binary alloy system indicates the presence of intermetallic Cu<sub>2</sub>Mg at the range of 15-18 weight % Mg up to 819°C [153]. The crystal structure of Cu<sub>2</sub>Mg is cubic fcc with the lattice constant  $a = 7.064 \text{ \AA}$  [154]. In addition the room temperature resistivity of Cu<sub>2</sub>Mg is known to be 5-6  $\mu\Omega\text{cm}$  which is compatible with that of Cu (1.67  $\mu\Omega\text{cm}$ ) [155]. One can therefore consider two variants of (Mg,Cu) buffer layers for Cu substrates, namely Mg-doped fcc Cu and the cubic Cu<sub>2</sub>Mg intermetallic. In order to assess the potential applicability of this approach to oxidation resistant buffers for

RABiTS-based conductors, we have investigated the epitaxial growth of (Cu,Mg) films on a (001) Cu surface.

### 3.2 Experiments

For these experiments, epitaxial (001) Cu films on (001) MgO single crystals were used as the substrate materials. The Cu films were grown using sputter deposition at a substrate temperature of 400°C with  $1.0 \times 10^{-2}$  Torr of Ar gas. The thickness of the epitaxial Cu film was 180nm. Due to the high vapor pressure of Mg (over  $2.0 \times 10^{-3}$  Torr at 400°C), in situ growth of epitaxial (Cu,Mg) films is not possible. The approach used to achieve epitaxy of a (Cu,Mg) film was to form Cu/Mg multilayer precursor films that would be subsequently annealed to form either Mg-doped fcc Cu or intermetallic  $\text{Cu}_2\text{Mg}$ . Sputter deposition was used to deposit Mg and Cu multilayers at room temperature with  $1.0 \times 10^{-2}$  Torr of Ar gas. The precursor consists of an Mg/Cu multilayer stack with 5 each of 25 nm thick Mg and 25 nm thick Cu layers, which were grown at room temperature by sputter deposition. Figure 3-1 shows the vertical structure, which is used for this experiment. The precursor is then annealed in a flowing  $\text{H}_2/\text{Ar}$  mixture at temperatures ranging from 400°C to 700°C. The development of (Cu,Mg) phases as the multilayer was investigated as a function of annealing temperature and duration.

### 3.3 Results and Discussion

At annealing temperature of 400°C, formation of the intermetallic  $\text{Cu}_2\text{Mg}$  was observed. Figure 3-2 shows a 2- $\theta$  X-ray diffraction scan along the surface normal for a multilayer structure annealed at 400°C. The strongest peaks, other than that from the substrate and epitaxial Cu film, correspond to  $\text{Cu}_2\text{Mg}$ . Both (111) and (001) oriented  $\text{Cu}_2\text{Mg}$  grains are observed. Interestingly, the (001) oriented component of the



intermetallic phase was found to be epitaxial with respect to the C layer. Figure 3-3 shows the X-ray diffraction rocking curve for the (004)  $\text{Cu}_2\text{Mg}$  peak, indicating a full-width half-maximum (FWHM) of  $\Delta\theta = 2.0^\circ$ , which is slightly larger than that for the Cu film ( $\Delta\theta = 1.45^\circ$ ). The in-plane orientation of the c-axis oriented  $\text{Cu}_2\text{Mg}$  was investigated using four-circle x-ray diffraction. Figure 3-4 shows an in-plane  $\phi$ -scan through the  $\text{Cu}_2\text{Mg}$  (222). The four-fold symmetric peaks indicate that the grains are epitaxial with respect to the Cu film, possessing a cube-on-cube orientation. The FWHM of the in-plane peaks is  $2.1^\circ$ . The cubic  $\text{Cu}_2\text{Mg}$  lattice parameter was measured to be  $7.016 \pm 0.005$  angstroms. At the upper end of the temperature range ( $600^\circ\text{C}$ ,  $700^\circ\text{C}$ ), only the (001) Cu peaks are observed. This is consistent with the formation of an epitaxial Mg-doped fcc Cu alloy. Figure 3-5 is the  $2\theta$  x-ray diffraction scan of the (Cu,Mg) multilayer after annealing at 400, 500, 600,  $700^\circ\text{C}$ . In order to confirm the oxidation resistance of the structures possessing (Cu,Mg) alloy films,  $\text{CeO}_2$  was deposited at elevated temperatures on Ni / (Cu,Mg) / Cu / MgO substrates and compared to  $\text{CeO}_2$  films on Ni / Cu / MgO. The  $\text{CeO}_2$  films were deposited by PLD at  $750^\circ\text{C}$ , and included a thin nucleation layer deposition in vacuum, followed by  $\text{CeO}_2$  deposition at  $2 \times 10^{-4}$  Torr of oxygen. In case of the  $\text{CeO}_2$  film on Ni / Cu / MgO, significant surface roughness due to the metal oxidation is observed. This is shown in figure 3-6. In contrast, no surface roughness is observed in the SEM image for the  $\text{CeO}_2$  / Ni / (Cu,Mg) / Cu / MgO structure.

### 3.4 Conclusions

The growth of epitaxial  $\text{Cu}_2\text{Mg}$  as an oxidation barrier for high temperature superconducting coated conductors was investigated. Epitaxy of (004)  $\text{Cu}_2\text{Mg}$  intermetallic phase was achieved on (002) Cu film. In-plane  $\phi$ -scan through the  $\text{Cu}_2\text{Mg}$

(222) and the x-ray diffraction rocking curve for the (004)  $\text{Cu}_2\text{Mg}$  peak indicates that the intermetallic phase is well oriented on (002) Cu surface.

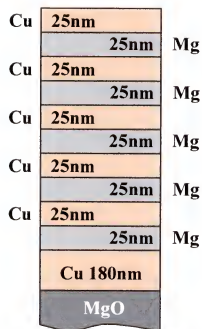


Figure 3-1. The vertical structure which is used for this experiment.

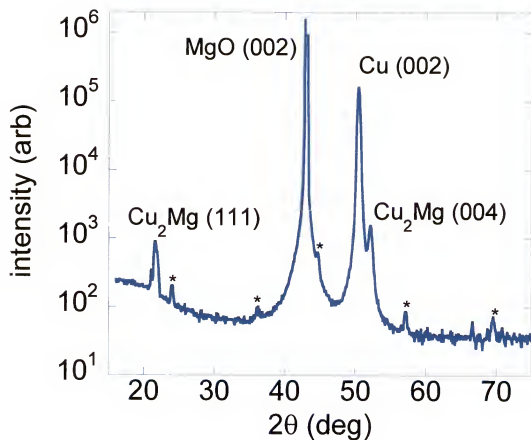


Figure 3-2. The X-ray diffraction  $\theta$ - $2\theta$  scan along the surface normal for a multilayer structure annealed at  $400^\circ\text{C}$ .

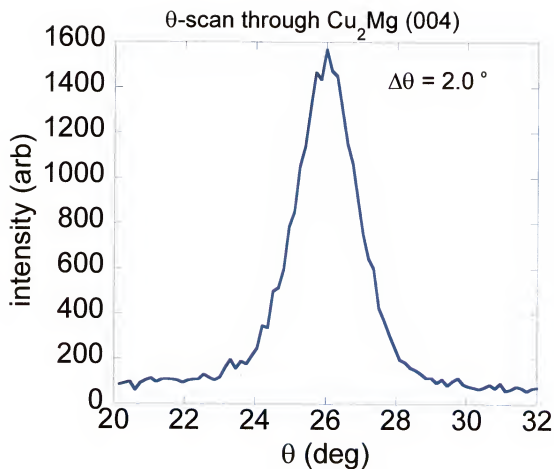


Figure 3-3. The X-ray diffraction rocking curve for the (004) Cu<sub>2</sub>Mg peak, indicating a full-width half-maximum (FWHM) of  $\Delta\theta = 2.0^\circ$ .

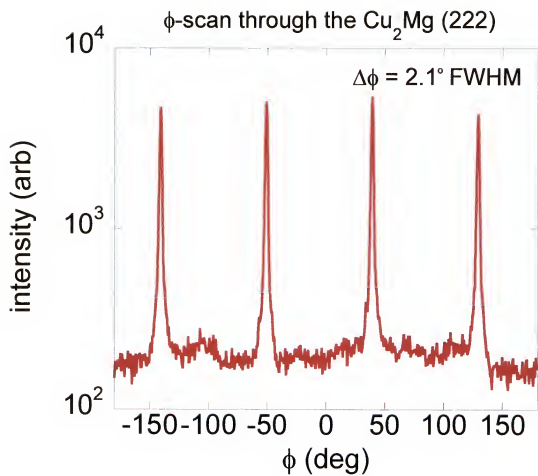


Figure 3-4. The X-ray diffraction  $\phi$ -scan through the  $\text{Cu}_2\text{Mg}$  (222).

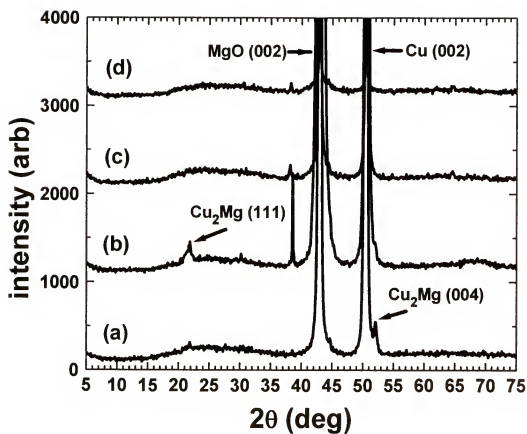


Figure 3-5. The X-ray diffraction  $\theta$ - $2\theta$  scan of the (Cu,Mg) multilayer after annealing at 400, 500, 600, 700°C.

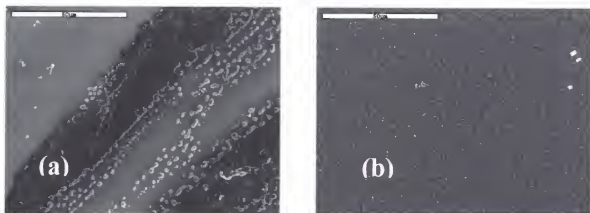


Figure 3-6. The SEM picture of (a)  $\text{CeO}_2$  film on  $\text{Ni} / \text{Cu} / \text{MgO}$  (b)  $\text{CeO}_2 / \text{Ni} / (\text{Cu}, \text{Mg}) / \text{Cu} / \text{MgO}$  structure.



## CHAPTER 4

### (LA,Sr)TiO<sub>3</sub> AS A CONDUCTING BUFFER LAYER FOR HIGH TEMPERATURE SUPERCONDUCTING COATED CONDUCTORS

#### 4.1 Introduction

Among the potential application of high-temperature superconductivity (HTS) are the power and utility sectors that will require high-current wires [8]. In the RABiTS (rolling assisted bi-axially textured substrate) approach, HTS coated conductors are made by deposition of buffer layers and superconducting oxide on a crystalline-textured metal tape. This approach is conducive to the development of electrically conductive buffer layers, which would provide a current shunt to the metal tape for improved protection. There are key issues for a conductive buffer layer of HTS coated conductors. First, it must be reasonably well lattice matched to both the metal substrate and the superconducting film, thus enabling epitaxy. Second, the interaction between the buffer layer and the metal substrate must be such as to minimize formation of any native interfacial oxide that would serve as an insulating barrier to shunted current flow. Although buffer layers of the conductive oxides La<sub>0.7</sub>Sr<sub>0.3</sub>MnO<sub>3</sub>, SrRuO<sub>3</sub> and LaNiO<sub>3</sub> on textured Ni tape have been reported [83,133], to date most buffer layers investigated for HTS conductors have been insulating, such as CeO<sub>2</sub> [156-158], Y<sub>2</sub>O<sub>3</sub>-ZrO<sub>2</sub> [68,151], [159,160], ZrO<sub>2</sub> [161], SrTiO<sub>3</sub> [162] and NiO [163], [164]. In the latter situation, protection must be accomplished by the addition of an adjacent normal metal layer that is sufficiently conductive and thick to accommodate the current flow without unmitigated growth of an unstable hot zone.

An alternative candidate material system that may satisfy the criteria for conductive buffers mentioned above is  $(\text{La,Sr})\text{TiO}_3$ .  $\text{LaTiO}_{3+x}$  is an interesting defect perovskite system, with transport properties varying from insulating to metallic based on oxygen stoichiometry [138,140,165]. La and Ti have a relatively high affinity for oxygen. This suggests that the driving force for native oxide formation at the interface between  $\text{LaTiO}_3$  and either Ni or Cu should be reasonably low. In previous work, we have demonstrated epitaxial growth of  $\text{LaTiO}_3$  on (001) Ni using pulsed laser deposition [166]. The results indicate that epitaxy can be achieved, although the stability of the  $\text{LaTiO}_3/\text{Ni}$  structure is limited to reducing conditions due to the phase transitions that occur with increased oxygen content. With an extreme sensitivity to oxygen content,  $\text{LaTiO}_{3+x}$  is not particularly attractive as a conductive buffer layer. One possible approach to maintaining metallic conductivity in an oxidized state is through cation doping. This could maintain carrier density as well as reduce oxygen diffusivity. The most likely dopant candidate is Sr. Doping with divalent element increases the  $\text{Ti}^{+3} / \text{Ti}^{4+}$  ratio and can make the compound less sensitive to ambient oxygen pressure during YBCO deposition. Electrical conductivity is a function of doping constant  $x$  in the  $\text{La}_{1-x}\text{Sr}_x\text{TiO}_3$  compound, and the resistivity continuously decreases with higher cation doping [140]. Previous study on oxygen dependency showed the room temperature resistivity of  $\text{La}_{0.5}\text{Sr}_{0.5}\text{TiO}_3$  was remained below  $1.0 \times 10^{-3} \Omega\cdot\text{cm}$  in  $10^{-4} \sim 10^{-2}$  Torr of oxygen pressure range [141].

In this chapter, the fundamental properties of  $(\text{La,Sr})\text{TiO}_3$  films on single crystal  $\text{SrTiO}_3$  substrates have been investigated and compared with the  $\text{LaTiO}_3$  films. The HTS films such as  $\text{YBa}_2\text{Cu}_3\text{O}_7$  grown on  $(\text{La,Sr})\text{TiO}_3$  buffer layers on single crystal  $\text{SrTiO}_3$

substrates have been also investigated in order to evaluate the compatibility of thin film layers.

#### 4.2 Experiments

The growth of (La,Sr)TiO<sub>3</sub> and LaTiO<sub>3</sub> films on (001) oriented single crystal SrTiO<sub>3</sub> substrate, 0.2-0.5μm thickness, was performed by pulsed laser deposition (PLD) in vacuum at 750°C, at an energy density of 2 J/cm<sup>2</sup> and repetition rate of 10Hz. A KrF (248nm) excimer laser was used as the ablation source. The oxygen sensitivities of (La,Sr)TiO<sub>3</sub> and LaTiO<sub>3</sub> films have been investigated by changing the oxygen partial pressure from 3.0×10<sup>-5</sup> Torr to 4.0×10<sup>-4</sup> Torr. The high temperature superconducting (HTS) YBa<sub>2</sub>Cu<sub>3</sub>O<sub>7</sub> (YBCO) layer was also grown by PLD under conditions of 1.0×10<sup>-1</sup> Torr of oxygen at 780°C, energy density of 2 J/cm<sup>2</sup>, 10Hz rate, with a thickness of 0.2μm. After completing YBCO deposition, the PLD chamber was cooled down to 500°C at a rate of 28°C/min and the oxygen pressure was increased to 400 Torr. After 20 minutes, the chamber was cooled down to room temperature rapidly.

The x-ray diffraction of  $\theta$ -2 $\theta$  scan,  $\omega$  and  $\phi$ -scan were used in order to observe the thin film crystallinity, in-plane and out-of-plane alignments of each film layers. The in situ reflection high-energy electron diffraction (RHEED) was used to monitor epitaxial film growth. The film thickness was measured by step profilometer which converts the physical step distance into the electrical signals.

A standard four-point probe technique was used to evaluate the electrical properties, including temperature-dependent resistivity (R-T) of not only the buffer layers but also the superconducting film, the superconducting transition temperature ( $T_c$ ) and the critical current density ( $J_c$ ). The R-T measurements were done in the cryogenic cooling

system which was operated in the liquid helium of 4 K. The critical current density ( $J_c$ ) as a function of magnetic field was evaluated by magnetization method in liquid helium. The widths of the samples were in the range of 0.28 ~0.53cm and the distance between the voltage tips was in the range of 0.3~0.4cm.

### 4.3 Results and Discussion

Figure 4-1 shows the x-ray diffraction  $\theta$ - $2\theta$  scan of (La,Sr)TiO<sub>3</sub> film deposited on (001) oriented SrTiO<sub>3</sub> single crystal substrate. The film was grown by pulsed laser deposition (PLD) method at 750°C in vacuum. The y-axis which indicates the intensity of figure 4-1 is designated by log scale in order to separate the film and substrate peaks clearly. The x-ray  $\theta$ - $2\theta$  scan of (La,Sr)TiO<sub>3</sub> film shows (001), (002), (003) peaks at 22.28°, 45.50°, and 70.93° respectively. The cubic lattice constant of the film is 3.98Å calculated from the Bragg's law. Figure 4-2 is the in situ monitored reflection high-energy electron diffraction (RHEED) pattern of (La,Sr)TiO<sub>3</sub> film grown at 750°C in vacuum. According to the x-ray  $\theta$ - $2\theta$  scan and RHEED pattern, the (La,Sr)TiO<sub>3</sub> film is epitaxially deposited on SrTiO<sub>3</sub> single crystal substrate by PLD method at 750°C in vacuum. In order to examine the oxygen sensitivity, the (La,Sr)TiO<sub>3</sub> films were grown in oxygen ambient with partial pressure of  $3.0 \times 10^{-5}$  Torr and  $4.0 \times 10^{-4}$  Torr. Figure 4-3 shows the x-ray diffraction  $\theta$ - $2\theta$  scan of (La,Sr)TiO<sub>3</sub> films deposited on SrTiO<sub>3</sub> single crystal substrates by PLD method with different ambient conditions. Only the (002) peaks of each sample are designated in this figure to make clear comparison. The dashed lines indicate the standard SrTiO<sub>3</sub> (002) and LaTiO<sub>3</sub> (002) peak positions at 46.48°, 46.03° respectively. The films grown under the oxygen partial pressure show the (002) peaks at almost the same position with LaTiO<sub>3</sub> (002) at 46.03°. This indicates that the

oxygen deficiency in the film is compensated by ambient oxygen pressure leading to the stoichiometric  $\text{LaTiO}_3$  film. Figure 4-4 shows the x-ray diffraction  $\theta$ - $2\theta$  scan of  $\text{LaTiO}_3$  film deposited on (001) oriented  $\text{SrTiO}_3$  single crystal substrate. The film was grown by pulsed laser deposition (PLD) method at  $750^\circ\text{C}$  in vacuum. The x-ray  $\theta$ - $2\theta$  scan of  $\text{LaTiO}_3$  film shows (001), (002), (003) peaks at  $22.26^\circ$ ,  $45.47^\circ$ , and  $70.89^\circ$  respectively. The cubic lattice constant of the film is calculated by  $3.98\text{\AA}$ . In order to compare the oxygen sensitivity of  $\text{LaTiO}_3$  with  $(\text{La,Sr})\text{TiO}_3$  film, same oxygen partial pressure conditions such as  $3.0 \times 10^{-5}$  Torr,  $4.0 \times 10^{-4}$  Torr were applied during  $\text{LaTiO}_3$  deposition. In the figure 4-5 (a) and figure 4-6 (a), the x-ray peaks were taken with aligning the sample to the (001) oriented  $\text{SrTiO}_3$  substrate. There are no clear peaks which designate the film existence in both cases. In contrast with  $\text{LaTiO}_3$ ,  $\text{La}_2\text{Ti}_2\text{O}_7$  which is a fully oxidized phase shows monoclinic layered structure. The crystallographic angle between  $(-210)$   $\text{La}_2\text{Ti}_2\text{O}_7$  and (001)  $\text{SrTiO}_3$  is known to be  $4.52^\circ$  [4.13]. The  $\theta$ - $2\theta$  scan graphs in the figure 4-5 (b) and figure 4-6 (b) were taken by tilting the substrate around  $4^\circ$  off axis. According to the figure 4-5 and figure 4-6,  $\text{LaTiO}_3$  films which are growing under the oxygen ambient can be turned into the fully oxidized  $\text{La}_2\text{Ti}_2\text{O}_7$  phase. Figure 4-7 shows the x-ray diffraction  $\phi$ -scan of  $(-420)$  peak for the  $\text{La}_2\text{Ti}_2\text{O}_7$  layer grown under the oxygen pressure of  $3.0 \times 10^{-5}$  Torr. The fourfold symmetry of the peak indicates that the film is in-plane aligned.

In addition to the structure, the transport behavior of epitaxial  $(\text{La,Sr})\text{TiO}_3$  and  $\text{LaTiO}_3$  films grown on  $\text{SrTiO}_3$  is indicated in figure 4-8 as a function of the oxygen pressure during growth. Figure 4-8 (a) designates the resistivities measured at 300 K and figure 4-8 (b) shows the resistivities measured at 77 K. In case of the vacuum growth

condition, both (La,Sr)TiO<sub>3</sub> and LaTiO<sub>3</sub> films show low and nearly identical values, with a resistivity on the order of  $10^{-5}$   $\Omega$  cm at 300 K. As oxygen pressure is moderately increased up to  $4.0 \times 10^{-4}$  Torr, the resistivity of LaTiO<sub>3</sub> film increases by more than two orders of magnitude to  $\sim 0.2$   $\Omega$  cm at 300 K. This increase in the resistivity with oxygen pressure during growth is related to the structural transition from LaTiO<sub>3</sub> to La<sub>2</sub>Ti<sub>2</sub>O<sub>7</sub> phase as indicated in the X-ray diffraction pattern of figure 4-5 and figure 4-6. In contrast, the resistivity of (La,Sr)TiO<sub>3</sub> films is relatively insensitive to oxygen pressure making it attractive as a conductive buffer for coated conductor applications. Figure 4-9 and 4-10 show the resistivity curves of (La,Sr)TiO<sub>3</sub> and LaTiO<sub>3</sub> films on SrTiO<sub>3</sub> substrates under various oxygen pressures as a function of measuring temperature. All of the R-T curves indicate that the films show metallic behaviors.

Based on the fundamental results of (La,Sr)TiO<sub>3</sub> films on single crystal SrTiO<sub>3</sub> substrate, high temperature superconducting YBa<sub>2</sub>Cu<sub>3</sub>O<sub>7</sub> layer was deposited on (La,Sr)TiO<sub>3</sub>. In this case, the (La,Sr)TiO<sub>3</sub> layer played a role of buffer layer similar to the real coated conductor application such as RABiTS. Figure 4-11 is the X-ray diffraction  $\theta$ -2 $\theta$  scan of YBa<sub>2</sub>Cu<sub>3</sub>O<sub>7</sub> film grown on (La,Sr)TiO<sub>3</sub> buffer layer on single crystal SrTiO<sub>3</sub> substrate. The (00 $l$ ) peaks of YBa<sub>2</sub>Cu<sub>3</sub>O<sub>7</sub> film are well defined. Figure 4-12 shows the X-ray diffraction  $\omega$ -scan of (002) peak for (La,Sr)TiO<sub>3</sub> buffer layer grown on SrTiO<sub>3</sub> substrate and (006) peak for YBa<sub>2</sub>Cu<sub>3</sub>O<sub>7</sub> HTS film deposited on (La,Sr)TiO<sub>3</sub> buffer layer. The full width half maximum (FWHM) values of each layer are 0.97° and 1.58°, respectively. Figure 4-13 shows the X-ray diffraction  $\phi$ -scan of (112) peak for (La,Sr)TiO<sub>3</sub> buffer layer grown on SrTiO<sub>3</sub> substrate and (012) peak for YBa<sub>2</sub>Cu<sub>3</sub>O<sub>7</sub> HTS film deposited on (La,Sr)TiO<sub>3</sub> buffer layer. The average full width half maximum

(FWHM) values of the fourfold symmetric peaks for each layer are  $0.71^\circ$  and  $1.48^\circ$ , respectively. According to the  $\omega$ -scan and  $\phi$ -scan, the  $\text{YBa}_2\text{Cu}_3\text{O}_7$  film is in-plane and out-of-plane aligned to the  $(\text{La,Sr})\text{TiO}_3$  buffer layer. Figure 4-14 shows the four-probe resistivity measurement for the  $\text{YBa}_2\text{Cu}_3\text{O}_7 / (\text{La,Sr})\text{TiO}_3 / \text{SrTiO}_3$  structure. The sample has the superconducting transition temperature ( $T_c$ ) of 91 K indicating cation-contamination-free  $\text{YBa}_2\text{Cu}_3\text{O}_7$ . Figure 4-15 is the critical current density ( $J_c$ ) as a function of the magnetic field of  $\text{YBa}_2\text{Cu}_3\text{O}_7 / (\text{La,Sr})\text{TiO}_3 / \text{SrTiO}_3$  structure. The  $J_c$  values were evaluated by magnetization method in liquid helium. The  $J_c$  can be calculated by the equation of  $J_c = (15 \times \Delta M) / r$ , here  $\Delta M$  is the magnetization difference and  $r$  is the radius of the sample. In this graph, the zero-field transport  $J_c$  value is  $2.18 \times 10^6 \text{ A/cm}^2$ . The interesting aspect of the conductive buffer layer in the coated conductor application is whether its conductivity remains after HTS film deposition or not. Normally, the HTS film such as  $\text{YBa}_2\text{Cu}_3\text{O}_7$  is grown at high temperature in high oxygen pressure. The underlying buffer layer should be exposed to this extreme oxidizing condition. The resistivity of  $(\text{La,Sr})\text{TiO}_3$  film after annealing at  $\text{YBa}_2\text{Cu}_3\text{O}_7$  deposition condition (at  $780^\circ\text{C}$ ,  $P_{\text{O}_2} 1.0 \times 10^{-1} \text{ Torr}$ ). Figure 4-16 shows the resistivity curve of  $(\text{La,Sr})\text{TiO}_3$  film grown on  $\text{SrTiO}_3$  substrate after annealing at  $\text{YBa}_2\text{Cu}_3\text{O}_7$  deposition condition. The resistivity values at 300 K and 77 K were about  $1.0 \text{ } \Omega \text{ cm}$  and  $0.09 \text{ } \Omega \text{ cm}$ . The resistivity values of  $(\text{La,Sr})\text{TiO}_3$  film without annealing were  $3.5 \times 10^{-5} \text{ } \Omega \text{ cm}$  and  $1.5 \times 10^{-6} \text{ } \Omega \text{ cm}$  at 300 K and 77 K, respectively. Although the absolute values were increased by roughly  $10^4$  orders of magnitude, the resistivity curve indicates that the  $(\text{La,Sr})\text{TiO}_3$  film remains metallic until the liquid nitrogen temperature of 77 K. The resistivity results of post annealed sample at  $\text{YBa}_2\text{Cu}_3\text{O}_7$  deposition condition show that

the (La,Sr)TiO<sub>3</sub> layer can be a candidate for the conductive buffer layer in the coated conductor applications.

#### 4.4 Conclusions

The perovskite (La,Sr)TiO<sub>3</sub> was investigated as a possible conducting oxide buffer layer for high temperature superconducting coated conductors. In order to observe the oxygen sensitivity, thin (La,Sr)TiO<sub>3</sub> films were epitaxially deposited by PLD on single crystal SrTiO<sub>3</sub> substrates at various oxygen partial pressures and compared with LaTiO<sub>3</sub> films at the same growth conditions. The room temperature resistivity of LaTiO<sub>3</sub> increases rapidly as the oxygen pressure increases by more than two orders of magnitude. In contrast, the resistivity of (La,Sr)TiO<sub>3</sub> films is relatively insensitive to oxygen pressure making it attractive as a conductive buffer for coated conductor applications.

The high temperature superconducting layer such as YBa<sub>2</sub>Cu<sub>3</sub>O<sub>7</sub> was grown epitaxially on (La,Sr)TiO<sub>3</sub> buffer layer on SrTiO<sub>3</sub> substrate with excellent in-plane and out-of-plane alignment. The superconducting transition temperature ( $T_c$ ) of YBa<sub>2</sub>Cu<sub>3</sub>O<sub>7</sub> / (La,Sr)TiO<sub>3</sub> / SrTiO<sub>3</sub> structure was 91 K and the critical current density ( $J_c$ ) of this structure was  $2.18 \times 10^6$  A/cm<sup>2</sup> at 0 magnetic field. The resistivity results of post annealed sample at YBa<sub>2</sub>Cu<sub>3</sub>O<sub>7</sub> deposition condition indicates that the (La,Sr)TiO<sub>3</sub> layer can be a candidate for the conductive buffer layer in the coated conductor applications.



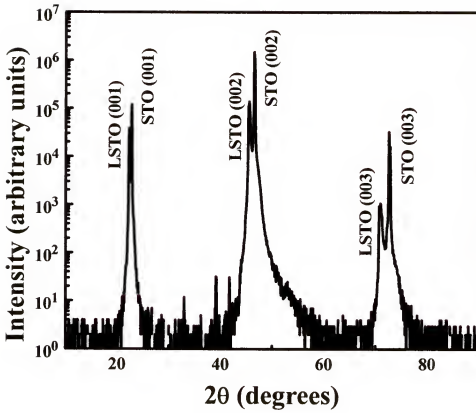


Figure 4-1. The X-ray diffraction  $\theta$ - $2\theta$  scan of  $(\text{La,Sr})\text{TiO}_3$  film grown on  $\text{SrTiO}_3$  single crystal substrate by pulsed laser deposition (PLD) method at  $750^\circ\text{C}$ , in vacuum.



Figure 4-2. The in situ reflection high-energy electron diffraction (RHEED) pattern of  $(\text{La,Sr})\text{TiO}_3$  film deposited on  $\text{SrTiO}_3$  single crystal substrate by PLD method at  $750^\circ\text{C}$ , in vacuum. RHEED is used to monitor the epitaxial film growth.

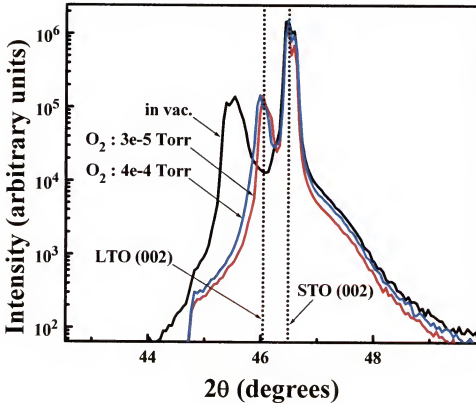


Figure 4-3. The X-ray  $\theta$ - $2\theta$  scans of  $(La,Sr)TiO_3$  films deposited on  $SrTiO_3$  single crystal substrates in different ambient conditions.

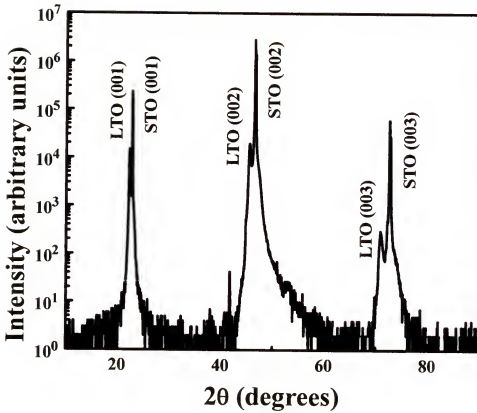


Figure 4-4. The X-ray diffraction  $\theta$ - $2\theta$  scan of  $\text{LaTiO}_3$  film grown on  $\text{SrTiO}_3$  single crystal substrate by pulsed laser deposition (PLD) method at  $750^\circ\text{C}$ , in vacuum.

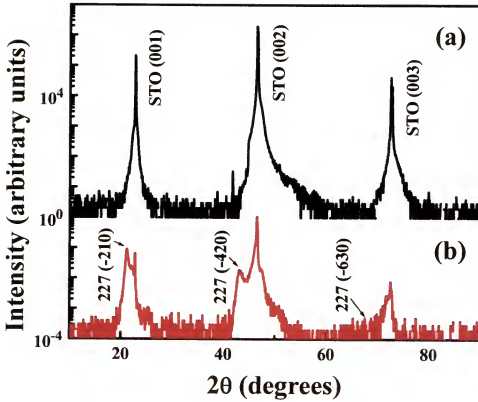


Figure 4-5. The two different X-ray  $\theta$ - $2\theta$  scans of  $\text{LaTiO}_3$  film grown on  $\text{SrTiO}_3$  single crystal substrate in the oxygen pressure of  $3.0 \times 10^{-5}$  Torr, aligned to (a) the substrate (001) plane and (b) the  $\text{La}_2\text{Ti}_2\text{O}_7$  (-210) plane, respectively.

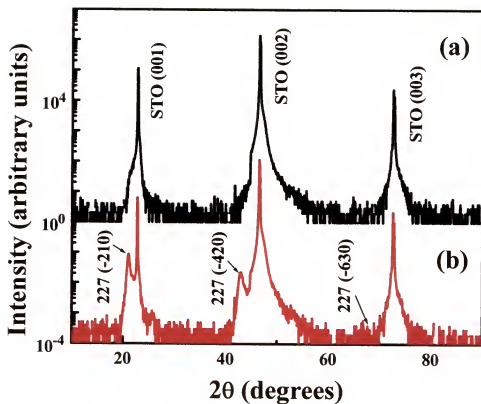


Figure 4-6. The two different X-ray  $\theta$ - $2\theta$  scans of  $\text{LaTiO}_3$  film grown on  $\text{SrTiO}_3$  single crystal substrate in the oxygen pressure of  $4.0 \times 10^{-4}$  Torr, aligned to (a) the substrate (001) plane and (b) the  $\text{La}_2\text{Ti}_2\text{O}_7$  (-210) plane, respectively.

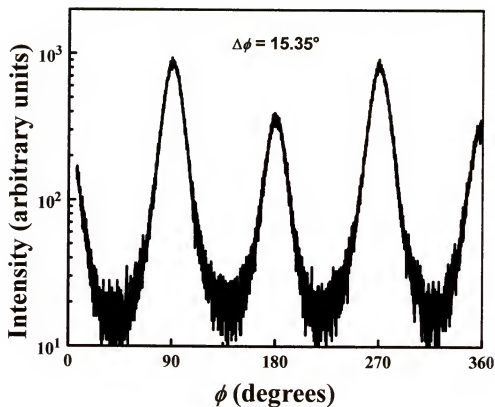


Figure 4-7. The X-ray  $\phi$ -scan of  $(-420)$  peak for  $\text{La}_2\text{Ti}_2\text{O}_7$  layer grown on  $\text{SrTiO}_3$  single crystal substrate in the oxygen pressure of  $3.0 \times 10^{-5}$  Torr.

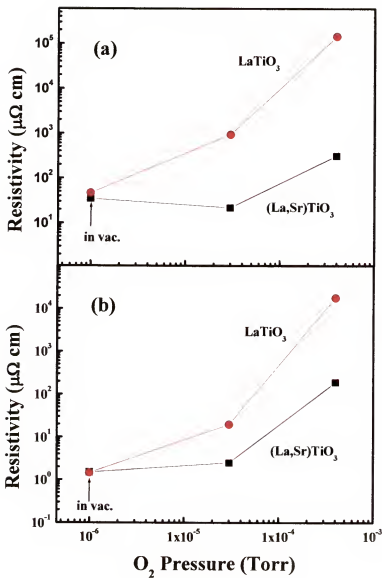


Figure 4-8. The resistivities of  $(\text{La,Sr})\text{TiO}_3$  and  $\text{LaTiO}_3$  films on single crystal  $\text{SrTiO}_3$ , measured at (a) 300 K and (b) 77 K, as a function of the oxygen pressure.



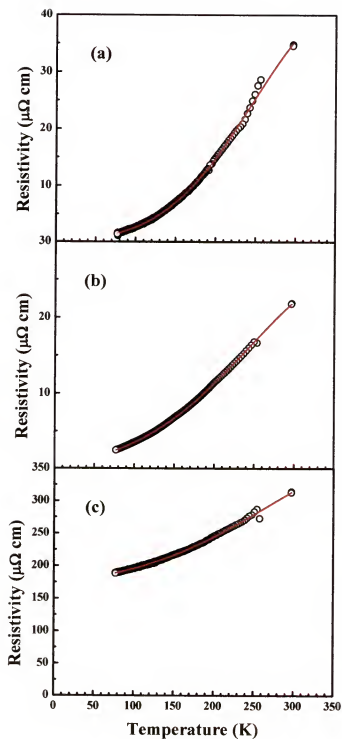


Figure 4-9. The resistivity curves of  $(\text{La,Sr})\text{TiO}_3$  films on  $\text{SrTiO}_3$  substrates grown in (a) vacuum, (b)  $3.0 \times 10^{-5}$  Torr of oxygen, and (c)  $4.0 \times 10^{-4}$  Torr of oxygen, as a function of temperature.

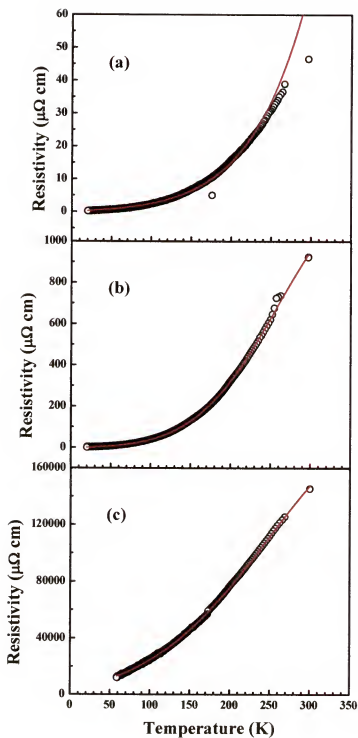


Figure 4-10. The resistivity curves of LaTiO<sub>3</sub> films on SrTiO<sub>3</sub> substrates grown in (a) vacuum, (b)  $3.0 \times 10^{-5}$  Torr of oxygen, and (c)  $4.0 \times 10^{-4}$  Torr of oxygen, as a function of temperature.

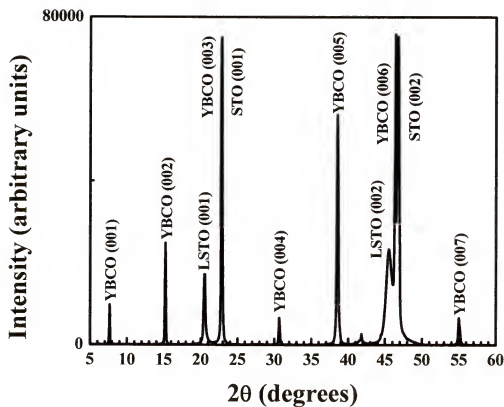


Figure 4-11. The X-ray  $\theta$ - $2\theta$  scan of  $\text{YBa}_2\text{Cu}_3\text{O}_7$  deposited on  $(\text{La,Sr})\text{TiO}_3$  buffer layer on  $\text{SrTiO}_3$  single crystal substrate.

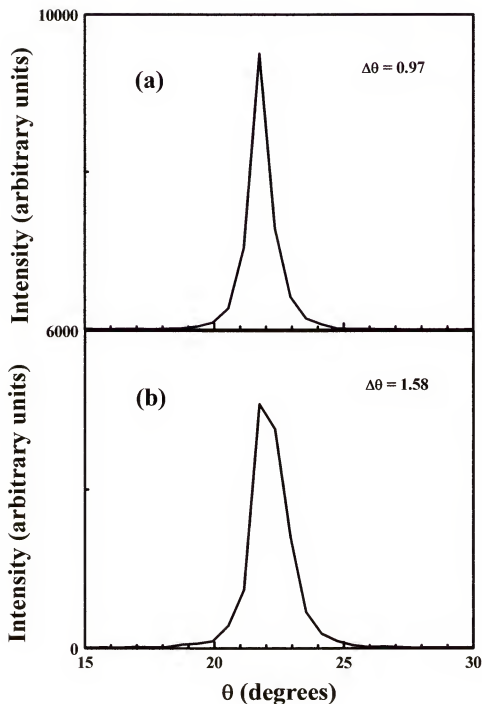


Figure 4-12. The X-ray  $\omega$ -scan of (a) (002) peak for (La,Sr)TiO<sub>3</sub> buffer layer on SrTiO<sub>3</sub> single crystal substrate and (b) (006) peak for the YBa<sub>2</sub>Cu<sub>3</sub>O<sub>7</sub> film deposited on (La,Sr)TiO<sub>3</sub> buffer layer.

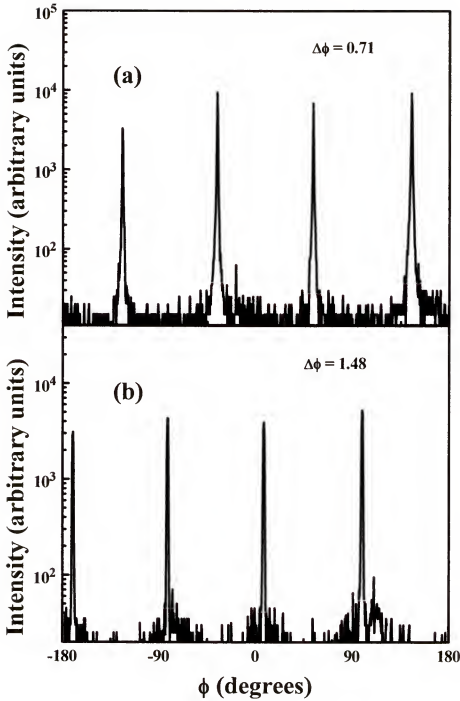


Figure 4-13. The X-ray  $\phi$ -scan of (a) (112) peak for  $(\text{La,Sr})\text{TiO}_3$  buffer layer on  $\text{SrTiO}_3$  single crystal substrate and (b) (012) peak for the  $\text{YBa}_2\text{Cu}_3\text{O}_7$  film deposited on  $(\text{La,Sr})\text{TiO}_3$  buffer layer.

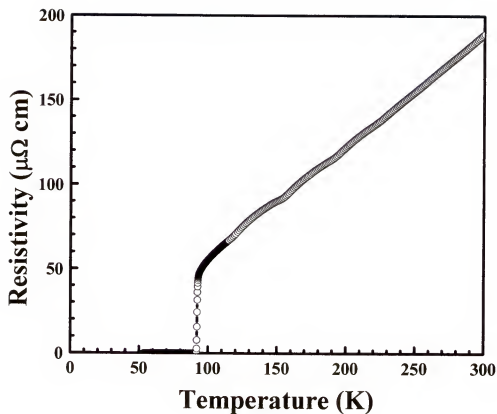


Figure 4-14. The resistivity versus temperature measurement for  $\text{YBa}_2\text{Cu}_3\text{O}_7$  film deposited on  $(\text{La,Sr})\text{TiO}_3$  buffer layer on single crystal  $\text{SrTiO}_3$  substrate.

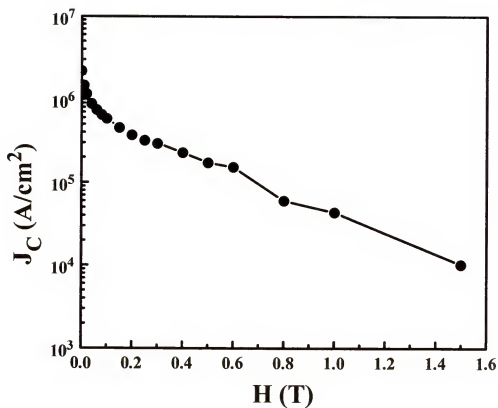


Figure 4-15. The critical current density ( $J_c$ ) as a function of magnetic field of  $\text{YBa}_2\text{Cu}_3\text{O}_7$  film deposited on (La,Sr) $\text{TiO}_3$  buffer layer on single crystal  $\text{SrTiO}_3$  substrate.

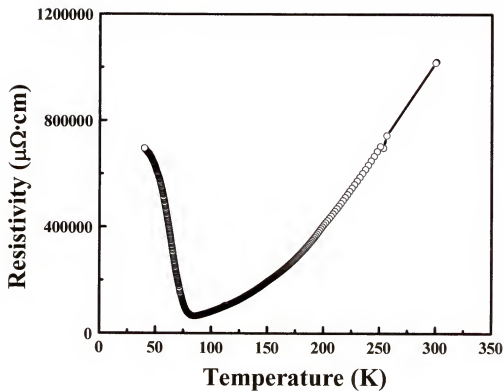


Figure 4-16. The resistivity versus temperature graph of  $(\text{La,Sr})\text{TiO}_3$  film grown on single crystal  $\text{SrTiO}_3$  substrate after annealing with the  $\text{YBa}_2\text{Cu}_3\text{O}_7$  deposition condition.



CHAPTER 5  
EPITAXIAL (La,Sr)TiO<sub>3</sub> AS A CONDUCTIVE BUFFER FOR NI-W BASED HIGH  
TEMPERATURE SUPERCONDUCTING COATED CONDUCTORS

**5.1 Introduction**

LaTiO<sub>3+x</sub> is a quite attractive material for coated conductor application because it has good metallic property at all temperature range in the oxygen stoichiometric of  $0.1 < x < 0.25$  [137], and its pseudo-cubic lattice parameter is well matched with YBa<sub>2</sub>Cu<sub>3</sub>O<sub>7</sub>. However, the composition also can be changed during YBa<sub>2</sub>Cu<sub>3</sub>O<sub>7</sub> growth in the high oxygen ambient ( $\sim 1 \times 10^{-1}$  Torr) at high temperature ( $\sim 780^\circ\text{C}$ ). The previous research on the relation of resistivity of LaTiO<sub>3+x</sub> with oxygen pressure during deposition by PLD indicated that oxygen played a crucial role in conducting property [139]. Cation doping in the compound can overcome this oxygen sensitivity of LaTiO<sub>3+x</sub>. Doping with divalent element increases the  $\text{Ti}^{+3} / \text{Ti}^{+4}$  ratio and can make the compound less sensitive to ambient oxygen pressure during YBCO deposition. Electrical conductivity is a function of doping constant x in the La<sub>1-x</sub>Sr<sub>x</sub>TiO<sub>3</sub> compound, and the resistivity continuously decreases with higher cation doping [140]. Previous study on oxygen dependency showed the room temperature resistivity of La<sub>0.5</sub>Sr<sub>0.5</sub>TiO<sub>3</sub> was remained below  $1.0 \times 10^{-3} \Omega \cdot \text{cm}$  in  $10^{-4} \sim 10^{-2}$  Torr of oxygen pressure range [141]. The metallic (La,Sr)TiO<sub>3</sub> film is being considered for various electronic applications [168-170], including coated onductors based on epitaxial high temperature superconducting (HTS) films deposited on metal tapes. In functioning as a conducting buffer layer in a RABiTS structure, the conductive oxide layer architecture must satisfy a specific set of criteria. First, the buffer layer must

be reasonably well lattice matched to both the metal substrate and the superconducting film, thus enabling epitaxy. Second, the material must be conductive not only as deposited, but after subsequent HTS film growth and oxygen annealing. Third, the interaction between the buffer layer and the metal substrate must be such as to minimize formation of any native interfacial oxide that would serve as an insulating barrier to shunted current flow. (La,Sr)TiO<sub>3</sub> appears to in satisfy these criteria. At room temperature, LaTiO<sub>3</sub> possesses the orthorhombic GdFeO<sub>3</sub> perovskite structure with  $a = 5.604 \text{ \AA}$ ,  $b = 5.595 \text{ \AA}$ , and  $c = 7.906 \text{ \AA}$ . The pseudo-cubic lattice parameter of  $3.96 \text{ \AA}$  provides a relatively large (12%) lattice mismatch to Ni ( $a = 3.524 \text{ \AA}$ ), although similar mismatched parameters have proven useful in other RABiTS architectures. La, Sr, and Ti have a high affinity for oxygen relative to Ni, suggesting that native NiO formation at the interface should be minimal.

In order to grow conductive (La,Sr)TiO<sub>3</sub> layer on Ni-W based metal tape, TiN was selected as a seed layer for templating the epitaxial film growth. Recent research has suggested that considerable sharpening of the out-of-plane texture occurs in YBa<sub>2</sub>Cu<sub>3</sub>O<sub>7- $\delta$</sub>  films grown on oxide buffer layers due to a tilted epitaxy growth mechanism in the TiN seed [167]. The buffer scheme using transition metal nitride film was reported by Kim *et al.* in 2002 [69]. In this report, TiN was chosen because of low electrical resistivity (20–30  $\mu\Omega\cdot\text{cm}$ ) and good mechanical strength (Young's modulus : 600 GPa, micro-hardness : 2000 Kg/mm<sup>2</sup>). Due to the oxidation of TiN layer during YBCO deposition, CeO<sub>2</sub> layer also applied between YBCO and TiN films. The TiN layer was formed by DC reactive sputtering with Ar/N<sub>2</sub> mixture gas and the CeO<sub>2</sub>, YBCO layers were grown by PLD method. A superconducting transition temperature for this architecture was 89 K

and the critical current density was  $6 \times 10^5 \text{ A/cm}^2$  at 77 K. Because TiN is also known as Cu diffusion barrier [70], Cantoni *et al.* studied multi buffer scheme using TiN for Cu based RABiTS process [71]. In this report,  $\text{LaMnO}_3 / \text{MgO} / \text{TiN}$  buffer architecture was proposed. MgO layer was chosen for oxygen diffusion barrier, and  $\text{LaMnO}_3$  layer proved to be a planarizing material for smooth growing of YBCO.

## 5.2 Experiments

The Ni-3% W alloy tapes were used as a metal substrate. The Ni-W tapes have  $\{100\} \langle 100 \rangle$  cube texture and obtained from randomly oriented metal bars by cold-rolling, followed by an anneal in vacuum at  $800^\circ\text{C}$  for 1 hour. The growth of  $(\text{La,Sr})\text{TiO}_3$  films was performed by pulsed laser deposition (PLD) in vacuum at  $750^\circ\text{C}$ , at an energy of  $2 \text{ J/cm}^2$  and repetition rate of 5~10Hz with a thickness of  $0.6 \mu\text{m}$ . A KrF (248nm) excimer laser was used as the ablation source. For the Ni-W based RABiTS application, PLD TiN layer was selected as a  $(\text{La,Sr})\text{TiO}_3$  template. The deposition condition for TiN was in  $1.0 \times 10^{-4}$  Torr of nitrogen at  $650^\circ\text{C}$ , energy density of  $3.5 \text{ J/cm}^2$ , rate 10Hz, with a thickness range of  $0.05 \sim 0.5 \mu\text{m}$ .  $\text{YBa}_2\text{Cu}_3\text{O}_{7-\delta}$  layer was grown as a high temperature superconductor by PLD under conditions of  $1.0 \times 10^{-1}$  Torr of oxygen at  $780^\circ\text{C}$ , energy density of  $2 \text{ J/cm}^2$ , 10Hz rate, with a thickness of  $0.2 \mu\text{m}$ . After completing YBCO deposition, the PLD chamber was cooled down to  $500^\circ\text{C}$  at a rate of  $28^\circ\text{C/min}$  and the oxygen pressure was increased to 400 Torr. After 20 minutes, the chamber was cooled down to room temperature rapidly.

The x-ray diffraction of  $\theta$ - $2\theta$  scan,  $\omega$  and  $\phi$ -scan were used in order to observe the in-plane and out-of-plane alignments of each layers. The in situ reflection high-energy electron diffraction (RHEED) was used to monitor epitaxial film growth. The surface

observation and the compositional analysis of thin films were investigated by scanning electron microscope (SEM) and energy dispersive x-ray spectroscopy (EDS).

A standard four probe technique was used to evaluate the electrical properties, including superconducting transition temperature ( $T_c$ ) and the critical current density ( $J_c$ ). The  $J_c$  measurements were carried out in liquid nitrogen, defined at a 1  $\mu\text{V}/\text{cm}$  criterion. The widths of the samples were in the range of 0.40 ~ 0.50 cm and the distance between the voltage tips was in the range of 0.3 ~ 0.4 cm.

### 5.3 Results and Discussion

The X-ray diffraction  $\theta$ - $2\theta$  scan shown in Figure 5-1 is for (La,Sr)TiO<sub>3</sub> films grown directly on Ni-3% W alloy tape. Although the Ni-W tape has {100}<100> cube texture, (La,Sr)TiO<sub>3</sub> layers grown at the temperature range of 700°C ~ 800°C showed strong (111) peaks. In order to grow (La,Sr)TiO<sub>3</sub> layer epitaxially on Ni-W tape without (111) peaks, the transition metal nitride such as TiN was selected for a epitaxial seed layer. The proper thickness of TiN layer should be considered because the metal elements can be diffused through TiN layer and reach the sample surface. The metal atoms diffused out from the metal substrate can lower the transition temperature of YBa<sub>2</sub>Cu<sub>3</sub>O<sub>7</sub>. In order to adjust the appropriate thickness, the TiN films with the thickness range of 500Å ~ 5000Å were deposited on 10000Å thick Cu films which were grown on single crystal SrTiO<sub>3</sub> substrates and the samples were annealed at 740°C in vacuum for 30 minutes and 60 minute. Figure 5-2 shows the energy dispersive X-ray spectroscopy (EDS) of the samples with different thicknesses after annealing for 60 minutes. The EDS signals were captured from the surfaces of TiN films. According to figure 5-2, titanium (Ti) and nitrogen (N) peaks were very weak in the sample of 500Å thick TiN layer and gradually increased as

the TiN layer were getting thicker. This indicates that the level of metal diffusion from the substrate can be affected by the TiN layer thickness. Figure 5-3 is the atomic percent of Cu observed on the surface of the TiN layer. The Cu composition level decreases drastically as the TiN thickness increases. The sample of 500Å thick TiN layer showed clear difference of Cu composition before and after annealing. From the annealing test, the proper TiN thickness was thought to be around 2000Å because thicker film has higher tensile stress which generates the handling problem. Figure 5-4 is the X-ray diffraction  $\theta$ -2 $\theta$  scans of TiN layer deposited on Ni-W tape and (La,Sr)TiO<sub>3</sub> film grown on TiN seed layer by PLD. The (La,Sr)TiO<sub>3</sub> (112) peaks observed in the sample which was grown directly on the Ni-W tape vanished and (00 $l$ ) peaks were clearly defined. Figure 5-5 shows the in situ monitored reflection high-energy electron diffraction (RHEED) patterns of TiN layer and (La,Sr)TiO<sub>3</sub> film grown on TiN seed layer. According to the x-ray  $\theta$ -2 $\theta$  scan and RHEED pattern, the TiN film is epitaxially deposited on textured Ni-W alloy tape. In addition to that, the (La,Sr)TiO<sub>3</sub> buffer layer also formed epitaxially on the TiN seed layer.

From the X-ray diffraction  $\omega$ -scans shown in figure 5-6, rocking curve sharpening was observed. The full width half maximum (FWHM) value of (002) TiN showed 3.4° compared to (002) Ni-W tape of 8.7°. FWHM value for the TiN film is considerably smaller than the corresponding value for the Ni-W substrate. FWHM of (004) (La,Sr)TiO<sub>3</sub> grown on TiN layer showed 3.8°. The in-plane aligned textures of the films are shown in the X-ray  $\phi$ -scans through the Ni (111), TiN (111) and (La,Sr)TiO<sub>3</sub> (112). The large peaks every 90 degrees in figure 5-7 represent the majority in-plane aligned (La,Sr)TiO<sub>3</sub> and TiN grains. The FWHM values of the  $\phi$ -scan are 7.28°, 6.48°, 8.89° for

Ni (111), TiN (111), and (La,Sr)TiO<sub>3</sub> (112), respectively. Figure 5-7 indicates that a cube-on-cube epitaxial relationship was obtained among the Ni-W substrate, TiN and (La,Sr)TiO<sub>3</sub> films. According to the x-ray diffraction  $\theta$ -2 $\theta$  scan,  $\omega$ -scan,  $\phi$ -scan and RHEED study, in-plane and out-of-plane aligned epitaxial thin film of (La,Sr)TiO<sub>3</sub> was grown on Ni-W metal tape by using TiN as a seed layer.

In order to assess the compatibility of (La,Sr)TiO<sub>3</sub> as a buffer layer for RABiTS application, the growth of YBa<sub>2</sub>Cu<sub>3</sub>O<sub>7- $\delta$</sub>  thin film on (La,Sr)TiO<sub>3</sub> / TiN / Ni-W tape structure was investigated. The X-ray diffraction  $\theta$ -2 $\theta$  scan in figure 5-8 shows clear YBa<sub>2</sub>Cu<sub>3</sub>O<sub>7- $\delta$</sub>  peaks. Although the YBa<sub>2</sub>Cu<sub>3</sub>O<sub>7- $\delta$</sub>  thin film was grown under conditions of  $1.0 \times 10^{-1}$  Torr of oxygen at 780°C, neither Ni oxide nor Ti oxide peaks detected in the scan. Figure 5-9 is the x-ray diffraction  $\omega$ -scan of (005) YBa<sub>2</sub>Cu<sub>3</sub>O<sub>7- $\delta$</sub>  and figure 5-10 is the  $\phi$ -scan of (103) YBa<sub>2</sub>Cu<sub>3</sub>O<sub>7- $\delta$</sub>  on (La,Sr)TiO<sub>3</sub> buffer layer / TiN seed layer / Ni-W tape structure. The rocking curve FWHM value of the (005) YBa<sub>2</sub>Cu<sub>3</sub>O<sub>7- $\delta$</sub>  peak is 4.92° and  $\phi$ -scan FWHM value of (103) YBa<sub>2</sub>Cu<sub>3</sub>O<sub>7- $\delta$</sub>  peak is 10.1°. Both x-ray diffraction results suggest that the in-plane and out-of-plane aligned high temperature superconducting YBa<sub>2</sub>Cu<sub>3</sub>O<sub>7- $\delta$</sub>  film can be formed epitaxially on the (La,Sr)TiO<sub>3</sub> / TiN / Ni-W tape structure.

A standard four-probe technique was used to evaluate the electrical properties, including superconducting transition temperature ( $T_c$ ) and critical current density ( $J_c$ ). The  $J_c$  value was assigned at a 1  $\mu$ V/cm criterion. Figure 5-11 shows the temperature-dependent net resistivity of the YBa<sub>2</sub>Cu<sub>3</sub>O<sub>7- $\delta$</sub>  on (La,Sr)TiO<sub>3</sub> / TiN / Ni-W tape. The sample has a  $T_c$  value of 89 K which is lower than the standard YBa<sub>2</sub>Cu<sub>3</sub>O<sub>7- $\delta$</sub>  film. Figure 5-12 is the I-V curve obtained from the YBa<sub>2</sub>Cu<sub>3</sub>O<sub>7- $\delta$</sub>  on (La,Sr)TiO<sub>3</sub> / TiN / Ni-W tape in

a field of 0 T and at the temperature of 77 K. The zero-field transport  $J_c$  is  $0.42 \times 10^6$  A/cm<sup>2</sup>. Figure 5-13 is the SEM picture of YBa<sub>2</sub>Cu<sub>3</sub>O<sub>7- $\delta$</sub>  film surface grown on (La,Sr)TiO<sub>3</sub> / TiN / Ni-W tape which shows YBa<sub>2</sub>Cu<sub>3</sub>O<sub>7- $\delta$</sub>  2<sup>nd</sup> phases and pin holes. These could cause the lower  $T_c$  and  $J_c$  values and deviation of resistivity versus temperature curve from the ideal behavior. Figure 5-14 is the EDS analysis graph indicating that the YBa<sub>2</sub>Cu<sub>3</sub>O<sub>7- $\delta$</sub>  film does not possess any cation contamination.

#### 5.4 Conclusions

The epitaxial film growth of (La,Sr)TiO<sub>3</sub> was examined on Ni-W metal alloy tape. The transition metal nitride such as TiN was deposited epitaxially on Ni-W tape by PLD and played an excellent role as a seed layer for (La,Sr)TiO<sub>3</sub> film growth on Ni-W tape.

The high temperature superconducting YBa<sub>2</sub>Cu<sub>3</sub>O<sub>7</sub> film was deposited epitaxially on (La,Sr)TiO<sub>3</sub> buffer layer with the TiN seed layer on Ni-W tape. The YBa<sub>2</sub>Cu<sub>3</sub>O<sub>7</sub> film grown on (La,Sr)TiO<sub>3</sub> / TiN / Ni-W tape has superconducting transition temperature of 89 K and critical current value of  $0.42 \times 10^6$  A/cm<sup>2</sup>. This shows that (La,Sr)TiO<sub>3</sub> is a possible candidate for the conductive buffer layer in the coated conductor applications.

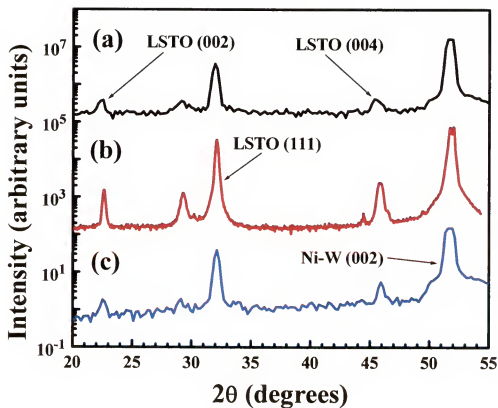


Figure 5-1. The X-ray diffraction  $\theta$ - $2\theta$  scan of  $(\text{La,Sr})\text{TiO}_3$  films deposited directly on Ni-W tape by PLD at the temperature of (a) 700°C, (b) 750°C, and (c) 800°C.



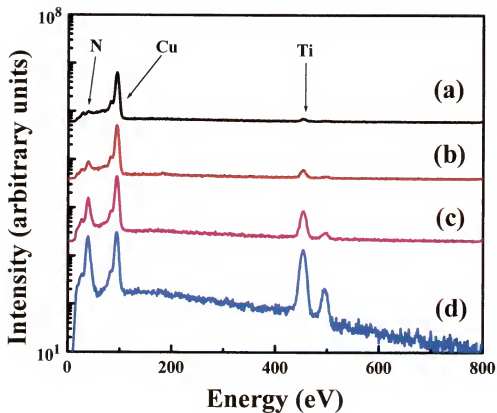


Figure 5-2. The energy dispersive X-ray spectroscopy (EDS) results of TiN films grown on Cu layers on single crystal  $\text{SrTiO}_3$  substrates with the thicknesses of (a) 500Å, (b) 1000Å, (c) 2000Å, and (d) 5000Å. These curves were taken after annealing the samples at 740°C, in vacuum for 60 minutes.

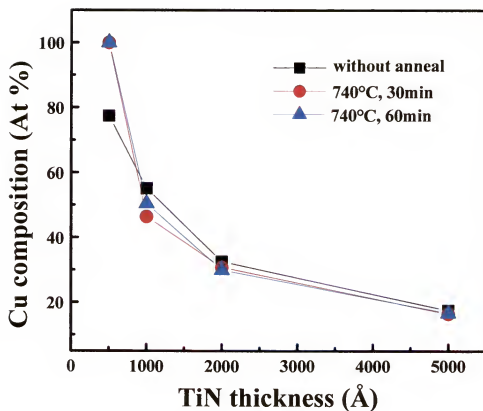


Figure 5-3. The atomic percent of Cu observed on the surface of TiN layer with the thickness range of 500~5000Å. The square symbols designate the samples without annealing. The circles and triangles show the samples with annealing at 740°C, in vacuum for 30 minutes and 60 minutes, respectively.

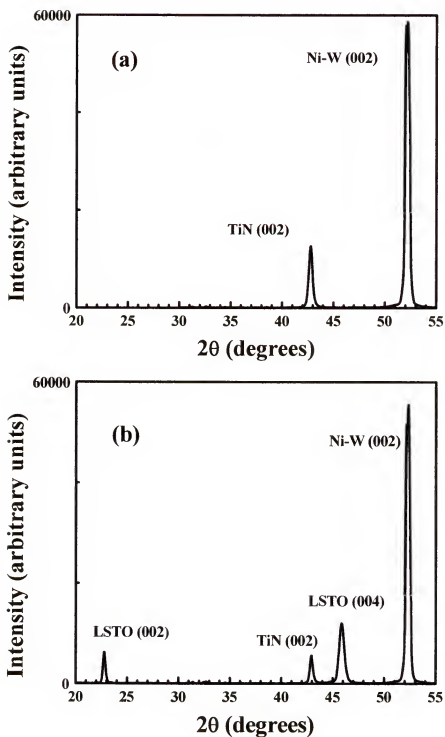


Figure 5-4. The X-ray diffraction  $\theta$ - $2\theta$  scan of (a) TiN layer deposited on textured Ni-W alloy tape, and (b) (La,Sr)TiO<sub>3</sub> film deposited on TiN seed layer.

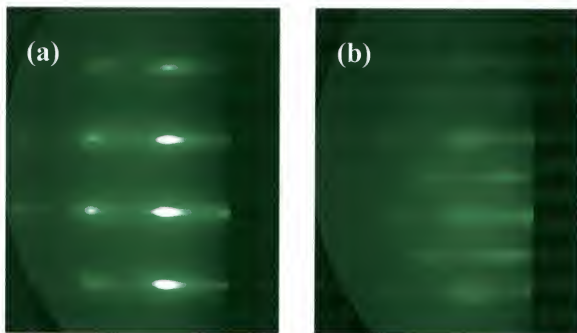


Figure 5-5. The in situ reflection high-energy electron diffraction (RHEED) pattern of (a) TiN film deposited on textured Ni-W alloy tape, and (b) (La,Sr)TiO<sub>3</sub> film deposited on TiN seed layer.

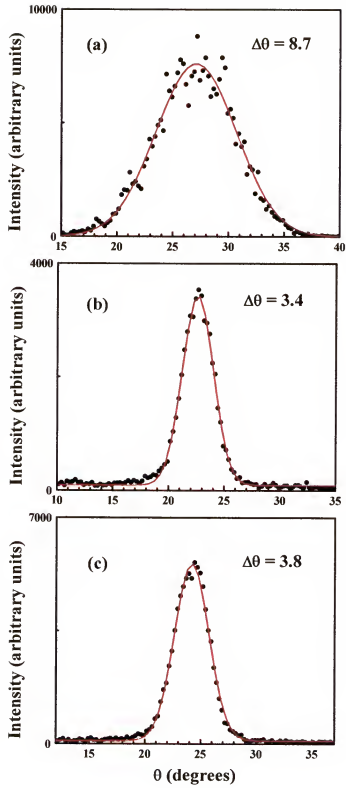


Figure 5-6. The X-ray diffraction  $\omega$ -scan of (a) Ni-W (002), (b) TiN (002), and (c) (La,Sr)TiO<sub>3</sub> (004) planes.

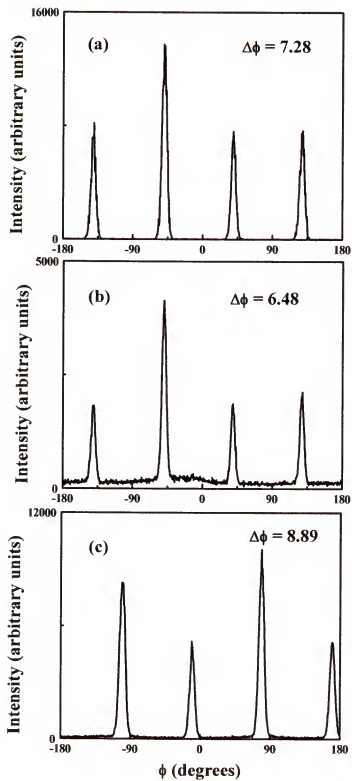


Figure 5-7. The X-ray diffraction  $\phi$ -scan of (a) Ni-W (111), (b) TiN (111), and (c) (La,Sr)TiO<sub>3</sub> (112) planes.

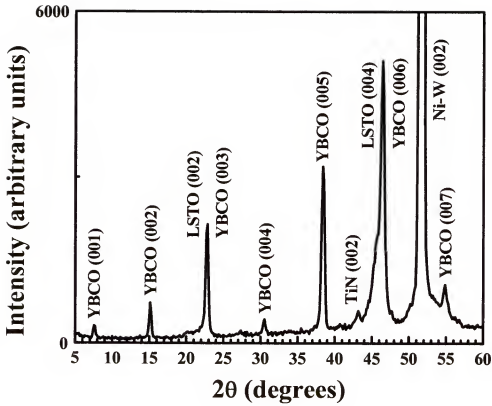


Figure 5-8. The X-ray diffraction  $\theta$ - $2\theta$  scan of high temperature superconducting  $\text{YBa}_2\text{Cu}_3\text{O}_7$  film grown on  $(\text{La,Sr})\text{TiO}_3$  buffer layer / TiN seed layer / Ni-W tape.

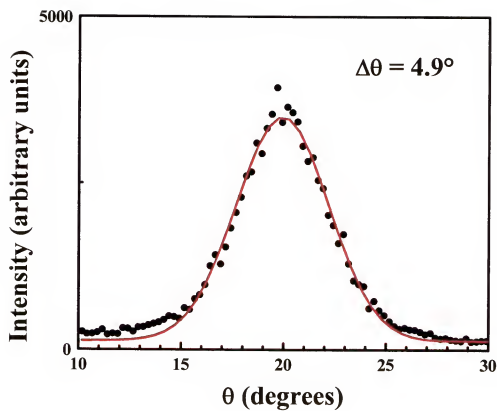


Figure 5-9. The X-ray diffraction  $\omega$ -scan of (005)  $\text{YBa}_2\text{Cu}_3\text{O}_7$  which was grown on (La,Sr) $\text{TiO}_3$  buffer layer / TiN seed layer / Ni-W tape.



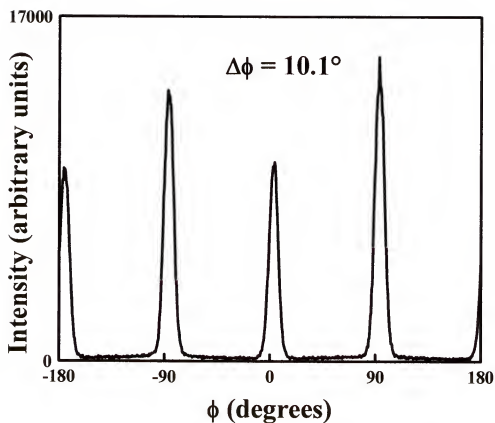


Figure 5-10. The X-ray diffraction  $\phi$ -scan of (103)  $\text{YBa}_2\text{Cu}_3\text{O}_7$  which was grown on (La,Sr) $\text{TiO}_3$  buffer layer / TiN seed layer / Ni-W tape.

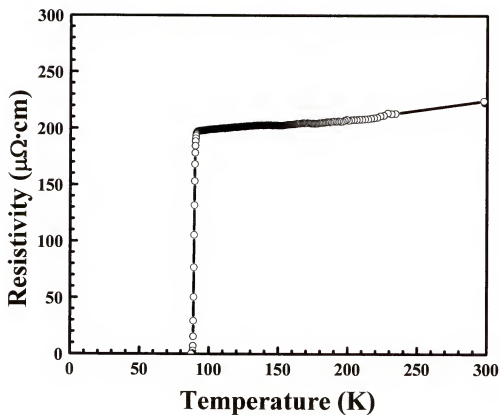


Figure 5-11. The resistivity versus temperature graph for  $\text{YBa}_2\text{Cu}_3\text{O}_7$  film grown on  $(\text{La,Sr})\text{TiO}_3$  buffer layer / TiN seed layer / Ni-W tape.

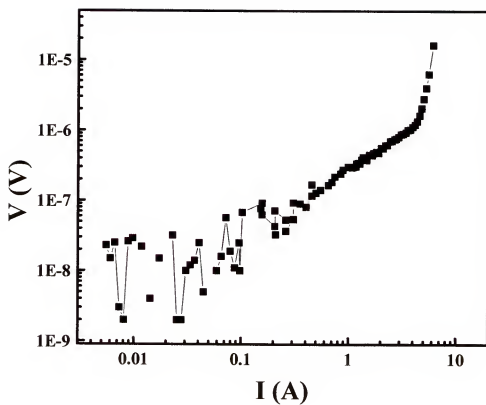


Figure 5-12. The voltage versus current graph of  $\text{YBa}_2\text{Cu}_3\text{O}_7$  film deposited on (La,Sr) $\text{TiO}_3$  buffer layer / TiN seed layer / Ni-W tape.

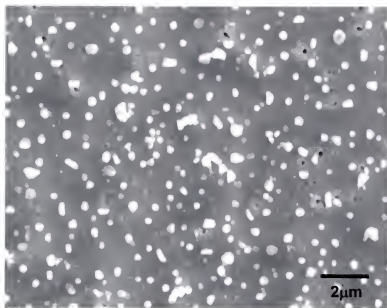


Figure 5-13. The SEM picture of YBa<sub>2</sub>Cu<sub>3</sub>O<sub>7</sub> film surface deposited on (La,Sr)TiO<sub>3</sub> buffer layer / TiN seed layer / Ni-W tape.

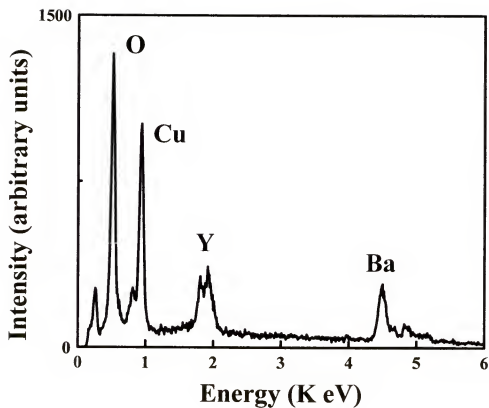


Figure 5-14. The energy dispersive X-ray spectroscopy (EDS) results of  $\text{YBa}_2\text{Cu}_3\text{O}_7$  film grown on  $(\text{La,Sr})\text{TiO}_3$  / TiN / Ni-W tape.

CHAPTER 6  
EPITAXIAL (LA,SR)TiO<sub>3</sub> AS A CONDUCTIVE BUFFER FOR CU BASED HIGH  
TEMPERATURE SUPERCONDUCTING COATED CONDUCTORS

**6.1 Introduction**

The important factor that can influence the current density,  $J_c$  in the superconducting wire application is the crystallinity of the HTS material. The high-angle grain boundaries generated in the polycrystalline HTS can reduce the amount of current because the grain boundary can act as weak superconducting interface separating the superconductivity. This is known as weak links and the grain boundary effect was demonstrated by Chaudhari *et al.* [34]. The YBa<sub>2</sub>Cu<sub>3</sub>O<sub>7</sub> film grown on textured metal templates can drastically reduce the misorientation of the individual grains allowing improvement of the links in the current path. The metal tapes produced by the thermomechanical texturing is known as rolling assisted biaxially textured substrate (RABiTS). The BABiTS process also consists of depositing buffer layers and HTS materials on the biaxially textured flexible metal substrates.

Nickel which is the current starting template of 2G wires has ferromagnetic (FM) property and the magnetic metal substrate such as Ni can cause significant hysteretic losses during application of alternating current (ac). The ac loss can be decreased by adding W to Ni [78]. However, even the Ni-W (5 at.%) alloy tape is not perfect nonmagnetic. In this aspect, Cu substrate is another candidate for the starting template of 2G wires. Cu is a diamagnetic material which shows no ac loss phenomenon. Cu also surpasses Ni alloy in the electrical conductivity characteristics. At 300 K, the resistivity

of Cu tape is  $1.5 \times 10^{-6} \Omega \cdot \text{cm}$  which is lower than Ni-W (3 at.%) alloy tape of  $2.5 \times 10^{-5} \Omega \cdot \text{cm}$ . At the temperature of liquid nitrogen 77 K, Cu tape and Ni-W (3 at.%) tape show the resistivity value of  $2.0 \times 10^{-7} \Omega \cdot \text{cm}$  and  $1.7 \times 10^{-5} \Omega \cdot \text{cm}$  respectively. Cu tape has  $\{100\} \langle 100 \rangle$  cube texture and obtained from randomly oriented metal bars by cold-rolling, followed by an anneal in vacuum at  $800^\circ\text{C}$  for 1 h.

Though the Cu based RABiTS process has advantages, the Cu oxidation problem could be worse. The high temperature and high oxygen ambient of  $\text{YBa}_2\text{Cu}_3\text{O}_7$  growth condition can cause copper oxidation. One method of preventing Cu oxidation is applying noble metal as an oxygen barrier between metal substrate and conductive oxide buffer layers. One of the candidate material is iridium (Ir) which has face centered cubic (fcc) crystal structure and lattice parameter of  $3.840 \text{ \AA}$ . In the crystallographic aspect, iridium can be well matched with Cu substrate. Because iridium is well known platinum group metal with excellent oxidation resistance, oxidation behavior is only considered above  $1400^\circ\text{C}$  [95~97]. Although the iridium oxides ( $\text{IrO}_2$ ) are formed after the YBCO deposition, it has still good metallic property with the resistivity of below  $3 \times 10^{-4} \Omega \cdot \text{cm}$  at room temperature [98]. Aytug *et al.* reported Ir as an oxygen barrier on Ni-W alloy based RABiTS application [99]. In their research,  $\text{La}_{0.7}\text{Sr}_{0.3}\text{MnO}_3$  conductive buffer layer was used to form fully conductive buffer architecture. On the other hand, careful consideration is also needed, because oxygen diffusivity through Ir is  $5 \times 10^{-12} \text{ cm}^2/\text{s}$  at  $800^\circ\text{C}$  [78] and there is a possibility of Cu diffusion through Ir layer. Cu and Ir are known to be soluble in the extremely small amount of atomic % [100]. However,  $50 \mu\text{m}$  thick Cu substrate can continuously supply copper element to the thin Ir layer during buffer oxides and YBCO processes. These mean that Cu oxidation can be observed either

on top of the YBCO film or on the Cu substrate and proper thickness of Ir layer should be deposited.

In this chapter, novel buffer scheme for high temperature superconducting coated conductors will be addressed. Multi layer of (La,Sr)TiO<sub>3</sub> and Ir will be formed on Cu tape. The metallic (La,Sr)TiO<sub>3</sub> serves as a template for YBa<sub>2</sub>Cu<sub>3</sub>O<sub>7</sub> film growth and Ir layer acts as an oxygen diffusion barrier between the metal substrate and the buffer layer. The (La,Sr)TiO<sub>3</sub> and Ir stack will be the fully conductive buffer scheme on Cu based RABiTS application.

## 6.2 Experiments

The copper tapes were used as a metal substrate. The Cu tapes have {100}<100> cube texture and obtained from randomly oriented metal bars by cold-rolling, followed by an anneal in vacuum at 800°C for 1 hour. The growth of (La,Sr)TiO<sub>3</sub> films was performed by pulsed laser deposition (PLD) in vacuum at 750°C, at an energy of 2 J/cm<sup>2</sup> and repetition rate of 5~10Hz with a thickness of 0.6µm. A KrF (248nm) excimer laser was used as the ablation source. Ir seed layers were used as an oxygen barrier before (La,Sr)TiO<sub>3</sub> deposition on Cu tapes. Thin films of Ir were grown by PLD in 7.0×10<sup>-4</sup> Torr of 4% H<sub>2</sub>/Ar mixture gas at 300°C, energy density of 4 J/cm<sup>2</sup>, 40Hz, with thickness below 0.1µm. YBa<sub>2</sub>Cu<sub>3</sub>O<sub>7-δ</sub> layer was grown as a high temperature superconductor by PLD under conditions of 1.0×10<sup>-1</sup> Torr of oxygen at 780°C, energy density of 2 J/cm<sup>2</sup>, 10Hz rate, with a thickness of 0.2µm. After completing YBCO deposition, the PLD chamber was cooled down to 500°C at a rate of 28°C/min and the oxygen pressure was increased to 400 Torr. After 20 minutes, the chamber was cooled down to room temperature rapidly.



The x-ray diffraction of  $\theta$ - $2\theta$  scan,  $\omega$  and  $\phi$ -scan were used in order to observe the in-plane and out-of-plane alignments of each layers. The in situ reflection high-energy electron diffraction (RHEED) was used to monitor epitaxial film growth. The surface observation and the compositional analysis of thin films were investigated by scanning electron microscope (SEM) and energy dispersive x-ray spectroscopy (EDS).

A standard four probe technique was used to evaluate the electrical properties, including superconducting transition temperature ( $T_c$ ) and the critical current density ( $J_c$ ). The  $J_c$  measurements were carried out in liquid nitrogen, defined at a 1  $\mu\text{V}/\text{cm}$  criterion. The widths of the samples were in the range of 0.40 ~0.50cm and the distance between the voltage tips was in the range of 0.3~0.4cm.

### 6.3 Results and Discussion

One of the clue that the Cu substrate has a critical problem of oxidation is showing in the figure 6-1 and figure 6-2. After depositing  $(\text{La,Sr})\text{TiO}_3$  film on Cu tape, annealing was done at  $780^\circ\text{C}$  in oxygen  $1.0 \times 10^{-1}$  Torr for 7 minutes which is the  $\text{YBa}_2\text{Cu}_3\text{O}_7$  film growth condition in PLD system. According to these SEM and EDS figures, the surface of the as deposited film of  $(\text{La,Sr})\text{TiO}_3$  was covered with the Cu oxide. For this reason, iridium was selected as an oxygen diffusion barrier on Cu tape. Figure 6-3 shows the X-ray diffraction  $\theta$ - $2\theta$  scan of Ir film deposited on textured Cu substrate and  $(\text{La,Sr})\text{TiO}_3$  film grown on Ir layer. Figure 6-4 shows the in situ monitored reflection high-energy electron diffraction (RHEED) patterns of Ir layer deposited on Cu tape and  $(\text{La,Sr})\text{TiO}_3$  film grown on Ir layer. According to the x-ray  $\theta$ - $2\theta$  scan and RHEED pattern, the Ir film is epitaxially deposited on textured Cu tape. In addition to that, the  $(\text{La,Sr})\text{TiO}_3$  buffer layer also formed epitaxially on the Ir layer. From the X-ray diffraction  $\omega$ -scans shown in

figure 6-5, the full width half maximum (FWHM) value of (002) Ir showed  $6.20^\circ$  which is close to the substrate Cu (002) of  $5.41^\circ$ . (La,Sr)TiO<sub>3</sub> film grown on Ir showed FWHM value of  $12.3^\circ$ . The in-plane aligned texture of the (La,Sr)TiO<sub>3</sub> film which is grown on Ir layer is shown in the X-ray  $\phi$ -scan. The large peaks every 90 degrees in figure 6-6 represent the majority in-plane aligned (La,Sr)TiO<sub>3</sub>. The FWHM value of the  $\phi$ -scan is  $8.63^\circ$ . Figure 6-7 shows the pole figure graphs of (111) Cu, (111) Ir and (112) (La,Sr)TiO<sub>3</sub>. The pole figure is generated by scanning X-ray signals with rotating the sample  $360^\circ$  ( $\phi$ -scan) and tilting it from  $0^\circ$  to  $90^\circ$  ( $\psi$ -scan) at a specific  $\theta$  angle. The fourfold symmetric poles indicate that the film is in-plane and out-of-plane aligned. In addition to this, the volume fraction of the poles explains the extent of this alignment quantitatively. From these X-ray analysis, a cube-on-cube epitaxial relationship was obtained among the Cu substrate, Ir and (La,Sr)TiO<sub>3</sub> films.

In order to investigate the electrical connectivity of (La,Sr)TiO<sub>3</sub> film to Ir layer, temperature dependent resistivity measurement was performed. Figure 6-8 shows the resistivity curves of Ir film, (La,Sr)TiO<sub>3</sub> film grown on Ir layer and (La,Sr)TiO<sub>3</sub> film, respectively. All the films were grown on SrTiO<sub>3</sub> single crystal substrates. The (La,Sr)TiO<sub>3</sub> films of these samples were deposited at  $612^\circ\text{C}$ , in vacuum by PLD system. The resistivity curve of (La,Sr)TiO<sub>3</sub> film deposited on Ir layer shows quite different shape from the (La,Sr)TiO<sub>3</sub> film itself. And it follows the Ir curve shape even showing lower values. This indicates that the (La,Sr)TiO<sub>3</sub> film is electrically well connected to the underlying Ir layer. Figure 6-9 designates the resistivity curves of Ir films grown on single crystal SrTiO<sub>3</sub> substrate before and after annealing at  $780^\circ\text{C}$  in oxygen pressure of

$1.0 \times 10^{-1}$  Torr for 7 minutes. In this figure, Ir shows no resistivity change even after annealing at the severe oxidizing condition.

In order to assess the compatibility of (La,Sr)TiO<sub>3</sub> as a buffer layer for Cu based RABiTS application, the growth of YBa<sub>2</sub>Cu<sub>3</sub>O<sub>7- $\delta$</sub>  thin film on (La,Sr)TiO<sub>3</sub> / Ir / Cu tape structure was investigated. The X-ray diffraction  $\theta$ -2 $\theta$  scan in figure 6-10 shows clear YBa<sub>2</sub>Cu<sub>3</sub>O<sub>7- $\delta$</sub>  peaks. Because the YBa<sub>2</sub>Cu<sub>3</sub>O<sub>7- $\delta$</sub>  thin film was grown under conditions of  $1.0 \times 10^{-1}$  Torr of oxygen at 780°C, copper oxide peaks were observed in this figure. Figure 6-11 shows the defects on the surface of the YBa<sub>2</sub>Cu<sub>3</sub>O<sub>7</sub> film of the sample. Figure 6-12 is the energy dispersive X-ray spectroscopy graphs of the normal YBa<sub>2</sub>Cu<sub>3</sub>O<sub>7</sub> film surface and the defect region of the YBa<sub>2</sub>Cu<sub>3</sub>O<sub>7</sub> film. The normal surface of the film shows only Y, Ba, Cu, O contents. On the other hand, the defect region shows Cu and O peaks which indicate that the defects are copper oxides. These copper oxides were formed by the reaction of oxygen gas and the Cu elements which were diffused out from the Cu tape.

A standard four-probe technique was used to evaluate the electrical properties, including superconducting transition temperature ( $T_c$ ) and critical current density ( $J_c$ ). The  $J_c$  value was assigned at a 1  $\mu$ V/cm criterion. Figure 6-13 shows the temperature-dependent net resistivity of the YBa<sub>2</sub>Cu<sub>3</sub>O<sub>7- $\delta$</sub>  on (La,Sr)TiO<sub>3</sub> and Ir buffer stack on Cu tape. The sample has a  $T_c$  value of 90 K and the zero-field transport  $J_c$  was  $1.0 \times 10^6$  A/cm<sup>2</sup>. These results indicate that the metallic (La,Sr)TiO<sub>3</sub> layer played an excellent role of templating HTS film. And fully conductive buffer layer scheme could be obtained in the Cu based RABiTS applications. According to the X-ray  $\theta$ -2 $\theta$  scan, surface SEM pictures and the EDS analysis of the YBa<sub>2</sub>Cu<sub>3</sub>O<sub>7</sub> film, the thicknesses of (La,Sr)TiO<sub>3</sub> and

Ir buffers should be considered carefully to prevent forming copper oxide either on top of  $\text{YBa}_2\text{Cu}_3\text{O}_7$  or in the interface between the Cu tape and the buffer layers.

#### 6.4 Conclusions

The epitaxial film growth of  $(\text{La,Sr})\text{TiO}_3$  was examined on Cu tape as a possible conducting buffer layer for high temperature superconducting coated conductors. The noble metal such as Ir was deposited epitaxially on Cu tape by PLD for oxygen diffusion barrier.

The high temperature superconducting  $\text{YBa}_2\text{Cu}_3\text{O}_7$  film was deposited epitaxially on  $(\text{La,Sr})\text{TiO}_3$  and Ir buffer stack on Cu tape. The  $\text{YBa}_2\text{Cu}_3\text{O}_7$  film grown on  $(\text{La,Sr})\text{TiO}_3$  / Ir / Cu tape has superconducting transition temperature of 90 K and critical current density value of  $1.0 \times 10^6 \text{ A/cm}^2$ . This shows that  $(\text{La,Sr})\text{TiO}_3$  is a possible candidate for the conductive buffer layer in the Cu based RABiTS applications.

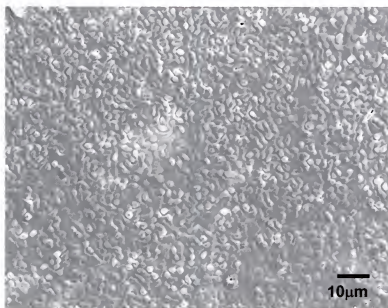


Figure 6-1. The surface SEM picture of the (La,Sr)TiO<sub>3</sub> film grown on Cu tape after annealing at 780°C in oxygen partial pressure of  $1.0 \times 10^{-1}$  Torr for 7 minutes.

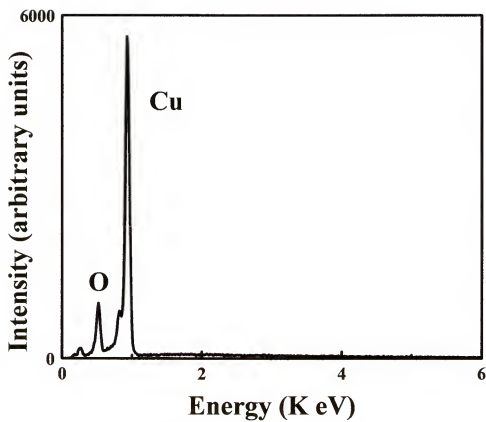


Figure 6-2. The energy dispersive X-ray spectroscopy (EDS) graph of (La,Sr)TiO<sub>3</sub> film grown on Cu tape after annealing at 780°C in oxygen  $1.0 \times 10^{-1}$  Torr for 7 minutes.

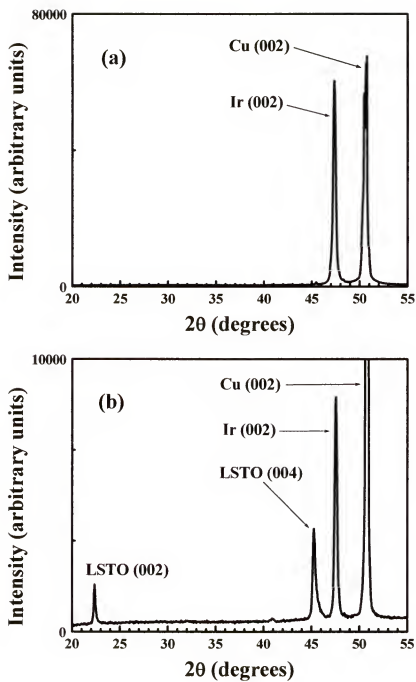


Figure 6-3. The X-ray diffraction  $\theta$ - $2\theta$  scan of (a) Ir layer deposited on textured Cu by PLD, and (b) (La,Sr)TiO<sub>3</sub> film deposited on Ir layer.

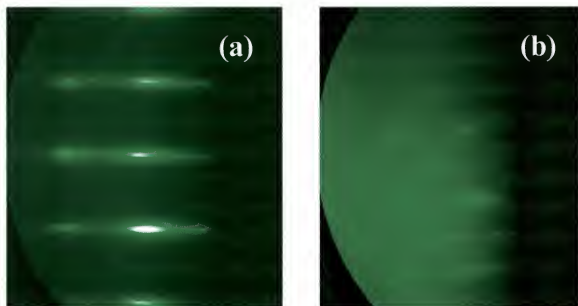


Figure 6-4. The in situ reflection high-energy electron diffraction (RHEED) pattern of Ir film deposited on textured Cu tape, and (b) (La,Sr)TiO<sub>3</sub> film deposited on Ir layer.



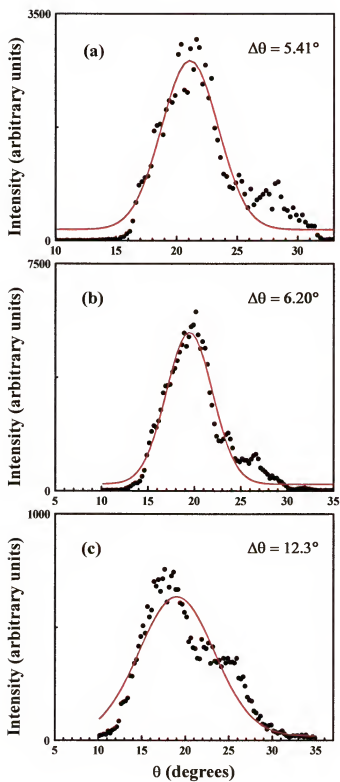


Figure 6-5. The X-ray diffraction  $\omega$ -scan of (a) Cu (002), (b) Ir (002), and (c) (La,Sr)TiO<sub>3</sub> (004) planes.

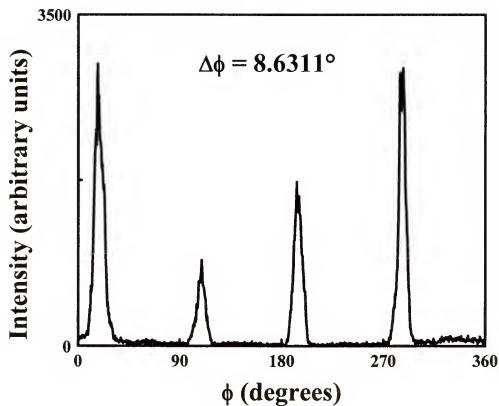
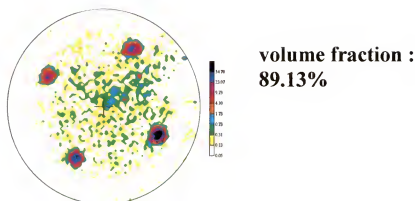
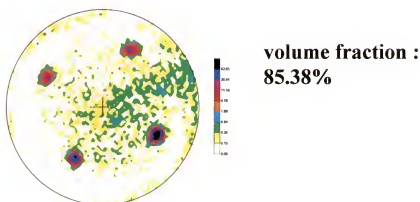


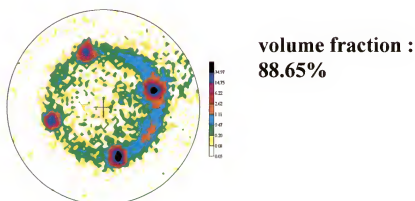
Figure 6-6. The X-ray diffraction  $\phi$ -scan of (La,Sr)TiO<sub>3</sub> (112) which was grown on Ir film on Cu tape.



(a)



(b)



(c)

Figure 6-7. The X-ray pole figures of (a) Cu (111), (b) Ir (111), and (c) (La,Sr)TiO<sub>3</sub> (112).

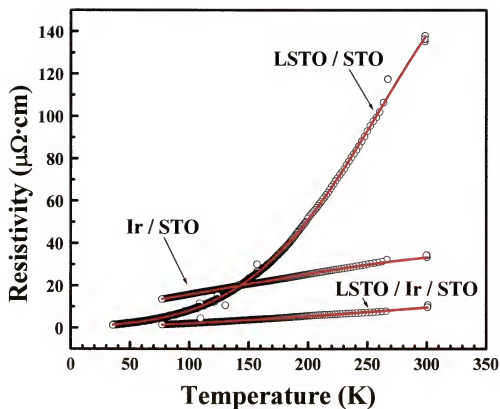


Figure 6-8. The resistivity curves of Ir on  $\text{SrTiO}_3$  single crystal,  $(\text{La,Sr})\text{TiO}_3$  film on  $\text{SrTiO}_3$  substrate and  $(\text{La,Sr})\text{TiO}_3$  film on Ir on  $\text{SrTiO}_3$  substrate.

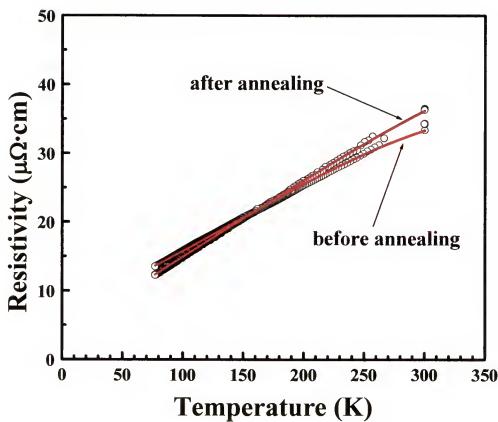


Figure 6-9. The resistivity curves of Ir on SrTiO<sub>3</sub> single crystal with and without annealing at 780°C in oxygen  $1.0\times 10^{-4}$  Torr for 7 minutes.

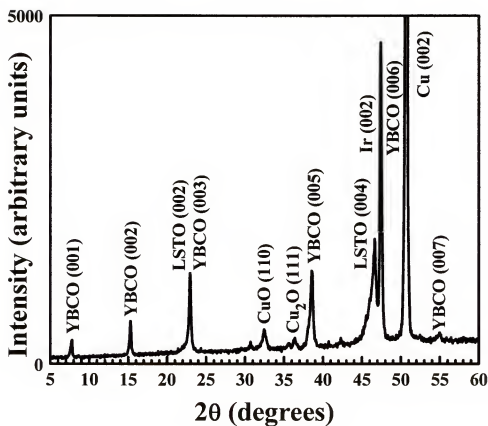


Figure 6-10. The X-ray diffraction 0-2θ scan of YBa<sub>2</sub>Cu<sub>3</sub>O<sub>7</sub> layer deposited on (La,Sr)TiO<sub>3</sub> / Ir multi buffer stack on textured Cu tape.

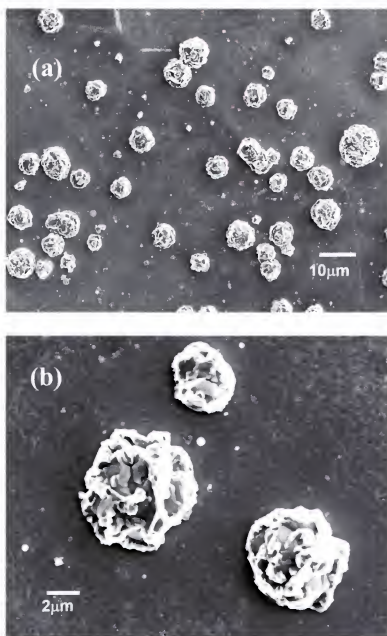


Figure 6-11. The surface SEM picture of the  $\text{YBa}_2\text{Cu}_3\text{O}_7$  film grown on  $(\text{La,Sr})\text{TiO}_3$  / Ir buffer stack on Cu tape with the magnification of (a)  $\times 1000$  and (b)  $\times 5000$ .

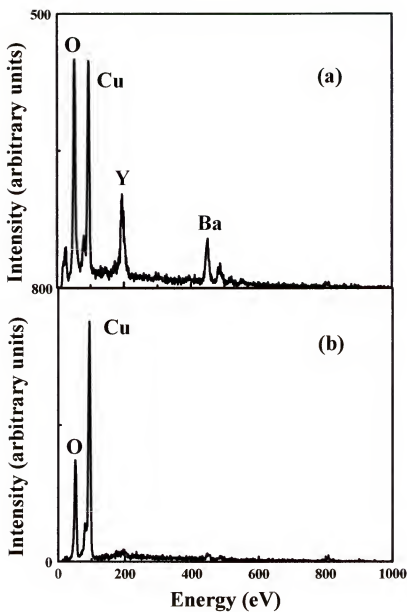


Figure 6-12. The energy dispersive X-ray spectroscopy (EDS) graph of (a) normal  $\text{YBa}_2\text{Cu}_3\text{O}_7$  film surface, (b) defect region of  $\text{YBa}_2\text{Cu}_3\text{O}_7$  film.



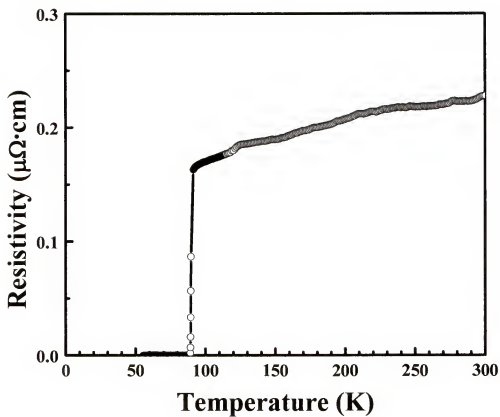


Figure 6-13. The resistivity versus temperature measurement for YBa<sub>2</sub>Cu<sub>3</sub>O<sub>7</sub> film deposited on (La,Sr)TiO<sub>3</sub> / Ir multi buffer stack on Cu tape.

## CHAPTER 7

### SUMMARY

Epitaxial growth of intermetallic  $\text{Cu}_2\text{Mg}$  was investigated for the Cu based RABiTS applications. Epitaxial growth of  $(\text{La},\text{Sr})\text{TiO}_3$  layer was investigated for the conductive buffer architecture of Cu based high temperature superconducting coated conductors.

In order to form the oxidation resistant buffers for RABiTS-based conductors, the epitaxial growth of  $(\text{Cu},\text{Mg})$  films on a (001) Cu surface was investigated. The approach used to achieve epitaxy of  $(\text{Cu},\text{Mg})$  films was to form Cu/Mg multilayer precursor films that would be subsequently annealed to form either Mg-doped fcc Cu or intermetallic  $\text{Cu}_2\text{Mg}$ . The precursor consists of an Mg/Cu multilayer stack with 5 each of 25 nm thick Mg and 25 nm thick Cu layers which were grown at room temperature by sputter deposition. Annealing was performed in a flowing  $\text{H}_2/\text{Ar}$  mixture. At annealing temperature of  $400^\circ\text{C}$ , formation of the intermetallic  $\text{Cu}_2\text{Mg}$  was observed. X-ray diffraction rocking curve for the (004)  $\text{Cu}_2\text{Mg}$  peak showed a full-width half-maximum (FWHM) of  $\Delta\theta = 2.0^\circ$ , which is slightly larger than that for the Cu film ( $\Delta\theta = 1.45^\circ$ ). An in-plane  $\phi$ -scan through the  $\text{Cu}_2\text{Mg}$  (222) indicates that the grains are epitaxial with respect to the Cu film, possessing a cube-on-cube orientation. The FWHM of the in-plane peak is  $2.1^\circ$ . In order to confirm the oxidation resistance of the structures possessing  $(\text{Cu},\text{Mg})$  alloy films,  $\text{CeO}_2$  films were deposited at elevated temperature on  $\text{Ni}/(\text{Cu},\text{Mg})/\text{Cu}/\text{MgO}$  and on  $\text{Ni}/\text{Cu}/\text{MgO}$ . In case of the  $\text{CeO}_2$  film on  $\text{Ni}/\text{Cu}/\text{MgO}$ , significant surface roughness due to the metal oxidation is observed. In contrast, no

surface roughness is observed in the SEM image for the  $\text{CeO}_2/\text{Ni}/(\text{Cu},\text{Mg})/\text{Cu}/\text{MgO}$  structure.

The perovskite  $(\text{La},\text{Sr})\text{TiO}_3$  was investigated as a possible conducting oxide buffer layer for high temperature superconducting coated conductors. In order to observe the oxygen sensitivity, thin  $(\text{La},\text{Sr})\text{TiO}_3$  films were epitaxially deposited by PLD on single crystal  $\text{SrTiO}_3$  substrates at various oxygen partial pressures and compared with  $\text{LaTiO}_3$  films at the same growth conditions. The room temperature resistivity of  $\text{LaTiO}_3$  increases rapidly as the oxygen pressure increases by more than two orders of magnitude. In contrast, the resistivity of  $(\text{La},\text{Sr})\text{TiO}_3$  films is relatively insensitive to oxygen pressure making it attractive as a conductive buffer for coated conductor applications. The high temperature superconducting layer such as  $\text{YBa}_2\text{Cu}_3\text{O}_7$  was grown epitaxially on  $(\text{La},\text{Sr})\text{TiO}_3$  buffer layer on  $\text{SrTiO}_3$  substrate with excellent in-plane and out-of-plane alignment. The superconducting transition temperature ( $T_c$ ) of  $\text{YBa}_2\text{Cu}_3\text{O}_7 / (\text{La},\text{Sr})\text{TiO}_3 / \text{SrTiO}_3$  structure was 91 K and the critical current density ( $J_c$ ) of this structure was  $2.18 \times 10^6 \text{ A/cm}^2$  at 0 magnetic field. The resistivity results of post annealed sample at  $\text{YBa}_2\text{Cu}_3\text{O}_7$  deposition condition indicates that the  $(\text{La},\text{Sr})\text{TiO}_3$  layer can be a candidate for the conductive buffer layer in the coated conductor applications.

The epitaxial film growth of  $(\text{La},\text{Sr})\text{TiO}_3$  was examined on Ni-W metal alloy tape. The transition metal nitride such as TiN was deposited epitaxially on Ni-W tape by PLD and played an excellent role as a seed layer for  $(\text{La},\text{Sr})\text{TiO}_3$  film growth on Ni-W tape. The high temperature superconducting  $\text{YBa}_2\text{Cu}_3\text{O}_7$  film was deposited epitaxially on  $(\text{La},\text{Sr})\text{TiO}_3$  buffer layer with the TiN seed layer on Ni-W tape. The  $\text{YBa}_2\text{Cu}_3\text{O}_7$  film

grown on (La,Sr)TiO<sub>3</sub> / TiN / Ni-W tape has superconducting transition temperature of 89 K and critical current value of  $0.42 \times 10^6$  A/cm<sup>2</sup>.

The epitaxial film growth of (La,Sr)TiO<sub>3</sub> was examined on Cu tape as a possible conducting buffer layer for high temperature superconducting coated conductors. The noble metal such as Ir was deposited epitaxially on Cu tape by PLD for oxygen diffusion barrier. The high temperature superconducting YBa<sub>2</sub>Cu<sub>3</sub>O<sub>7</sub> film was deposited epitaxially on (La,Sr)TiO<sub>3</sub> and Ir buffer stack on Cu tape. The YBa<sub>2</sub>Cu<sub>3</sub>O<sub>7</sub> film grown on (La,Sr)TiO<sub>3</sub> / Ir / Cu tape has superconducting transition temperature of 90 K and critical current density value of  $1.0 \times 10^6$  A/cm<sup>2</sup>.

## LIST OF REFERENCES

1. M.R. Beasley, and T.H. Geballe, *Phys. Today* **36**, 60 (1984)
2. D.C. Johnston, H. Prakash, W.H. Zachariasen, and R. Viswanathan, *Mat. Res. Bull.* **8**, 777 (1973)
3. T.D. Thanh, A. Koma, and S. Tanaka, *Appl. Phys.* **22**, 205 (1980)
4. J. Bardeen, L.N. Cooper, and J.R. Schrieffer, *Physical Review* **108**, 1175 (1957)
5. P. Townsend, and J. Sutteon, *Physical Review* **128**, 591 (1962)
6. Frank J. Blatt, *Modern Physics*, McGraw-Hill (1992)
7. F. London, and H. London, *Proc. Roy. Soc. (London)* **149**, 71 (1935)
8. G. Burns, *High-Temperature Superconductivity an Introduction*, Academic Press, Inc., San Diego (1992)
9. C.P. Poole, Jr., H.A. Farach, and R.J. Creswick, *Superconductivity*, Academic Press, San Diego (1995)
10. J.G. Bednorz and K.A. Müller, *Z. Phys. B – Condensed Matter* **64**, 189 (1986)
11. M.K. Wu, J.R. Ashburn, C.J. Torng, P.H. Hor, R.L. Meng, L.Gao, Z.J. Huang, Y.Q. Wang, and C.W. Chu, *Physical Review Letters* **58**, 908 (1987)
12. H. Maeda, Y. Tanaka, M. Fukutomi, and T. Asano, *Japanese Journal of Applied Physics* **27**, L209 (1988)
13. Z.Z. Sheng, W. Kiehl, J. Bennett, A. El Ali, D. Marsh, G.D. Mooney, F. Arammash, J. Smith, D. Viar, and A.M. Hermann, *Appl. Phys. Lett.* **52**, 1738 (1988)
14. S.N. Putilin, E.V. Antipov, and M. Marezio, *Physica C*, **212**, 266 (1993)
15. D.P. Norton, *Annu. Rev. Mater. Sci.* **28**, 299 (1998)

16. M.A. Beno, L. Soderholm, D.W. Capone, II, D.G. Hinks, J.D. Jorgensen, J.D. Grace, Ivan K. Schuller, C.U. Segre, and K. Zhang, *Appl. Phys. Lett.* **51**, 57 (1987)
17. P.K. Gallagher, H.M. O'Bryan, S.A. Sunshine, and D.W. Murphy, *Mat. Res. Bull.* **22**, 995 (1987)
18. R.J. Cava, B. Batlogg, C.H. Chen, E.A. Rietman, S.M. Zahurak, and D. Werder, *Nature* **329**, 423 (1987)
19. A. Santoro, S. Miraglia, and F. Beech, *Mat. Res. Bull.* **22**, 1007 (1987)
20. P.M. Mankiewich, J.H. Scofield, W.J. Skocpol, R.E. Howard, A.H. Dayem, and E. Good, *Appl. Phys. Lett.* **51**, 1753 (1987)
21. R. Feenstra, L.A. Boatner, J.D. Budai, D.K. Christen, M.D. Galloway, and D.B. Poker, *Appl. Phys. Lett.* **54**, 1063 (1989)
22. Y. Zhang, R. Feenstra, J.R. Thompson, A.A. Gapud, T. Aytug, P.M. Martin, and D.K. Christen, *Supercond. Sci. Technol.* **17**, 1154 (2004)
23. C.B. Eom, J.Z. Sun, K. Yamamoto, A.F. Marshall, K.E. Luther, T.H. Geballe, and S.S. Laderman, *Appl. Phys. Lett.* **55**, 595 (1989)
24. D.P. Norton, D.H. Lowndes, X.-Y. Zheng, S. Zhu, and R.J. Warmack, *Physical Review B* **44**, 9760 (1991)
25. J. Akimitsu, A. Yamazaki, H. Sawa, and H. Fujiki, *Japanese Journal of Applied Physics* **26**, L2080 (1987)
26. C. Michel, M. Hervieu, M.M. Borel, A. Grandin, F. Deslandes, J. Provost, and B. Raveau, *Z. Phys. B – Condensed Matter* **68**, 421 (1987)
27. S.A. Sunshine, T. Siegrist, L.F. Schneemeyer, D.W. Murphy, R.J. Cava, B. Batlogg, R.B. van Dover, R.M. Fleming, S.H. Glarum, S. Nakahara, R. Farrow, J.J. Krajewski, S.M. Zahurak, J.V. Waszczak, J.H. Marshall, P. Marsh, L.W. Rupp, Jr., and W.F. Peck, *Physical Review B* **38**, 893 (1988)
28. M. Kanai, T. Kawai, and S. Kawai, *Appl. Phys. Lett.* **54**, 1802 (1989)
29. M. Kanai, T. kawai, M. Kawai, and S. Kawai, *Japanese Journal of Applied Physics* **27**, L1293 (1988)
30. M.A. Subramanian, C.C. Torardi, J.C. Calabrese, J. Gopalakrishnan, K.J. Morrissey, T.R. Askew, R.B. Flippin, U. Chowdhry, and A.W. Sleight, *Science* **239**, 1015 (1988)

31. H. Tabata, T. Kawai, M. Kanai, O. Murata, and S. Kawai, *Japanese Journal of Applied Physics* **28**, L430 (1989)
32. T. Kawai, Y. Egami, H. Tabata, and S. Kawai, *Nature* **349**, 200 (1991)
33. G.B. Lubkin, *Physics Today* **49**, 48 (1996)
34. P. Chaudhari, J. Mannhart, D. Dimos, C.C. Tsuei, J. Chi, M.M. Oprysko, and M. Scheuermann, *Physical Review Letters* **60**, 1653 (1988)
35. A. Goyal, D.P. Norton, J.D. Budai, M. Paranthaman, E.D. Specht, D.M. Kroeger, D.K. Christen, Q. He, B. Saffian, F.A. List, D.F. Lee, P.M. Martin, C.E. Klabunde, E. Hartfield, and V.K. Sikka, *Appl. Phys. Lett.* **69**, 1795 (1996)
36. A. Goyal, D.P. Norton, D.K. Christen, E.D. Specht, M. Paranthaman, D.M. Kroeger, J.D. Budai, Q. He, F.A. List, R. Feenstra, H.R. Kerchner, D.F. Lee, E. Hatfield, P.M. Martin, J. Mathis, and C. Park, *Applied Superconductivity* **4**, 403 (1996)
37. Selected Powder Diffraction Data for Metals and Alloys, First edition, **Volume I**, JCPDS-International Centre for Diffraction Data, Pennsylvania (1978)
38. E.D. Specht, A. Goyal, D.F. Lee, F.A. List, D.M. Kroeger, M. Paranthaman, R.K. Williams, and D.K. Christen, *Supercond. Sci. Technol.* **11**, 945 (1998)
39. A. Goyal, R. Feenstra, M. Paranthaman, J.R. Thompson, B.Y. Kang, C. Cantoni, D.F. Lee, F.A. List, P.M. Martin, E. Lara-Curzio, C. Stevens, D.M. Kroeger, M. Kowalewski, E.D. Specht, T. Aytug, S. Sathyamurthy, R.K. Williams, and R.E. Ericson, *Physica C* **382**, 251 (2002)
40. A.O. Ijaduola, J.R. Thompson, A. Goyal, C.L.H. Thieme, and K. Marken, *Physica C* **403**, 163 (2004)
41. J.R. Thompson, A. Goyal, D.K. Christen, and D.M. Kroeger, *Physica C* **370**, 169 (2002)
42. A. Goyal, M. Parans Paranthaman, and U. Schoop, *MRS Bulletin* **29**, 552 (2004)
43. T.J. Jackson, B.A. Glowacki, and J.E. Evetts, *Physica C* **296**, 215 (1998)
44. J.M.S. Skakle, *Materials Science and Engineering* **R23**, 1 (1998)
45. G. Xiao, F.H. Streitz, A. Gavrin, Y.W. Du, and C.L. Chien, *Physical Review B* **35**, 8782 (1987)

46. Y. Maeno, T. Tomita, M. Kyogoku, S. Awaji, Y. Aoki, K. Hoshino, A. Minami, and T. Fujita, *Nature* **328**, 512 (1987)
47. P. Strobel, C. Paulsen, and J.L. Tholence, *Solid State Communications* **65**, 585 (1988)
48. J.M. Tarascon, P. Barboux, P.F. Miceli, L.H. Greene, and G.W. Hull, *Physical Review B* **37**, 7458 (1998)
49. E. T-Muromachi, Y. Uchida, and K.Kato, *Japanese Journal of Applied Physics* **26**, L2087 (1987)
50. S. Witanachi, S. Patel, H.S. Kwok, and D.T. Shaw, *Appl. Phys. Lett.* **54**, 578 (1989)
51. A.B. Berezin, C.W. Yuan, and A.L. de Lozanne, *Appl. Phys. Lett.* **57**, 90 (1990)
52. Y. Hakuraku, K. Maezono, and H. Ueda, *Supercond. Sci. Technol.* **9**, 775 (1996)
53. K. Char, M.S. Colclough, S.M Garrison, N. Newman, and G. Zaharchuk, *Appl. Phys. Lett.* **59**, 733 (1991)
54. B.K. Moon, and H. Ishiwara, *Jpn. J. Appl. Phys.* **33**, 1472 (1994)
55. H. Ishiwara, N. Tsuji, H. Mori, and H. Nohira, *Appl. Phys. Lett.* **61**, 1459 (1992)
56. M.G. Blamire, G.W. Morris, R.E. Somekh, and J.E. Evetts, *J. Phys. D: Appl. Phys.* **20**, 1330 (1987)
57. K. Hirata, K. Yamamoto, K. Iijima, J. Takada, T. Terashima, Y. Bando, and H. Mazaki, *Appl. Phys. Lett.* **56**, 683 (1990)
58. M. Migliuolo, A.K. Stamper, D.W. Greve, and T.E. Schlesinger, *Appl. Phys. Lett.* **54**, 859 (1989)
59. H. Myoren, Y. Nishiyama, N. Miyamoto, Y. Kai, Y. Yamanaka, Y. Osaka, and F. Nishiyama, *Japanese Journal of Applied Physics* **29**, L955 (1990)
60. Q.Z. Jia, S.Y. Lee, W.A. Anderson, and D.T. Shaw, *Appl. Phys. Lett.* **59**, 1120 (1991)
61. M.W. Denhoff, and J.P. McCaffrey, *J. Appl. Phys.* **70**, 3986 (1991)
62. T. Venkatesan, E.W. Chase, X.D. Wu, A. Inam, C.C. Chang, and F.K. Shokoohi, *Appl. Phys. Lett.* **53**, 243 (1988)



63. K. Harada, N. Fujimori, and S. Yazu, *Japanese Journal of Applied Physics* **27**, L1524 (1988)
64. L.S. Hung, J.A. Agostinelli, G.R. Paz-Pujalt, and J.M. Mir, *Appl. Phys. Lett.* **53**, 2450 (1988)
65. D.P. Norton, A. Goyal, J.D. Budai, D.K. Christen, D.M. Kroeger, E.D. Specht, Q. He, B. Saffian, M. Paranthaman, C.E. Klabunde, D.F. Lee, B.C. Sales, and F.A. List, *Science* **274**, 755 (1996)
66. M. Paranthaman, A. Goyal, F.A. List, E.D. Specht, D.F. Lee, P.M. Martin, Q. He, D.K. Christen, D.P. Norton, J.D. Budai, and D.M. Kroeger, *Physica C* **275**, 266 (1997)
67. Q. He, D.K. Christen, J.D. Budai, E.D. Specht, D.F. Lee, A. Goyal, D.P. Norton, M. Paranthaman, F.A. List, and D.M. Kroeger, *Physica C* **275**, 155 (1997)
68. J.E. Mathis, A. Goyal, D.F. Lee, F.A. List, M. Paranthaman, D.K. Christen, E.D. Specht, D.M. Kroeger, and P.M. Martin, *Jpn. J. Appl. Phys.* **37**, L1379 (1998)
69. I. Kim, P.N. Barnes, A. Goyal, S.A. Barnett, R. Biggers, G. Kozlowski, C. Varanasi, I. Maartens, R. Nekkanti, T. Peterson, T. Haugan, and S. Sambasivan, *Physica C* **377**, 227 (2002)
70. S-Q. Wang, I. Raaijmakers, B.J. Burrow, S. Suthar, S. Redkar, and K-B. Kim, *J. Appl. Phys.* **68**, 5176 (1990)
71. C. Cantoni, D.K. Christen, M. Varela, J.R. Thompson, S.J. Pennycook, E.D. Specht, and A. Goyal, *J. Mater. Res.* **18**, 2387 (2003)
72. L.J. Masur, D. Buczek, E. Harley, T. Kodenkandath, X. Li, J. Lynch, N. Nguyen, M. Rupich, U. Schoop, J. Scudiere, E. Siegal, C. Thieme, D. Verebelyi, W. Zhang, and J. Kellers, *Physica C* **392-396**, 989 (2003)
73. H. Maeda, Y. Tanaka, M. Fukutomi, T. Asano, K. Togano, H. Kumakura, M. Uehara, S. Ikeda, K. Ogawa, S. Horiuchi, and Y. Matsui, *Physica C* **153-155**, 602 (1988)
74. K. Heine, J. Tenbrink, and M. Thoner, *Appl. Phys. Lett.* **55**, 2441 (1989)
75. M. Parans Paranthaman, and T. Izumi, *MRS Bulletin* **29**, 533 (2004)
76. M.W. Rupich, U. Schoop, D.T. Verebelyi, C. Thieme, W. Zhang, X. Li, T. Kodenkandath, N. Nguyen, E. Siegal, D. Buczek, J. Lynch, M. Jowett, E. Thompson, J-S. Wang, J. Scudiere, A.P. Malozemoff, Q. Li, S. Annavarapu, S.

- Cui, L. Fritzemeier, B. Aldrich, C. Craven, F. Niu, R. Schwall, A. Goyal, and M. Paranthaman, *IEEE Trans. Appl. Supercond.* **13**, 2458 (2003)
77. R.E. Hummel, *Electronic Properties of Materials*, Springer-Verlag, New York (2001)
  78. A. Goyal, M. Parans Paranthaman, and U. Schoop, *MRS Bulletin* **29** 552 (2004)
  79. A.O. Ijaduola, J.R. Thompson, A. Goyal, C.L.H. Thieme, and K. Marken, *Physica C* **403**, 163 (2004)
  80. C. Cantoni, T. Aytug, D.T. Verebelyi, M. Paranthaman, E.D. Specht, D.P. Norton, and D.K. Christen, *IEEE Transactions on Applied Superconductivity* **11**, 3309 (2001)
  81. E.G. Brentari and R.V. Smith, *Adv. Cryog. Eng.* **10**, 325 (1965)
  82. S. Piñol, J. Díaz, M. Segarra, and F. Espiell, *Supercond. Sci. Technol.* **14**, 11 (2001)
  83. T. Aytug, B.W. Kang, C. Cantoni, E.D. Specht, M. Paranthaman, A. Goyal, D.K. Christen, D.T. Verebelyi, J.Z. Wu, R.E. Ericson, C.L. Thomas, C-Y. Yang, and S.E. Babcock, *Journal of Materials Research* **16**, 2661 (2001)
  84. X.D. Wu, S.R. Foltyn, R.C. Dye, Y. Coulter, and R.E. Muenchausen, *Appl. Phys. Lett.* **62**, 2434 (1993)
  85. K. Sreedhar, J.M. Honig, M. Darwin, M. McElfresh, P.M. Shand, J. Xu, B.C. Crooker, and J. Spalek, *Physical Review B* **46**, 6382 (1992)
  86. T. Aytug, M. Paranthaman, J.R. Thompson, A. Goyal, N. Rutter, H.Y. Zhai, A.A. Gapud, A.O. Ijaduola, and D.K. Christen, *Applied Physics Letters* **83**, 3963 (2003)
  87. H.M. Naguib, R.J. Kriegler, J.A. Davies, and J.B. Mitchell, *J. Vac. Sci. Technol.* **13**, 396 (1976)
  88. W.A. Lanford, P.J. Ding, W. Wang, S. Hymes, and S.P. Muraka, *Thin Solid Films* **262**, 234 (1995)
  89. Z-C. Wu, Y-L. Liu, and M-C. Chen, *Thin Solid Films* **346**, 186 (1999)
  90. Z-C. Wu, Y-L. Liu, and M-C. Chen, *Thin Solid Films* **358**, 180 (2000)
  91. X.Q. Zhao, Y.F. Han, and B.X. Liu, *J. Appl. Phys.* **90**, 1638 (2001)

92. B. Arcot, S.P. Murarka, L.A. Clevenger, Q.Z. Hong, W. Ziegler, and J.M.E. Harper, *J. Appl. Phys.* **76**, 5161 (1994)
93. M. Hansen and K. Anderko, *Constitution of Binary Alloys*, McGraw-Hill Book, New York (1958)
94. W.H. Lee, H.L. Cho, B.S. Cho, J.Y. Kim, W.J. Nam, Y-S. Kim, W.G. Jung, H. Kwon, J.H. Lee, and J.G. Lee, *Applied Physics Letters* **77**, 2191 (2000)
95. H. Jehn, *Journal of the Less-Common Metals* **100**, 321 (1984)
96. R.T. Wimber and H.G. Kraus, *Metallurgical Transactions* **5**, 1565 (1974)
97. H. Jehn, R. Völker, and M.I. Ismail, *Platinum Met. Rev.* **22**, 92 (1978)
98. M.A.E. Khakani and M. Chaker, *Thin Solid Films* **335**, 6 (1998)
99. T. Aytug, M. Paranthaman, H.T. Zhai, A.A. Gapud, K.J. Leonard, P.M. Martin, A. Goyal, J.R. Thompson, and D.K. Christen, *Applied Physics Letters* **85**, 2887 (2004)
100. W.G. Moffatt, *The Handbook of Binary Phase Diagrams*, Genium Publishing Corp., New York (1984)
101. M. Ohring, *Materials Science of Thin Films*, Academic Press, San Diego (2002)
102. H.S. Kim, K.C. Chung, B.S. Lee, S.M. Lim, and D. Youm, *Supercond. Sci. Technol.* **17**, 291 (2004)
103. G. Yuan, J. Yang, and K. Shi, *IEEE Trans. on Appl. Supercond.* **11**, 3382 (2001)
104. M.P. Paranthaman, T. Aytug, S. Kang, R. Feenstra, J.D. Budai, D.K. Christen, P.N. Arendt, L. Stan, J.R. Groves, R.F. DePaula, S.R. Foltyn, and T.G. Holesinger, *IEEE Trans. on Appl. Supercond.* **13**, 2481 (2003)
105. S.A. Campbell, *The Science and Engineering of Microelectronic Fabrication*, Oxford University Press, New York (1996)
106. R. Metzger, M.Bauer, K. Numssen, R. Semerad, P. Berberich, and H. Kinder, *IEEE Trans. on Appl. Supercond.* **11**, 2826 (2001)
107. L.D. Chang, M.Z. Tseng, and E.L. Hu, *Appl. Phys. Lett.* **60**, 1753 (1992)
108. A. Ichinose, C-Y. Yang, D.C. Larbalestier, S.E. Babcock, A. Kikuchi, K. Tachikawa, and S. Akita, *Physica C* **324**, 113 (1999)

109. A.P. Malozemoff, S. Annavarapu, L. Fritzemeier, Q. Li, V. Prunier, M. Rupich, C. Thieme, W. Zhang, A. Goyal, M. Paranthaman, and D.F. Lee, *Supercond. Sci. Technol.* **13**, 473 (2000)
110. D.B. Chrisey and G.K. Hubler, *Pulsed Laser Deposition of Thin Films*, John Wiley & Sons, Inc., New York (1994)
111. H. Iwai, T. Muroga, T. Watanabe, S. Miyata, Y. Yamada, Y. Shiohara, T. Kato, and T. Hirayama, *Supercond. Sci. Technol.* **17**, 496 (2004)
112. C. Park, D.P. Norton, D.K. Christen, D.T. Verebelyi, R. Feenstra, J.D. Budai, A. Goyal, D.F. Lee, E.D. Specht, D.M. Kroeger, and M. Paranthaman, *IEEE Trans. on Appl. Supercond.* **9**, 2276 (1999)
113. C. Cantoni, D.K. Christen, E.D. Specht, M. Varela, J.R. Thompson, A. Goyal, C. Thieme, Y. Xu, and S.J. Pennycook, *Supercond. Sci. Technol.* **17**, 341 (2004)
114. A. Usoskin and H.C. Freyhardt, *MRS Bulletin* **29**, 583 (2004)
115. R.W. Schwartz, *Chem. Mater.* **9**, 2325 (1997)
116. M. Paranthaman, S.S. Shoup, D.B. Beach, R.K. Williams, and E.D. Specht, *MRS Bulletin* **32**, 1697 (1997)
117. S. Sathyamurthy, M. Paranthaman, H-Y. Zhai, H.M. Christen, P.M. Martin, and A. Goyal, *J. Mater. Res.* **17**, 2181 (2002)
118. M.S. Bhuiyan, M. Paranthaman, S. Sathyamurthy, T. Aytug, S. Kang, D.F. Lee, A. Goyal, E.A. Payzant, and K. Salama, *Supercond. Sci. Technol.* **16**, 1305 (2003)
119. P.N. Arendt and S.R. Foltyn, *MRS Bulletin* **29**, 543 (2004)
120. J. Zaanen, G.A. Sawatzky, and J.W. Allen, *Physical Review Letters* **55**, 418 (1985)
121. J.B. Torrance, P. Lacorre, C. Asavaroengchai, and R.M. Metzger, *Physica C* **182**, 351 (1991)
122. R.D. Sánchez, M.T. Causa, A. Caneiro, A. Butera, M. Vallet-Regí, M.J. Sayagués, and J. González-Calbet, *Physical Review B* **54**, 16574 (1996)
123. Q. He, D.K. Christen, R. Feenstra, D.P. Norton, M. Paranthaman, E.D. Specht, D.F. Lee, A. Goyal, and D.M. Kroeger, *Physica C* **314**, 105 (1999)
124. A. Callaghan, C.W. Moeller, and R. Ward, *Inorganic Chemistry* **5**, 1572 (1966)

125. L. Klein, J.S. Dodge, C.H.Ahn, J.W. Reiner, L. Mieville, T.H. Geballe, M.R. Beasley, and A. Kapitulnik, *J. Phys.:Condens. Matter* **8**, 10111 (1996)
126. P. Tiwari, X.D. Wu, S.R. Foltyn, M.Q.Le, I.H. Campbell, R.C. Dye, and R.E. Muenchausen, *Appl. Phys. Lett.* **64**, 634 (1994)
127. T. Aytug, J.Z. Wu, C. Cantoni, D.T. Verebelyi, E.D. Specht, M. Paranthaman, D.P. Norton, D.K. Christen, R.E. Ericson, and C.L. Thomas, *Applied Physics Letters* **76**, 760 (2000)
128. C. Cantoni, T. Aytug, D.T. Verbelyi, M. Paranthaman, E.D. Specht, D.P. Norton, and D.K. Christen, *IEEE Trans. on Appl. Supercond.* **11**, 3309 (2001)
129. Q.X. Jia, S.R. Foltyn, P.N. Arendt, T. Holesinger, J.R. Groves, and M. Hawley, *IEEE Trans. on Appl. Supercond.* **13**, 2655 (2003)
130. J.M.D. Coey, M. Viret, and S. von Molnár, *Advances in Physics* **48**, 167 (1999)
131. C. Zener, *Physical Review* **82**, 403 (1951)
132. D.P. Norton, *Materials Science and Engineering R* **43**, 139 (2004)
133. T. Aytug, M. Paranthaman, B.W. Kang, S. Sathyamurthy, A. Goyal, and D.K. Christen, *Applied Physics Letters* **79**, 2205 (2001)
134. Y. Okada, T. Arima, Y. Tokura, C. Murayama, and N. Môri, *Physical Review B* **48**, 9677 (1993)
135. A. Schmehl, F. Lichtenberg, H. Bielefeldt, J. Mannhart, and D.G. Schlom, *Applied Physics Letters* **82**, 3077 (2003)
136. K. Yoshii, A. Nakamura, and H. Abe, *J. of Alloys and Compounds* **290**, 236 (1999)
137. F. Lichtenberg, D. Widmer, J.G. Bednorz, T. Williams, and A. Reller, *Z. Phys. B-Condensed Matter* **82**, 211 (1991)
138. J.G. Bednorz, *Physica C* **282-287**, 37 (1997)
139. K.H. Kim, D.P. Norton, J.D. Budai, M.F. Chisholm, B.C. Sales, D.K. Christen, and C. Cantoni, *phy. stat. sol. (a)* **200**, 346 (2003)
140. C.C. Hays, J.-S. Zhou, J.T. Markert, and J.B. Goodenough, *Physical Review B* **60**, 10367 (1999)

141. K. Kim, Y.W. Kwon, D.P. Norton, D.K. Christen, J.D. Budai, B.C. Sales, M.F. Chisholm, C. Cantoni, and K. Marken, *Solid-State Electronics* **47**, 2177 (2003)
142. K. Kim, D.P. Norton, C. Cantoni, T. Aytug, A.A. Gapud, M. Paranthaman, A. Goyal, and D.K. Christen, *IEEE Trans. on Appl. Supercond.*, to be published (2005)
143. G. Prokhorov, G.G. Kaminsky, I.I. Kravchenko, and Y.P. Lee, *Physica B* **324**, 205 (2002)
144. G. Yalovega and A.V. Soldatov, *phys. stat. sol. (b)* **218**, 455 (2000)
145. H.C. Yu and K.Z. Fung, *J. Mater. Res.* **19**, 943 (2004)
146. K.M. Satyalakshmi, R.M. Mallya, K.V. Ramanathan, X.D. Wu, B. Brainard, D.C. Gautier, N.Y. Vasanthachary, and M.S. Hegde, *Appl. Phys. Lett.* **62**, 1233 (1993)
147. X.Q. Xu, J.L. Peng, Z.Y. Li, H.L. Ju, and R.L. Greene, *Physical Review B* **48**, 1112 (1993)
148. C.N.R. Rao and B. Raveau, *Transition Metal Oxides*, John Wiley & Sons, Inc., New York (1998)
149. A.J. Millis, P.B. Littlewood, and B.I. Shraiman, *Physical Review Letters* **74**, 5144 (1995)
150. G. Demazeau, C. Parent, M. Pouchard, and P. Hagenmüller, *Mat. Res. Bull.* **7**, 913 (1972)
151. D.P. Norton, C. Park, C. Prouteau, D.K. Christen, M.F. Chisholm, J.D. Budai, S.J. Pennycook, A. Goyal, E.Y. Sun, D.F. Lee, D.M. Kroege, E. Specht, M. Paranthaman, and N.D. Browning, *Materials Science and Engineering* **B56**, 86 (1998)
152. S. Mrowec, and A. Stoklosa, *Oxidation of Metal* **3**, 291 (1971)
153. M. Hansen, and K. Anderko, *Constitution of Binary Alloys*, McGraw-Hill Book Company, New York, 594 (1958)
154. F.A. Shunk, *Constitution of Binary Alloys, Second Supplement*, McGraw-Hill Book Company, New York, 290 (1969)
155. K. Schroder, *Handbook of Electrical Resistivities of Binary Metallic Alloys*, CRC Press Inc., Boca Raton, FL, 219 (1983)

156. D. Goo, S. Oh, J. Kim, K. Jung, and D. Youm, *Physica C* **305**, 221 (1998)
157. T.J. Jackson, B.A. Glowacki, and J.E. Evetts, *Physica C* **296**, 215 (1998)
158. R.P. Wang, Y.L. Zhou, S.H. Pan, M. He, H.B. Lu, Z.H. Chen, G.Z. Yang, C.F. Liu, X. Wu, F.Y. Wang, Y. Feng, P.X. Zhang, X.Z. Wu, and L. Zhou, *Physica C* **337**, 87 (2000)
159. X.D. Wu, S.R. Foltyn, P.N. Arendt, W.R. Blumenthal, I.H. Campbell, J.D. Cotton, J.Y. Coulter, W.L. Hults, M.P. Maley, H.F. Safar, and J.L. Smith, *Appl. Phys. Lett.* **67**, 2397 (1995)
160. G. Sipos, B. Utz, W. Schmidt, H.W. Neumueller, and P. Mueller, *Physica C* **341**, 1457 (2000)
161. M. Jin, S.C. Han, T.H. Sung, and K. No, *Physica C* **334**, 243 (2000)
162. S.B. Kim, T. Maeda, Y. Yamada, T. Suga, Y. Yamada, T. Watanabe, K. Matsumoto, and I. Hirabayashi, *Physica C* **357-360**, 979 (2001)
163. K. Matsumoto, S.B. Kim, K. Yamagiwa, Y. Koike, I. Hirabayashi, T. Watanabe, N. Uno, and M. Ikeda, *Physica C* **335**, 39 (2000)
164. G. Celentano, C. Annino, V. Boffa, L. Ciontea, F. Fabbri, U. Gambardella, V. Galluzzi, G. Grimaldi, A. Mancini, L. Muzzi, and T. Petrison, *Physica C* **341-348**, 2501 (2000)
165. S. Gariglio, J.W. Seo, J. Fompeyrine, J.-P. Locquet, and J.-M. Triscone, *Physical Review B* **63**, 161103(R) (2001)
166. D.P. Norton, K. Kim, D.K. Christen, J.D. Budai, B.C. Sales, M.F. Chisholm, D.M. Kroeger, A. Goyal, and C. Cantoni, *Physica C* **372-376**, 818 (2002)
167. C. Cantoni, A. Goyal, U. Schoop, X. Li, M.W. Rupich, C. Thieme, A.A. Gapud, T. Aytug, M. Paranthaman, K. Kim, J.D. Budai, and D.K. Christen, *IEEE Trans. on Appl. Supercond.*, to be published (2005)
168. B.T. Liu, K. Maki, Y. So, V. Nagarajan, R. Ramesh, J. Lettieri, J.H. Haeni, D.G. Schlom, W. Tian, X.Q. Pan, F.J. Walker, and R.A. Mckee, *Appl. Phys. Lett.* **80**, 4801 (2002)
169. T. Hato, A. Yoshida, C. Yoshida, H. Suzuki, and N. Yokoyama, *Appl. Phys. Lett.* **70**, 2900 (1997)
170. G.Q. Li, P.T. Lai, S.H. Zeng, M.Q. Huang, and Y.C. Cheng, *Sensors and Actuators A* **63**, 223 (1997)

## BIOGRAPHICAL SKETCH

Kyunghoon Kim was born in Seoul, Republic of Korea, in November, 1964. He grew up and was educated in his hometown.

Kyunghoon received a B.S. degree in ceramics engineering from Yonsei University in Seoul, Korea, in 1988. After graduation he entered the R&D center of Samsung Semiconductor Inc. in Kiheung, Korea. He participated in the project of developing capacitor process for DRAM devices. From 1988 to 1992, he developed silicon oxide and silicon nitride films for capacitor dielectrics. From 1992 to 1994, he developed hemispherical grain silicon and various storage node structures for capacitance enhancement. From 1994 to 1999, he developed a high dielectric film process for a 1 giga bit DRAM device. The high dielectric film process includes the  $\text{Ta}_2\text{O}_5$  and  $\text{Al}_2\text{O}_3$  as high dielectric films and TiN film as an electrode material. He continued his study after work time at night and obtained his master's degree in 1996. The research topic for his master's degree was a study on the fabrication and characteristics of the tantalum oxide capacitor according to the nitridation pre-treatment. In 2000, he was admitted to the Department of Materials Science and Engineering at the University of Florida to pursue his Ph.D degree with a specialty in electronic materials. His research area at Dr. Norton's group was synthesis and characterization of conductive oxides on metal substrate. Furthermore, he extended his research interests into the application of high temperature superconducting coated conductor by collaboration in the Oak Ridge National Laboratory since 2002.

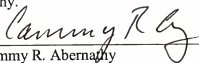


I certify that I have read this study and that in my opinion it conforms to acceptable standards of scholarly presentation and is fully adequate, in scope and quality, as a dissertation for the degree of Doctor of Philosophy.



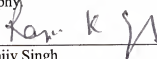
David P. Norton, Chair  
Professor of Materials Science and  
Engineering

I certify that I have read this study and that in my opinion it conforms to acceptable standards of scholarly presentation and is fully adequate, in scope and quality, as a dissertation for the degree of Doctor of Philosophy.



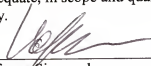
Cammy R. Abernathy  
Professor of Materials Science and  
Engineering

I certify that I have read this study and that in my opinion it conforms to acceptable standards of scholarly presentation and is fully adequate, in scope and quality, as a dissertation for the degree of Doctor of Philosophy.



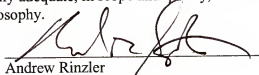
Rajiv Singh  
Professor of Materials Science and  
Engineering

I certify that I have read this study and that in my opinion it conforms to acceptable standards of scholarly presentation and is fully adequate, in scope and quality, as a dissertation for the degree of Doctor of Philosophy.



Wolfgang Sigmund  
Associate Professor of Materials Science  
and Engineering

I certify that I have read this study and that in my opinion it conforms to acceptable standards of scholarly presentation and is fully adequate, in scope and quality, as a dissertation for the degree of Doctor of Philosophy.



Andrew Rinzler  
Associate Professor of Physics

This dissertation was submitted to the Graduate Faculty of the College of Engineering and to the Graduate School and was accepted as partial fulfillment of the requirements for the degree of Doctor of Philosophy.

August 2005



---

Pramod P. Khargonekar  
Dean, College of Engineering

---

Kenneth Gerhardt  
Interim Dean, Graduate School